High-resolution ambient-noise and earthquake surface-wave tomography of the Alps Apennines and Dinarides

Emanuel David Käestle

Doctoral thesis

Université Pierre et Marie Curie
ED 398 - Géosciences, Ressources Naturelles et Environnement
Institut des Sciences de la Terre de Paris

Surface-wave imaging of the crust and uppermost mantle under the Alps and surrounding regions

Emanuel David Kästle

Public defense on September 19, 2017

Supervised by Lapo Boschi, Claudio Rosenberg and Nicolas Bellahsen

Jury members
Romain Bousquet – Professor (Universität Kiel) – Reviewer
Eduard Kissling – Professor (ETH Zürich) – Reviewer
Sylvie Leroy – Directrice de Recherche (UPMC Paris)
Jean-Paul Montagner – Professor (IPGP Paris)

Summary

The plate collision in the Alps and adjacent orogens has created a complex picture of highly arcuate mountain belts and complicated interactions of subduction slabs. The subduction polarity is reversed from European to Adriatic subduction in the transition of the Alps to the Apennines and to the Dinarides. The subduction of Adria both to the west and east and the almost vertical dip of the slabs implies an important flexure of this plate. Even more so if one considers the proposed subduction of Adria also to the north under the eastern Alps, which is still a matter of discussion. Gaps in the Adriatic slab under the northern Dinarides, below 150 km depth and in the southern Apennines above 200 km may be signs of the stresses and the consequent tearing that the Adriatic plate is exposed to.
Also the European plate has supposedly undergone one or several break-offs all along the Alpine arc. Especially in the eastern and western Alps it is still an open question whether the European slab is detached below the lithosphere. New tomographic models are thus needed.

The herein presented tomographic model is based on surface-wave phase velocities and gives a picture of the shear-velocity structure from the surface to 200 km depth. It is the first high-resolution shear-velocity model of the entire Alpine crust and upper mantle. It is also unique in its good resolution in the lithospheric mantle, where previous body-wave models are subject to high uncertainties. In order to be able to image both crust and upper mantle, a combination of ambient-noise and earthquake-based phase-velocity measurements is used in the present thesis.

The validity of this approach is tested by a detailed comparison of the phase-velocity measurements and the structures that are imaged from each method individually. A small bias between the methods results in slightly elevated velocities from earthquake measurements. By comparison with earlier works it appears that this bias is due to methodological differences. Several effects that may influence the ambient-noise records are tested with synthetic experiments, but no unique cause is found. The most likely explanation for the bias between the two methods is a combination of

different structural sensitivities and the influence of higher modes. Nevertheless, the discrepancy is sufficiently small with respect to the structural variations that the bias can be neglected.

A final shear-velocity model of the Alpine region is obtained which has a lateral resolution in the shallow crust of approximately 25 km. From synthetic tests, the average depth resolution is estimated to be 2 km close to the surface and 5 km for the Moho depth. In the upper mantle the resolution decreases significantly, but main slab structures are well imaged in the central Alps and the Apennines down to the bottom of the model at 200 km depth.
Highlights of the crustal part of the model are size and depth of sedimentary basins, the Ivrea body and the Moho structure. Being the first shear-velocity model of this detail and extend it is proposed to serve as reference for the Alps.

Limits of subduction zones and regions of low-velocity asthenospheric upwellings in the Ligurian and Pannonian basin are shown. Known features such as the Apenninic and Dinaric slab gaps are imaged, but also additional information is gained: A small low-velocity zone cuts through the northern Dinaric lithosphere and is interpreted as expression of a large-scale transform fault. In the western Alps, the European slab is limited at about 100 km depth and separated from the deeper lying slab. This is evidence of a slab detachment below the lithosphere. In contrast, the central Alpine slab is broad and shows the strongest v_S anomalies. This strong anomaly is sharply limited towards the east and only a moderate velocity increase appears east of the Giudicarie fault. This pronounced contrast in velocity anomaly between central and eastern Alps is most likely caused by a break-off of the European slab in the eastern Alps. Comparison with body-wave models indicate that at depth below 200 km, the European slab is still present. Above this depth, remnants of the European slab, an Adriatic slab or a combination of both may be the reason for the moderate v_S anomaly.

Résumé

La collision alpine a créé des structures complexes comme des chaînes de montagnes très arqués et des interactions compliquées entre les slabs subduits. La polarité de subduction est inversée à la transition entre les Alpes et les Apennins et les Alpes et les Dinarides. Le fait que la plaque Adria subducte en même temps vers l'ouest et vers l'est avec un fort pendage, presque verticalement, suggèrent une flexion importante de cette plaque. Notamment, si on considère de plus la proposition qu'Adria subducte aussi vers le nord sous les Alpes de l'est, ce qui est toujours sujet de discussion. Des déchirures dans le slab adriatique sous les Dinarides du nord à plus de 150 km de profondeur et sous les Apennins à moins de 200 km, pourraient être des signes d'une forte tension et, en conséquence, un détachement de la plaque adriatique. La plaque européenne pourrait aussi avoir subi plusieurs déchirures le long des Alpes. Cette hypothèse sujette à débat nécessite de nouveaux modèles tomographiques.

Le modèle tomographique présenté dans cette thèse se base sur les vitesses de phase des ondes de surface pour donner un modèle 3-D à haute résolution des vitesses de cisaillement de la surface jusqu'à 200 km de profondeur. Ce modèle est unique de par sa haute résolution dans le manteau lithosphérique où des modèles antérieurs montrent de fortes incertitudes. Afin d'imager la croûte et le manteau supérieur en même temps, une combinaison des données de vitesses de phase des ondes de surface mesurés à partir des bruits ambiants ainsi que des séismes est utilisée dans cette thèse.

Pour tester la validité de cette procédure, une comparaison détaillée des mesures de vitesses de phases et des structures imagées avec les deux méthodes est présentée. De l'analyse résulte un faible biais qui montre des vitesses plus élevées avec les données se basant sur des séismes par rapport aux données se basant sur le bruit ambiant. En comparant avec des travaux antérieurs, il est apparu que ce biais est dû à une différence méthodologique. Plusieurs paramètres qui pourraient influencer les mesures du bruit ambiant sont testés numériquement. Une cause unique n'a pu être identifiée. L'explication la plus probable pour le biais est une combinaison entre différentes sensibilités des méthodes aux structures et l'influence des modes supérieurs. Néanmoins,

l'écart est suffisamment faible par rapport aux variations structurales pour être négligé.

Un modèle final de vitesse de cisaillement de la région alpine est obtenu avec une résolution latérale d'environ 25 km dans la croûte peu profonde. Les tests synthétiques donnent une résolution approximative de profondeur estimée à 2 km près de la surface et de 5 km à la profondeur du Moho. Dans le manteau supérieur, la résolution baisse rapidement mais les structures principales des panneaux plongeants restent bien imagées jusqu'à une profondeur de 200 km le long des Alpes et des Apennins.
La partie crustale du modèle donne des informations à haute résolution sur la taille et la profondeur des bassins sédimentaires et du corps d'Ivrée ainsi que sur la profondeur et la structure du Moho. Ce modèle de vitesses de cisaillement est le premier montrant autant de détails et couvrant les Alpes entières, il est proposé que le modèle pourrait servir comme référence pour la région.

Le modèle montre les limites des zones de subduction et les régions de basses vitesses asthénosphèriques montants sous les bassins Ligure et pannonien. Des structures connues comme les déchirures de slabs sous les Apennins et les Dinarides sont imagés. Des découvertes supplémentaires ont été mises en évidence : une petite zone de faible vitesse qui coupe la lithosphère au nord des Dinarides est interprété comme l'expression d'une grande faille décrochante. Dans les Alpes de l'ouest, le slab est limité à une profondeur d'environ 100 km et séparé d'un deuxième slab plus profond. C'est une preuve d'un détachement sous la lithosphère. Par contre, le slab des Alpes centrales est large et montre les anomalies de v_S les plus élevées de tout le modèle. Cette forte anomalie est clairement limitée vers l'est et seulement une anomalie modérée est visible à l'est de la faille de Giudicarie. Ce contraste distinct entre les anomalies des Alpes centrales et des Alpes de l'est est probablement causé par un détachement du slab européen sous les Alpes de l'est. La comparaison avec les modèles d'ondes de volume montrent qu'à une profondeur plus de 200 km, le slab européen est toujours présent. Au-dessus, les résidus du slab européen, un slab adriatique ou une combinaison entre les deux pourraient être la cause de l'anomalie de v_S modérée.

Acknowledgements

I would like to thank my supervisor Lapo Boschi for all his help and encouragement during the last three years. I appreciate that he always had an open ear and his open-minded, enthusiastic and motivating way of supporting me.

I am indebted to my advisors Nicolas Bellahsen and Claudio Rosenberg who supported me in many extremely helpful discussions with their expertise in Alpine geology and dynamics.

I want to thank Thomas Meier for his contributions to this project, the interesting discussions and the encouraging feedback.

I would like to express my gratitude to Sylvie Leroy and Jean-Paul Montagner for their valuable advice during my mid-PhD defense.

I am grateful to all the network operators providing data to the EIDA archive (http://www.orfeus-eu.org/eida).

I appreciate the work of the makers of Obspy (Beyreuther et al., 2010) and Geopsy (www.geopsy.org).

Contents

1 Introduction

In plate tectonic theory, three types of boundaries are distinguished: convergent, divergent and transform boundaries. Convergent boundaries are also termed active margins as they are often linked to mountain building, volcanism and earthquakes, making them zones of high interest to study geohazards but also to improve our understanding of plate dynamics. Major questions comprise the driving forces of plate movements (slab pull, convection, asthenospheric drag, ridge push), the fate of subducted plates, the flexibility or rigidity of tectonic plates and the types of earthquakes that can be induced in plate collisions. Generally, we distinguish between continent-continent, ocean-ocean and continent-ocean collisions. Active continent-continent collisions, such as in the Alps, Apennines and Dinarides, are characterized by high mountains, thick crust and high seismic activity.

The absence of intermediate and deep seismicity makes it necessary to apply tomographic imaging methods to provide information on the subducting slabs underneath the Alps. Large-scale tomographic models show signs of subduction of lithospheric mantle under the central Mediterranean mountain belts, reaching down to the mantle transition zone at 660 km depth (e.g., Wortel and Spakman, 2000; Piromallo and Morelli, 2003; Koulakov et al., 2009). This is evidence of a long history of plate collision, which caused sinking of several hundreds of kilometers of oceanic and continental plates into the mantle (e.g., Handy et al., 2010).

A number of high-resolution P-wave velocity models of the Alpine region are available, imaging the crust (Béthoux et al., 2007; Diehl et al., 2009) and the upper mantle (Lippitsch et al., 2003; Mitterbauer et al., 2011; Dando et al., 2011; Zhao et al., 2016; Hua et al., 2017). So far, however, no similar shear-wave models are available. On a larger scale, S-wave velocity models are calculated by waveform inversions of surface and S-waveforms of regional and teleseismic (Legendre et al., 2012) or of regional seismic events (Zhu et al., 2012) or by inversions including surface-wave dispersion measurements (Auer et al., 2014; Meier et al., 2016). The capabilities of the published models to resolve the crustal structure or the geometry of individual slabs is,

however, limited. The most promising approach to achieve this in the Alpine region is to use surface waves which have a high sensitivity to vertical shear-velocity variations. Surface-wave measurements can be obtained from earthquake and ambient-noise recordings. While teleseismic earthquakes provide signals in a frequency range suited to image the upper mantle, ambient noise can illuminate also very shallow structures from sedimentary basins to the bottom of the crust.
Ambient noise has been used to create group- and phase-velocity maps of the Alps and Apennines (Verbeke et al., 2012) as well as 3-D shear-velocity maps (Molinari et al., 2015). Thanks to an increasing number of seismometer stations in the Alps, the resolution of these models is steadily improving. Imaging the shear-velocity structure of the lithosphere can be used to constrain the composition by studying the v_P/v_S ratio (Lombardi et al., 2008; Giacomuzzi et al., 2012) or the temperature distribution (Goes et al., 2000).

The aim of this thesis is to create a high-resolution shear-velocity model of the crust and uppermost mantle under the Alps, Apennines and Dinarides in central Europe based on both ambient-noise and earthquake data. The new model distinguishes itself from earlier works not only by giving the v_S instead of v_P structure, but also by being continuous between the surface and 200 km depth. Earlier models only constrained either crustal or mantle structures, which leaves an important gap between the Moho and 150–200 km depth, which represents a crucial zone to understand lithospheric delamination, slab break-offs and subduction polarity in the central Mediterranean collision zones.

1.1 Organization of this thesis

The present thesis contains four chapters. The first one gives an introduction to the tectonic setting and geodynamic evolution of the Mediterranean, focusing on the Adriatic microplate and the orogeny of Alps, Apennines and Dinarides. This is followed by an overview of studies relevant for this work of the crust and mantle. A list of the main tectonic questions is presented thereafter. A major part of this study concentrates on the processing, evaluation and validation of the ambient-noise measurements. Thus a short, qualitative introduction to the ambient-noise method and the origin of ambient noise is given. More details are provided within the published article in chapter 2. Details of the earthquake method are not discussed in this work. The corresponding data was provided by Thomas Meier, Riaz Soomro and Amr El-Sharkawy, thanks to a cooperation with the university of Kiel, Germany.

In chapter 2, a published article is given, which presents the theoretical background to the applied ambient-noise method. The method is then tested with a suite of numerical experiments and an extensive comparison with earthquake-based data is presented.

The following chapter 3 includes a second article (submitted), which presents high-resolution v_S models for the crust and upper mantle. Within the article, the procedure to obtain the models is presented and the models of crust and mantle are discussed in light of earlier studies.

The last chapter 4 concentrates on the major tectonic questions regarding the slab geometry in the the Alps and discusses previous tectonic models in comparison with the herein presented shear-velocity model. Also this chapter is written in form of an independent article with the aim of future publication.

1.2 Tectonic setting

In the framework of the convergence of the large Eurasian and African plate, several microplates are involved in the orogenic processes that happen nowadays in the Alps, the Apennines and the Dinarides. In Figure 1.1, the orogenic fronts in the central Mediterranean are shown that limit European, Ligurian and Adriatic plates. The Ligurian plate is mainly composed of the Tyrrhenian and Ligurian basin, which are the result of extensional dynamics due to roll-back subduction of Adria (Faccenna et al., 2014, and references therein). In a similar way, the Pannonian basin formed by roll-back of Adriatic and European plates (e.g., Handy et al., 2015) and is proposed to form a micro-plate of its own (Brückl et al., 2007). The small Adriatic plate assumes an especially important role, representing the upper plate in the collision with Europe, which formed the Alpine and Carpathian arc, but subducting under the Apennines and Dinarides (Fig. 1.1). The junctions between western Alps and Apennines as well as between the eastern Alps and Dinarides therefore represent zones of switching subduction polarity (e.g., Vignaroli et al., 2008; Handy et al., 2015). Reversals in subduction polarity are also known from other active collisional zones, such as in Taiwan (e.g., Ustaszewski et al., 2012) or Pamir-Hindukush (e.g., Kufner et al., 2016).

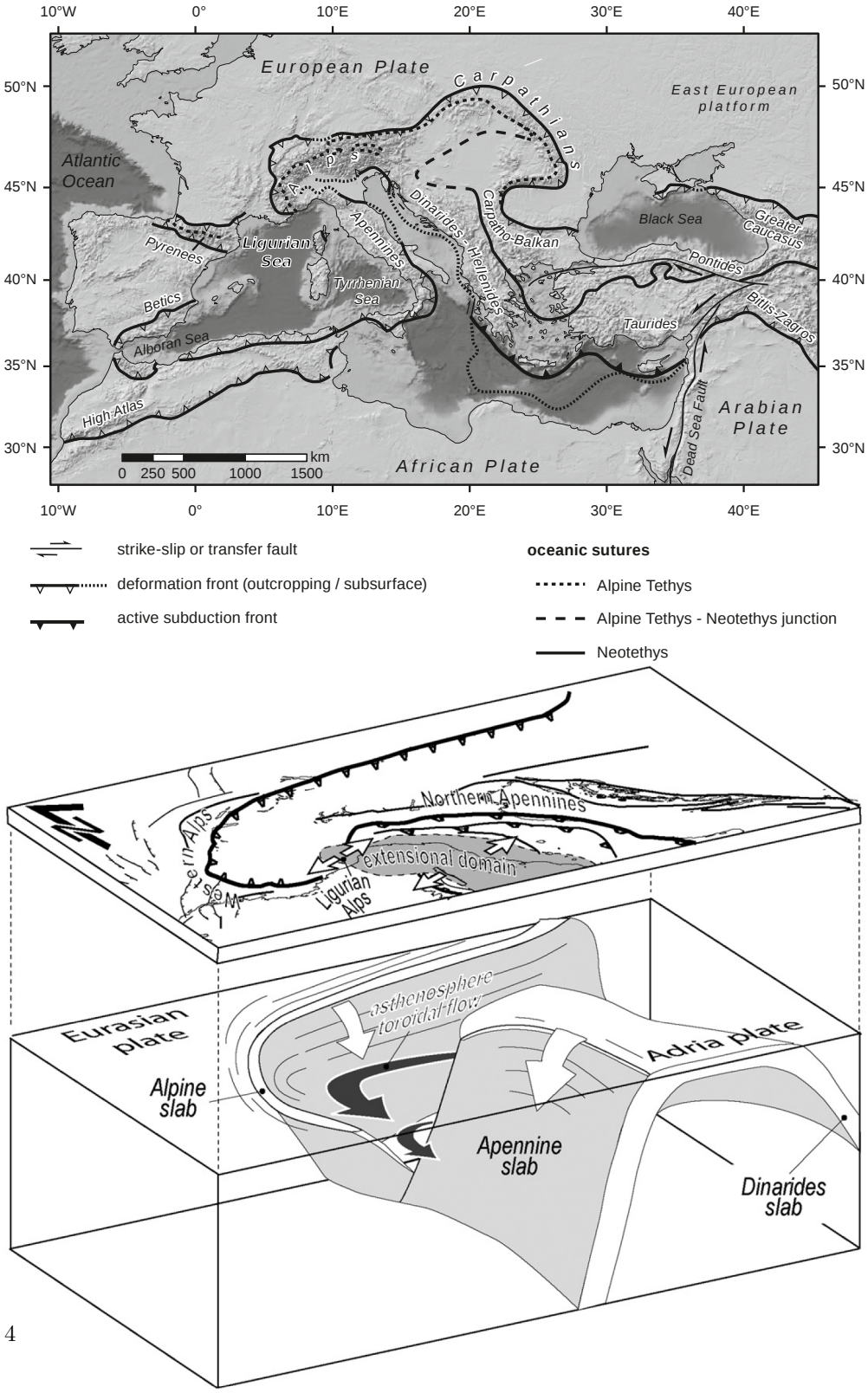

Figure 1.1: **Top:** Orogenic fronts of the Mediterranean chains. Modified after Ustaszewski et al. (2008). **Bottom:** Supposed geometry of the European and Adriatic slab. White arrows give subduction direction, black arrows asthenospheric flow direction. Original figure from Vignaroli et al. (2008).

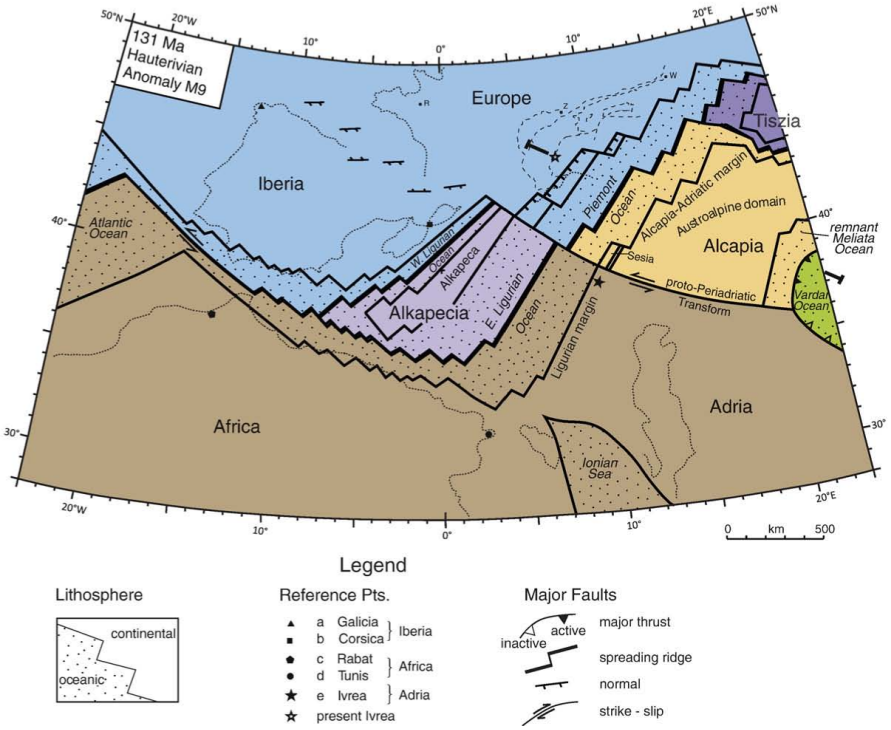

Figure 1.2: Plate tectonic map of the Alpine Tethys (Ligurian and Piemont oceans) and western embayment of Neotethys (Meliata and Vardar oceans). 131 Ma, end of spreading in the Piemont-Liguria ocean. Dotted lines: coastal outlines of western Europe, Iberia, islands in the western Mediterranean Sea (Corsica, Sardinia), southernmost Italy (Apulia(and northern Africa. Dashed lines: current outline of Alpine nappe edifice. City locations for reference on Europe: R - Rennes, W - Wien (Vienna), Z - Zürich. Original figure from (Handy et al., 2010).

1.2.1 Plate tectonic evolution

The formation of the Alps, Apennines and Dinarides is the result of a complex sequence of rifting, break-up of continental blocks, seafloor spreading, subduction and re-amalgamation. Spreading of the Northern and Central Atlantic started in Mid-Jurrasic times (170 Ma) related to a sinistral movement of the African plate with respect to Europe. Kinematically linked to the transcurrent movement, the Alcapia microplate broke-off the northern part of Africa, while further east an intra-oceanic subduction between the Meliata and the Vardar ocean was ongoing (Fig. 1.2 Handy et al., 2010). Three oceanic domains are distinguished that separated Africa and Europe (e.g., Handy et al., 2010) the Paleotethys, the Neotethys and the Alpine Tethys. The Paleotethys is already closed at this time by subduction under Eurasia; Meliata and Vardar oceans are parts of the Neotethys , whose opening was related to a break-off of continental parts from Pangea (Stampfli and Borel, 2002). At the same time, west of the Alcapia plate, the Liguria and Piemont ocean, two domains of the Alpine Tethys, started opening as offshoot of the Central Atlantic spreading (Fig. 1.2 Handy et al., 2010). With the spreading of the Northern Atlantic Ocean jumping northward to the Bay of Biscay at about 145 Ma, individuation and eastward motion of the Iberian microplate began, lasting until 84 Ma (e.g., Capitanio and Goes, 2006).

Around 84 Ma, spreading in the Alpine Tethys had stopped and subduction of its western Ligurian part began towards the east, probably linked to the subduction at the northern boundary of Africa (Fig. 1.3 Handy et al., 2010). The involved northern African segment is referred to as Adriatic plate, which broke-off from Africa at about 118 Ma and later re-amalgamated ($\sim$94 Ma) before it finally separated from Africa around 85 Ma ago (Handy et al., 2010). The convergence between Africa-Adria and Alcapia gave rise to the Eo-Alpine orogeny between 140 Ma and 84 Ma. Around 130 Ma the Meliata-Maliac and Vardar oceans were already closed (Brückl, 2011) and only small relics of the Meliata-Maliac plate were accreted in the the continental collision process (Mandl and Ondrejicková, 1991). Africa-Adria represented the upper plate while the Meliata slab and Alcapia plate got subducted towards the south (Handy et al., 2010). The Eo-alpine orogen forms large parts of today's Eastern Alps represented by the Austro-Alpine nappes of the northern Calcareous Alps that are largely unmetamorphic (e.g., Schmid et al., 2004). But also traces of Eo-Alpine continental subduction can be found nowadays in an E-W trending belt of Late Cretaceous, high-pressure and ultra-high pressure rocks (Thöni et al., 2008). The pressure peak of the metamorphism is attributed to 95–89 Ma (Handy et al., 2010). Handy et al. (2010) interpret the slab pull of the sinking Neotethyan plate as the driving force in this intra-continental collision. When the Adriatic and African plate became re-united

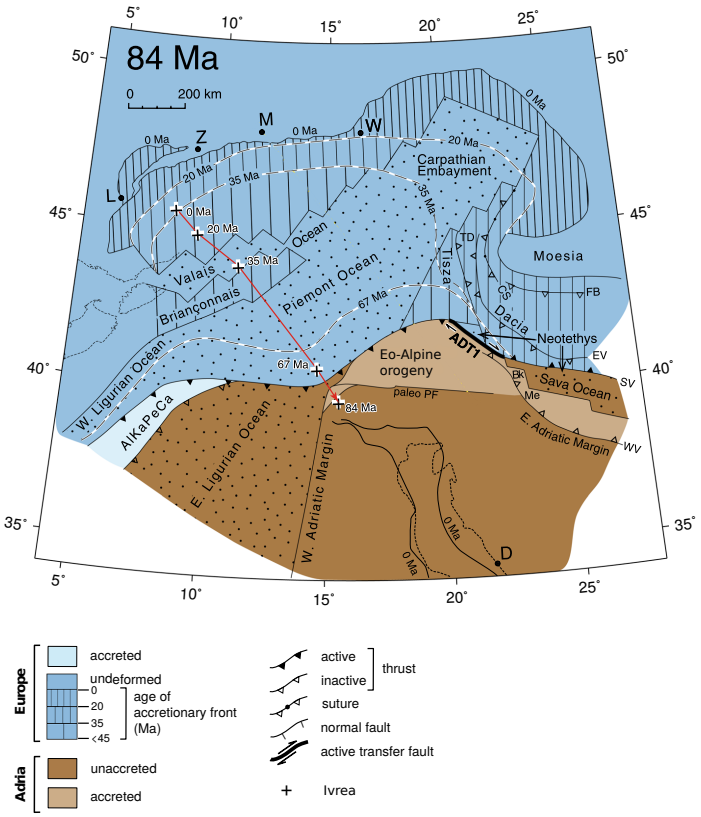

Figure 1.3: Plate tectonic map for 84 Ma, beginning of the subduction of Alpine Tethys (Ligurian, Valais and Piemont oceans). Black crosses connected by a red line show successive locations of Ivrea, defining the Adriatic plate motion with respect to Europe. Dashed black and white lines indicate locations of the Alpine orogenic front at different times. City locations for reference on Europe: L - Lyon, M - München, W - Wien (Vienna), Z - Zürich. Modified from Handy et al. (2015).

between Cenomanian and Santonian times (84 – 94 Ma) it included among others the Eo-Alpine orogen and large parts of the eastern Ligurian ocean (e.g., Channell and Horvath, 1976).
Therefore, Africa-Adria was the upper plate in the Ligurian and Eo-Alpine subduction zones. However, further to the east, subduction of the Adriatic plate under Europe started at least 92 Ma ago (Handy et al., 2015). It is proposed by Handy et al. (2015) that opposing directions of Eo-Alpine and Dinaric subduction have to be linked by a major transform fault, denominated ADT1 in Figure 1.3, and they infer that continental collision in the Dinarides started around 67 Ma.

The NNW movement of the African promontory was accompanied by a 2000 km long oceanic subduction margin reaching from the Eastern Alps to Southern Spain (Handy et al., 2010). Adria-Africa acted as upper plate and the Alpine Tethys, attached to the European margin, was subducted between 84 Ma and 35 Ma (Fig. 1.4. Handy et al. (2010) infer that the subduction slab had already reached the top of the mantle transition zone (410 km) at 84 Ma, successively sinking further down and accumulating at the 660 km boundary. Beginning around 67 – 56 Ma, the Adriatic plate separates again from Africa, linked to an increase in convergence rate between Adria and Europe, spreading of the Ionian sea between Africa and Adria and a counterclockwise rotation of the Adriatic plate (Nocquet and Calais, 2004; Handy et al., 2010).

The continental collision at 35 Ma causes important changes: in the north, the relative velocity of Adria towards Europe decreases to about 0.3 cm/year (Savostin et al., 1986). Handy et al. (2010) propose that the ongoing northward drift of Africa is compensated by subduction of the Ionian sea, between Africa and Adria, until it stopped at 20 Ma and the convergence is entirely accommodated by indentation of the Adriatic crust into the European continent. In the south-west, the remaining part of the eastern Ligurian sea starts subducting towards the west underneath Europe and Iberia, meaning a switch in subduction polarity (e.g., Vignaroli et al., 2008). This took place as a rollback subduction, causing extension and the opening of the western Mediterranean Sea (Ligurian and Tyrrhenian basin, Fig. 1.5).

The tip of the Adriatic plate in the Central and Western Alps is characterized by a shallow wedge of mantle rocks that were already exhumed in the Jurassic and are known as the Ivrea (geophysical) body causing a gravitational and seismic anomaly (e.g., Handy et al., 2010, crosses in Fig. 1.3 and 1.4). The European subduction slab in the Western Alps is inferred to have started breaking off in the late Miocene,

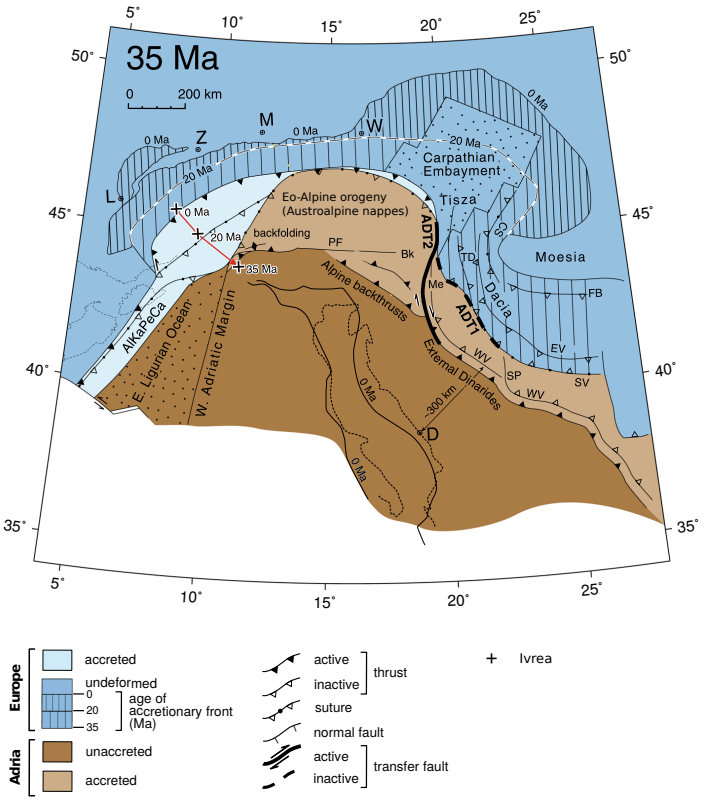

Figure 1.4: Plate tectonic map for 35 Ma, beginning of the continent collision in the Alps and Dinarides. 300 km arrows gives estimated shortening in the Dinarides, assuming a 20° rotation of Adria (Handy et al., 2015). Black crosses connected by a red line show successive locations of Ivrea, defining the Adriatic plate motion with respect to Europe. Dashed black and white lines indicate locations of the Alpine orogenic front at different times. City locations for reference on Europe: D - Dubrovnik, L - Lyon, M - München, W - Wien (Vienna), Z - Zürich. Modified from Handy et al. (2015).

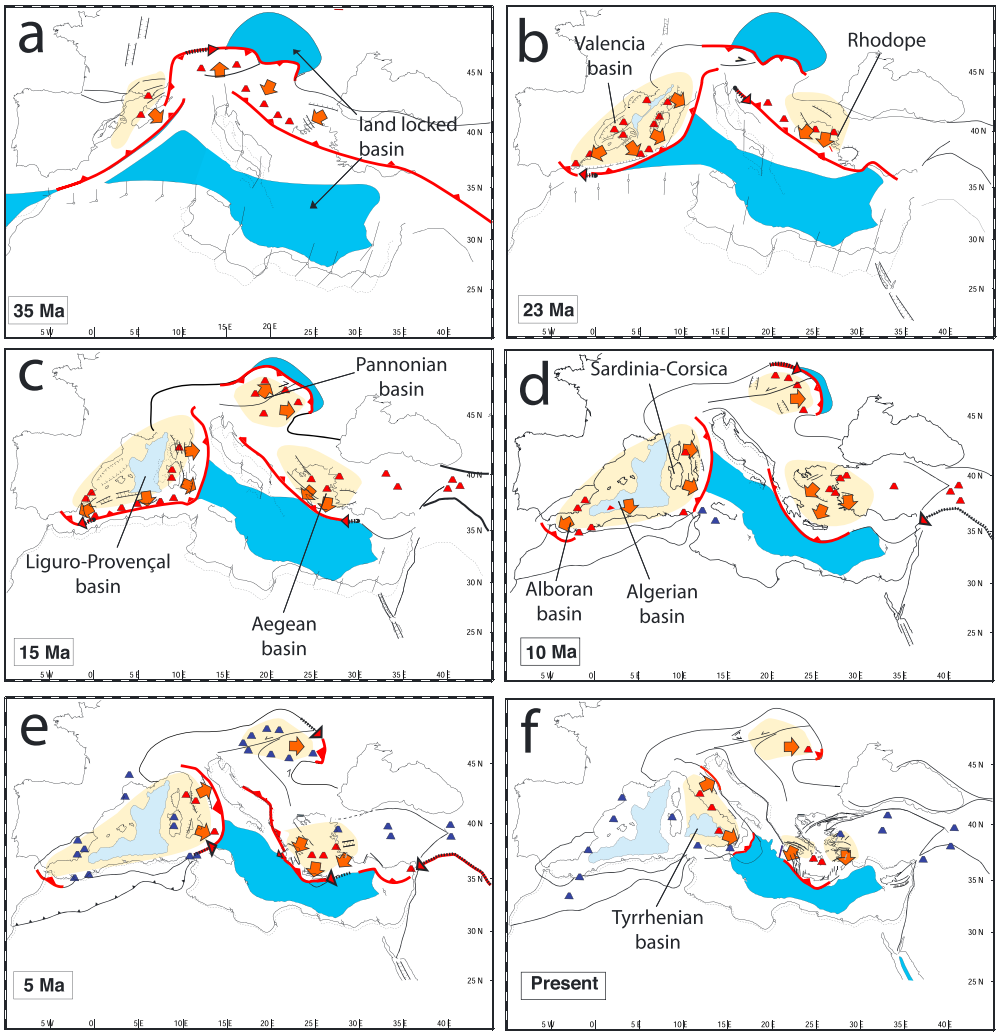

Figure 1.5: Plate tectonic evolution from 35 Ma to present. Red lines indicate active subduction. Red and blue triangles stand for calcaline and anorogenic volcanic activity, respectively. Yellow areas are zones of stretching and arrows indicate the direction of stretching. Original from Faccenna et al. (2014).

coinciding with a strong decrease in WNW-ESE convergence rate (Blanckenburg and Davies, 1995; Wortel and Spakman, 2000; Handy et al., 2010). Handy et al. (2010) argue that this break-off may have propagated from the Western to the Central and Eastern Alps, leaving a remnant European slab still attached to the European plate of about 160 km of continental lithosphere; the detached part would have sunken into the mantle and accumulated at the mantle transition zone. They remark, however, that propagation and timing of the slab break-off, as well as relation of the slab parts, as seen in tomography, to their associated plates, are still a matter of debate.

1.2.2 Previous studies

A main feature of this work is a lithospheric shear-velocity model of central Europe. It is the basis for an interpretation and discussion of the structures in the crust and mantle in comparison with previous studies and the plate tectonic history. Thus, a short overview of relevant studies, without claim of completeness, will be provided here.

Crustal structure

Kummerow et al. (2004), among others, discuss the results of the TRANSALP experiment (TRANSALP Working Group et al., 2002; Lüschen et al., 2004; Bleibinhaus and Gebrande, 2006; Castellarin et al., 2006), a north-south seismic profile crossing the eastern Alps through the Tauern window (Fig. 1.6). In the context of this thesis it is interesting as the Moho structure derived from the experiment has been interpreted to show either the Adria as upper plate (TRANSALP Working Group et al., 2002) or Europe (Schmid et al., 2004). Schmid et al. (2004) also summarize results from similar large-scale Alpine cross-section experiments in the central and western Alps (ECORS-CROP: Hirn et al. (1987); ECORS et al. (1989); Bois and Party (1990); Roure et al. (1996), NFP-20: Pfiffner et al. (1997)), where it is general consensus that Europe is the underthrusting plate.

Diehl et al. (2009) create a crustal 3-D P-wave velocity model based on local earthquakes, which covers most of the Alps and the northern Apennines. It shows location and size of the Ivrea body and fits well earlier Moho depth estimations of Waldhauser et al. (1998).

Grad and Tiira (2009) create a Moho-depth map of Europe by combining data from 3-D body- and surface-wave models, receiver functions as well as seismic and gravity

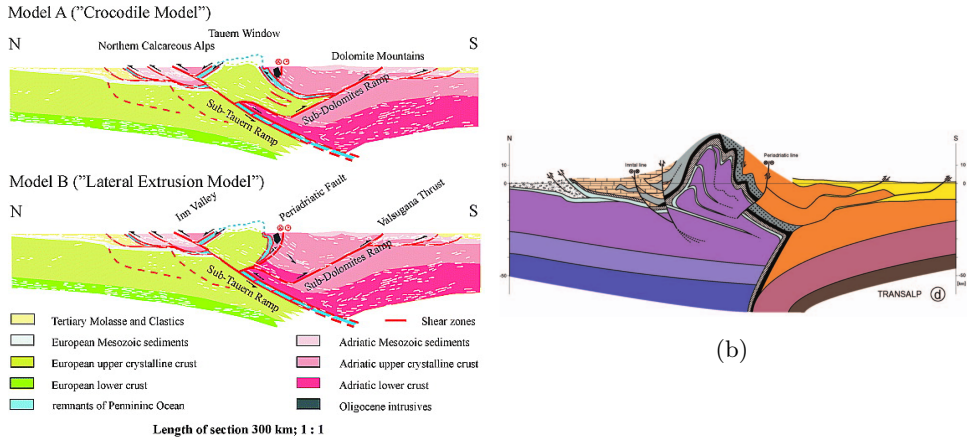

(a) (b)

Figure 1.6: TRANSALP cross-section interpreted by (a) TRANSALP Working Group et al. (2002) and (b) Schmid et al. (2004).

data. The greatest Moho depths are found in the eastern Alps with about 50 km. A very shallow Moho is present in the Ligurian and Tyrrhenian basin with only 15 km depth. BRÜCKL and Hammerl (2014) combine the results with the Moho information of Waldhauser et al. (1998) and Behm et al. (2007) to create a model for the eastern Alps and northern Dinarides. From this data they infer that the Pannonian basin is part of a separate plate, containing the remnants of Alcapa and Tisza (compare Fig. 1.2). This clear separation has not yet been reported by other groups.

Spada et al. (2013) present a Moho-depth model combining data from controlled-source experiments and receiver functions (Fig. 1.7). It covers a large area including the Alps, Apennines and parts of the Dinarides and is therefore similar to the study area of the presented thesis. It provides valuable information on the jumps in Moho depth at the plate boundaries. A zone of higher uncertainty is identified in the eastern Alps, which is excluded from the Moho map (corresponding to the area of diverging interpretations in Lüschen et al. (2004) and Schmid et al. (2004), mentioned above). In this thesis it is estimated that the model of Spada et al. (2013) is the most reliable and complete model of crustal depths and it is used as reference throughout this work when comparing the Moho structure.
The Moho discontinuity of the European plate increases from 28 km in the Alpine foreland to 50 km in the western and 60 km in the central Alps, at the junction with

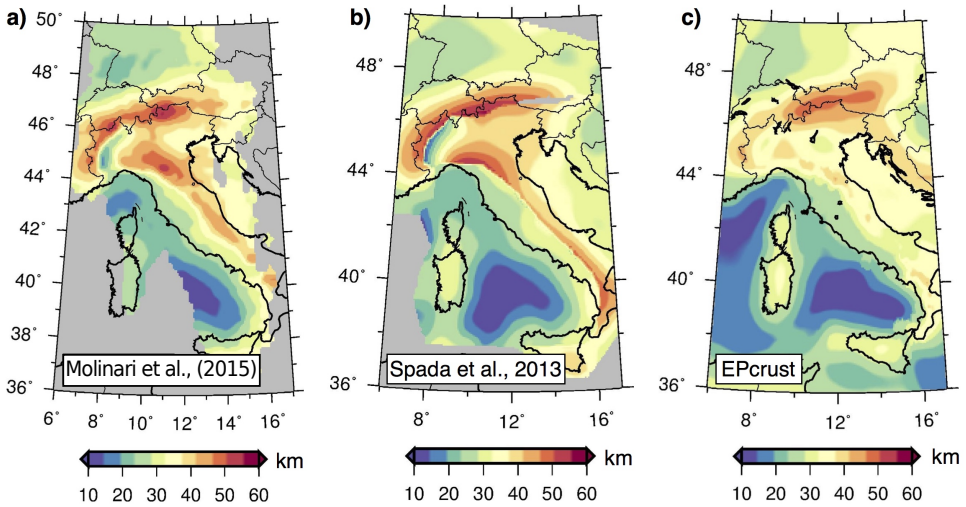

Figure 1.7: Comparison of Moho maps from (a) ambient noise (Molinari et al., 2015), (b) receiver functions and controlled source experiments (Spada et al., 2013) and (c) a combined model from different studies (Molinari and Morelli, 2011). Figure modified from (Molinari et al., 2015).

the Adriatic plate (Spada et al., 2013). Along the suture with the Adriatic plate it shows a sharp step of about 20 km. In the eastern Alps the Moho geometry is more symmetric and no jump between Adriatic and European Moho is imaged. The greatest Moho depths of the Adriatic plate are found under the northern and southern ends of the Apennines with depths reaching to more than 50 km.

Molinari et al. (2015) use ambient-noise phase- and group-velocity measurements in the Alps and Apennines, in continuation of the work of Verbeke et al. (2012), to derive a 3-D shear-velocity model of the crust. The approach of is analogue to the one in this thesis, however, in this work more data (Love waves, earthquake surface-wave measurements) are included and an updated and more thorough processing scheme is applied to obtain a model with larger extent and higher resolution. Molinari et al. (2015) show that the Moho depth estimates from ambient noise are in good agreement with previous studies (Fig. 1.7) and that main crustal features (e.g. Ivrea body) can be resolved.

Zhao et al. (2015) interpret receiver-function data from the CIFALPS experiment in the western Alps to show subduction of European crust down to 75 km. This depth is greater than other estimates of Spada et al. (2013) or Hua et al. (2017). They also show how the subducted crust is overlain by the Ivrea body.

Mantle structure

Many tomographic studies have been conducted in central Europe that illuminate the upper mantle structure with body waves. A large-scale picture of the entire Mediterranean region is provided by the teleseismic body-wave models of Wortel and Spakman (2000) (P waves), Piromallo and Morelli (2003) (P waves, Fig. 1.8), Spakman and Wortel (2004) (P waves) or Koulakov et al. (2009) (P and S waves). These models show high-velocity anomalies under the Alps, Apennines and Dinarides that are interpreted as subducted lithosphere of Europe and Adria. They also show a slab gap under the southern Apennines, where no fast anomaly is visible above $\sim$ 200 km depth. This may be an indication of onsetting slab break-off. Another gap structure becomes evident in the northern Dinaric subduction zone, where the otherwise continuous slab from the Hellenic subduction vanishes below $\sim$ 150 km depth (Fig. 1.8). This gap in the Dinaric subduction is possibly related to the asthenospheric upwelling during the extrusion of the Carpathians (Handy et al., 2015).
At depth greater 410 km, the entire region surrounding the Alps, Apennines and Dinarides is underlain by high-velocity anomalies (Fig. 1.8) that are interpreted to represent the remnants of the subducted Tethys ocean (e.g., Handy et al., 2010).

Other regional body-wave models concentrate on parts of the Mediterranean collision zone, such as the eastern Alps and Pannonian basin (Dando et al., 2011; Ren et al., 2012), the Alps (Lippitsch et al., 2003), the central and eastern Alps (Mitterbauer et al., 2011), the Alps and Apennines (Zhao et al., 2016) or the Alps, Apennines and Dinarides (Hua et al., 2017). The first order structures agree well between all these models, however, some interpretations show important differences: Lippitsch et al. (2003) find a northward dipping slab under the eastern Alps that has been inferred to be an indication of the subduction of the Adriatic plate (Schmid et al., 2004; Ustaszewski et al., 2008; Handy et al., 2015, Fig. 1.9). This interpretation is supported by Zhao et al. (2016) and Hua et al. (2017) but not by Mitterbauer et al. (2011) who argue that the slab dip is rather vertical and propose that the European slab is detached under the eastern Alps. This theory agrees with the SKS-wave splitting model of Qorbani et al. (2015) who define two anisotropic layers under the eastern Alps with different fast axis direction (Fig. 1.10). They relate the shallower one to asthenospheric mantle and the deeper one to the detached European slab.
Another discussion evolves around the suggested detachment of the European slab under the lithosphere of the western Alps (Lippitsch et al., 2003). Zhao et al. (2016)

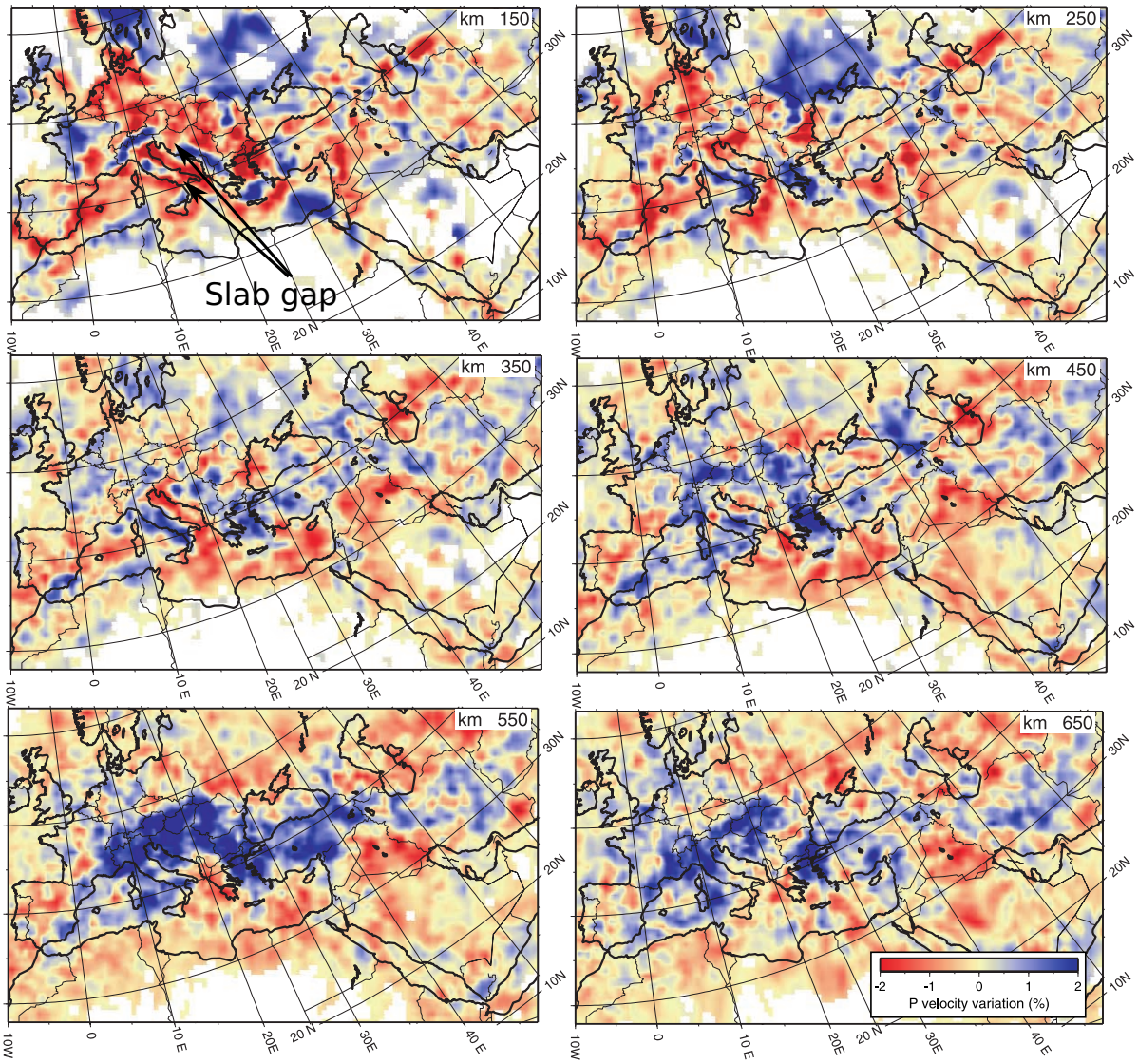

Figure 1.8: Mantle anomalies under the Mediterranean from teleseismic P-wave body-wave tomography. Figure modified from Piromallo and Morelli (2003).

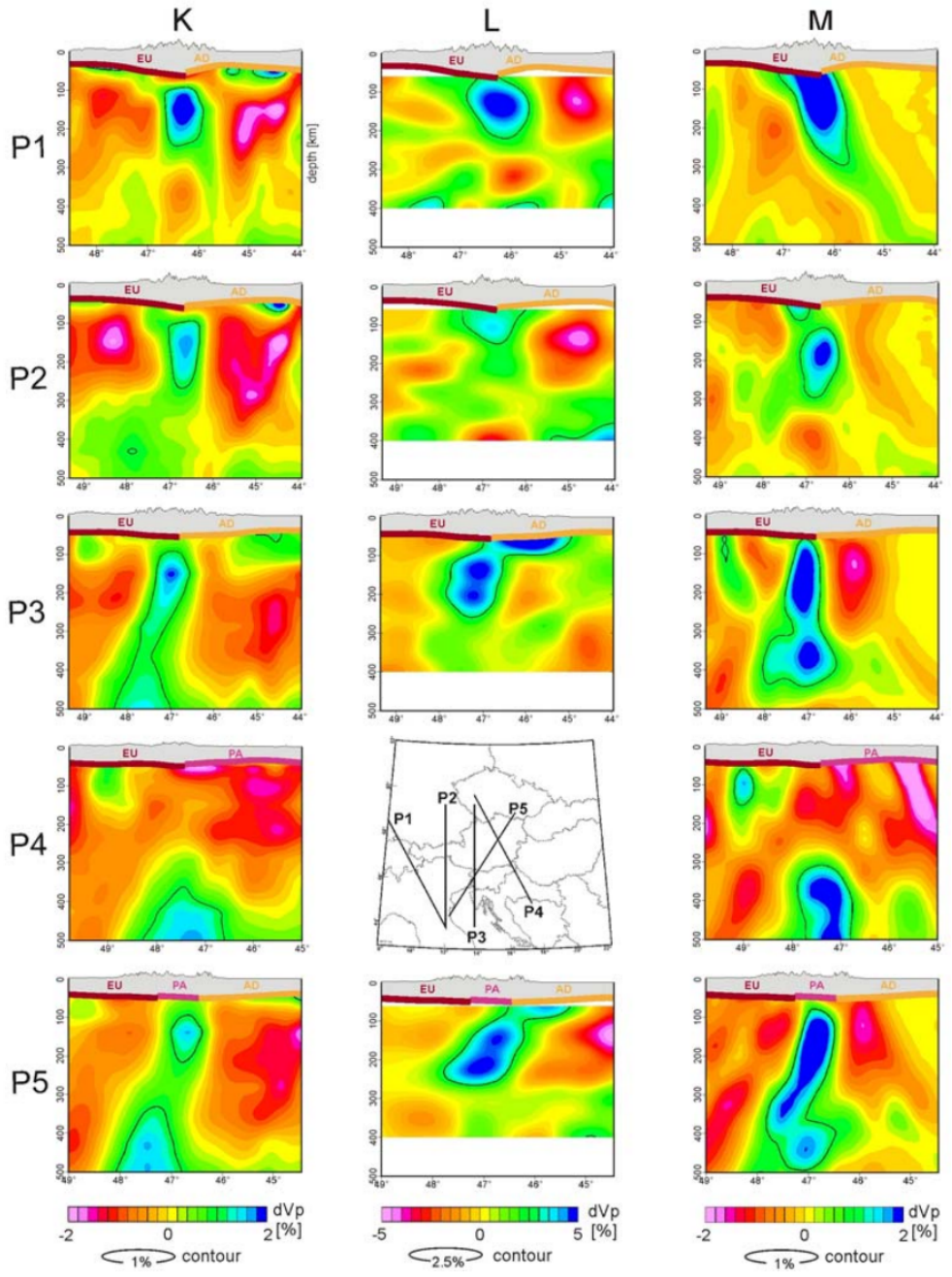

Figure 1.9: Comparison of cross-sections through the mantle under the eastern Alps taken from the models of Koulakov et al. (2009) (K), Lippitsch et al. (2003) (L) and Mitterbauer et al. (2011) (M). Abbreviations of the Moho boundaries indicate European (EU), Adriatic (AD) and Pannonian (PA) Moho. Original figure from Brückl (2011).

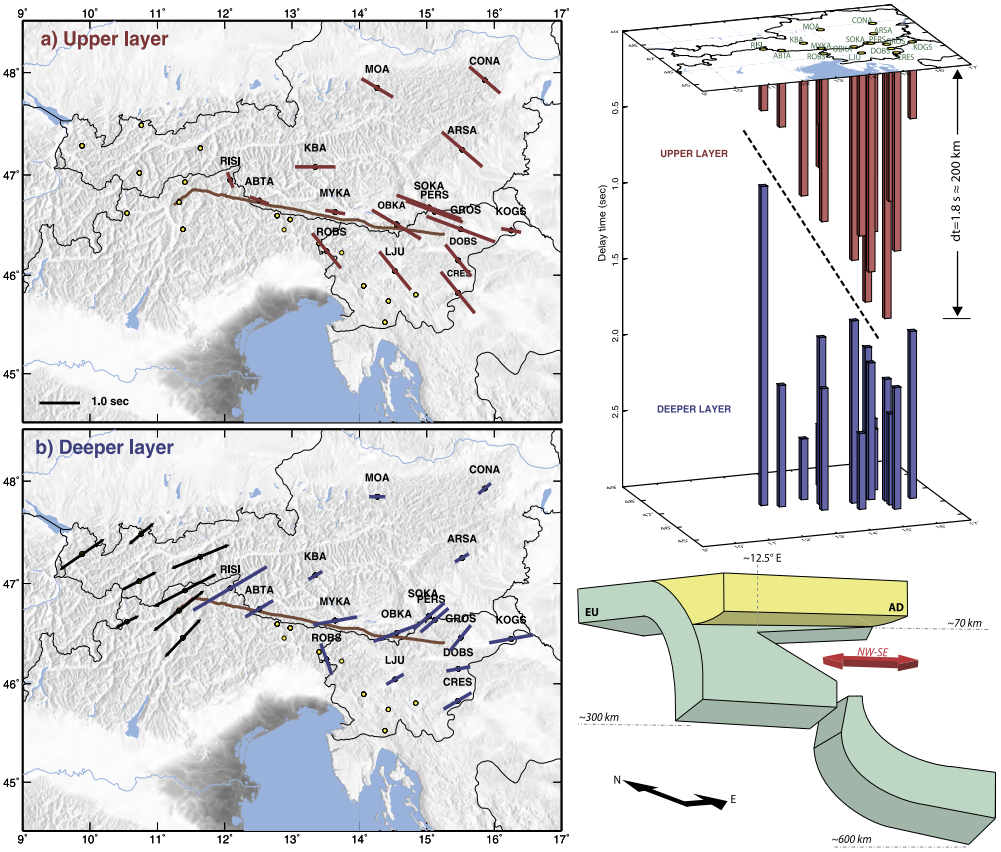

Figure 1.10: Layered anisotropy from SKS-wave splitting in the eastern Alps. Lines in the two maps give the anisotropic fast direction. The top layer is interpreted as asthenosphere and the bottom layer as detached European lithospheric slab. Original figure from Qorbani et al. (2015).

find a link between deeper slab and the lithosphere and conclude that the slab is still attached. They furthermore doubt that there was any slab detachment in the Alps and Apennines, contrary to the proposition of oceanic slab detachment at 35 Ma which is often inferred to explain volcanic activity that coincides temporally with the continent collision (e.g., Blanckenburg and Davies, 1995).
In the central Alps all models show that the upper mantle slab is still attached to the lithosphere, however, at depth below 160 km there is no agreement whether the oceanic part of the slab has detached (Lippitsch et al., 2003) or not (Zhao et al., 2016).

1.2.3 Main tectonic questions

The primary tectonic questions in the Adriatic plate collision can thus be summed up as follows:

- **Is there evidence of current and past slab detachments under the subduction zones that could explain volcanic activity or uplift?**
  The theory of past slab detachment of the oceanic slab is largely based on the Cenozoic magmatism along the orogens that coincides temporally with the continental collision (e.g. Blanckenburg and Davies, 1995). In the Apennines, Dinarides and also western Alps, asthenospheric upwelling due to slab retreat may, however, be of greater importance (Zhao et al., 2016). Adriatic subduction in the easten Alps would probably require a previous break-off of the European slab (Ustaszewski et al., 2008; Handy et al., 2015). Lippitsch et al. (2003) show in their model that the European slab in the western Alps seems detached directly below the lithosphere, however, other authors show a more continuous slab (Koulakov et al., 2009; Zhao et al., 2016). Singer et al. (2014) assume that slab break-off in the central Alps is causing crustal earthquakes in the foreland due to a redistribution of stresses after crustal detachment.

- **What is the nature of the slab gap in the southern Apennines? Could it be evidence of the onset of a shallow (above 200 km) slab detachment?**
  Counter-clockwise rotation in the northern Italy has been significantly less than in southern Italy, showing a main transition between 40°N and 41°N (Carminati and Doglioni, 2012), which coincides with the approximate location of the slab gap. Zhao et al. (2016) relate the slab gap to major faults on the surface. Below 200 km, the slab seems to be continuous from north to south, which could indicate that the slab tearing happened at a later stage of subduction when the

differential subduction rates from north to south became too large or that the tear propagated downwards from the surface.

- **What caused the slab gap in the Dinarides and where did the deep slab vanish?**
  In most parts of the Hellenic subduction zone the slab can be trace from the lithosphere down to the mantle discontinuties, however, in the Dinarides, no fast slab anomaly is found in tomographic models below about 150 km (Piromallo and Morelli, 2003; Koulakov et al., 2009). Considering the continuous slab in the Hellenides and that a significant amount of shortening is likely to have occurred in the Dinarides (Schmid et al., 2008; Ustaszewski et al., 2008), it raises the question of what happened to the deeper part of the slab. It is possible that in the transition from south-directed European subduction in the Alps to north-east directed subduction in the Dinarides and Hellenides the convergence in the northern Dinarides was significantly decreased and the deeper slab broke off. Another possibility is the interaction with the upwelling asthenosphere in the Pannonian basin (Faccenna et al., 2014).

- **Is the Adriatic plate subducting in the eastern Alps and to which depths?**
  The idea of northward subduction of Adria under the eastern Alps is mainly based on the apparent northward dip of the fast upper mantle anomaly under the eastern Alps and it has been proposed that the slab reaches to depths of 250–400 km (Lippitsch et al., 2003; Zhao et al., 2016; Hua et al., 2017). This contradicts shortening estimates of the Adriatic crust in the southern Alps that are in the order of 50 km (Schönborn, 1999; Nussbaum, 2000). Handy et al. (2015) estimate that the Adriatic slab should not be longer than 190 km. Mitterbauer et al. (2011) state that there is not enough evidence to assume Adriatic subduction in the eastern Alps. The situation is further complicated due to the continuous transition of the anomalies from eastern Alps to northern Dinarides. In the latter it is widely accepted that the Adriatic plate is subducting to the northeast, although during the last 20 Ma the region may have been mostly affected by transform faulting and only low subduction rates (Ustaszewski et al., 2008). Tomographic images in the transition zone may sometimes rather show the Dinaric slab than the eastern Alpine one.

- **What is the origin of the deep slab under the eastern Alps? If it is part of the European subduction, what caused the apparent northward**

dip?
Despite the assumption of a maximum Adriatic slab depth of 250 km in the eastern Alps (Handy et al., 2015), it has been proposed that northward dipping Adria may reach to more than 400 km depth (Zhao et al., 2016; Hua et al., 2017). The eastern Alpine slab seems furthermore continuous with a deep anomaly under the Pannonian basin, which suggests European origin of the slab. In this case the question remains what processes have steepened or even overturned the European slab under the eastern Alps?

1.3 The ambient-noise method

In seismic recordings the signal is typically understood as ground movement caused by seismic waves that were excited during an earthquake or an active, i.e. man-made experiment. The rest of the signal that is not associated to a specific source of interest, is summed up as noise. Noise can have several reasons such as instrument noise, atmospheric pressure or temperature fluctuations, vibrations due to traffic, industry or natural sources. Not all of these types of noise are associated with seismic waves, but if they are, then they are also a potential source for ambient-noise methods in seismology.

A main difference between "classical", earthquake-based measurements and ambient-noise recordings is that ambient noise is often very weak in its amplitude and the sources are less localized. Ambient-noise signals are therefore rather the combination of many randomly traveling seismic waves that interact and create an approximately diffuse wavefield. Individual sources that contribute to this wavefield cannot be separated nor can the signal be traced back to a unique source location. The advantage is, however, that we can measure this wavefield basically everywhere on Earth, independent of earthquake-generating structures such as active fault zones.

In this chapter, a qualitative description of the ambient-noise method is given. A more technical derivation is presented in the article in chapter 2 or can be found in the review articles of Wapenaar et al. (2010a,b), Campillo et al. (2014) or Boschi and Weemstra (2015).

1.3.1 Principle of ambient-noise correlations

The idea to use ambient noise in seismology goes back to the original work of Aki (1957), who showed that by correlation of signals we can extract the coherent parts

of the wavefield, i.e. the waves that travel between different recording stations. By stacking and summing these coherent contributions we can enhance the signal and get rid of cross-terms, i.e. spurious correlations. These spurious correlations are due to many simultaneously acting sources that contribute to the correlation but contain no usable information. This work concentrates on regional (countries/parts of continents) experiments where the stacking and summing process will be performed over time spans between several months to few years. Applied to a pair of seismometer stations and under ideal conditions, the thus obtained signal is identical to a signal traveling directly from one station to the other. More precisely speaking, it gives us the Green's function, i.e. the response of the medium for an impulse traveling between the stations (e.g., Boschi and Weemstra, 2015). The Green's function contains therefore valuable information on the medium along the path of the wave and can be used to derive the structure and the material properties between the station pair.

In Figure 1.11 a 2-D case is presented where two stations at x_A and x_B are surrounded by a circle of uniformly random distributed noise sources. In this example it is assumed that the noise source are not active at the same time and that each one emits a simple impulse that travels through the isotropic medium to both stations. The signals recorded at both stations (Fig. 1.11b and c) are cross-correlated and give the differential arrival time of the impulse, according to the azimuth ϕ_S of the noise sources (Fig. 1.11d). If the cross-correlations over all azimuths are summed, all contributions of sources that are not aligned with the station pair will cancel out (Fig. 1.11e). The summed trace represents therefore an estimate of the (time-integrated) Green's function, i.e. an impulse traveling from station A to station B and vice versa, causing the two peaks in Figure 1.11e at ± 0.6 s. More precisely it gives the forward and backward Green's function convolved with the autocorrelation of the source signal. This autocorrelation will disappear if the sources have random signals. Figure 1.11f shows also the summed cross-correlations when the sources are simultaneously active. The non-perfect cancellation of the cross-terms causes the higher noise around the Green's functions' peaks.
The dashed lines in Figure 1.11a and d indicate the Fresnel zones, i.e. the area where the noise sources contribute constructively to the Green's function reconstruction. The size of the two hyperbolae depends on the period of the sources' signals and are larger with increasing period.

The estimated Green's functions can be used to extract the travel-time information of a wave traveling between station A and B. In this thesis, exclusively surface waves

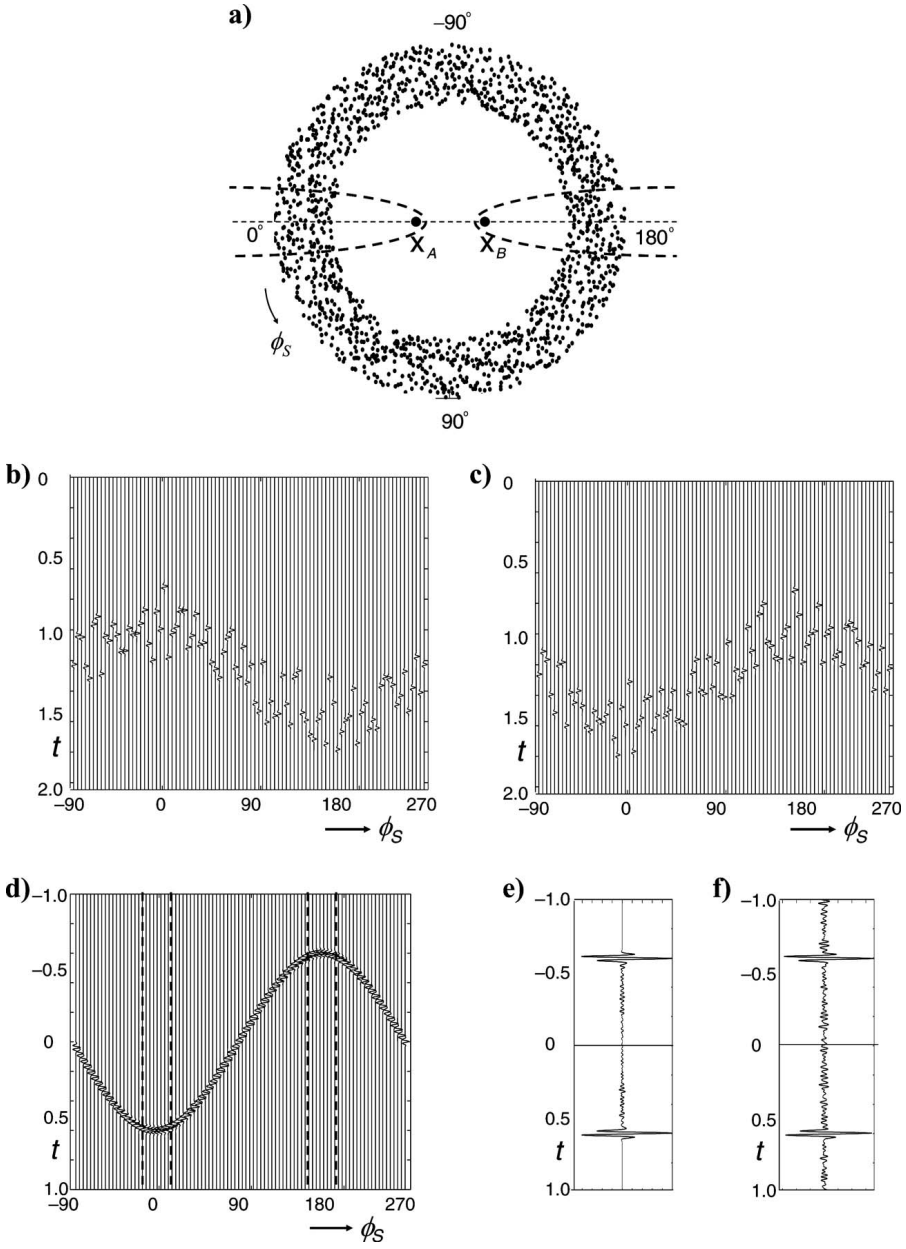

Figure 1.11: Principle of ambient-noise interferometry. **a)** Location of the two stations x_A and x_B surrounded by noise sources. The dashed parabola indicate the Fresnel zone where sources contribute constructively to the cross-correlation. **b)** Signals recorded at x_A according the the source azimuth ϕ_S. **c)** Same for station x_B. **d)** Cross-correlations of the signals at x_A and x_B. Dashed lines give the Fresnel zones. **e)** Summed cross-correlation over all azimuths from **d)**. **e)** Single cross-correlation of the signals at x_A and x_B for simultaneously acting sources. Original from Wapenaar et al. (2010a).

are used for the analysis as in most cases they are the most energetic source of noise (Friedrich et al., 1998). The summed cross-correlations are thus used to extract dispersive phase-velocity information between the station pairs. However, the same method can also be used to obtain the Green's function of body waves (e.g., Poli et al., 2012).

1.3.2 Origin of ambient noise

The most important role in regional ambient-noise seismology play signals generated by pressure fluctuations on the sea floor, which are caused by surface gravity waves, i.e. ocean surface waves. They are usually referred to as microseisms and are observable basically everywhere on earth. In a seismometer spectrum, these signals can be recognized as the two most energetic peaks, the so-called microseism peaks. The single-frequency or primary microseism peak is centered around 14 s and is weaker in amplitude compared to the double-frequency or secondary microseism peak around 7 s. Apart from that, there is also seismic hum which summarizes all the long period noise above 30 s, which is less energetic and less centered on a specific period compared to the two aforementioned spectral peaks.

The primary microseism peak

In shallow water, surface gravity waves interact with the sea bottom, exciting a pressure field. A special case would be an undulating sea-floor topography, similar in its wavelength to an ocean wave. The ocean wave itself will not excite any seismic waves as its phase speed is not in the range of seismic speeds, which are much higher. However, the interaction of undulating sea floor and surface gravity wave causes pressure fluctuations with group velocities that corresponds to seismic wave speeds (Hasselmann, 1963; Ardhuin et al., 2015). In a more realistic scenario, shallowing sea floor, e.g. at continental shelves will similarly modulate the phase velocity of the pressure field. Ardhuin et al. (2015) show how a surface-gravity wave, when propagating over an inclined ocean floor, causes a pressure dipole on the sea bottom that excites seismic waves. The shallowing ocean depth causes an increase in wave amplitude, augmenting the bottom pressure, and a decrease in wavelength, reducing the bottom pressure. The dipole evolves around the equilibrium point, which depends on the ocean wave's wavelength and the water depth. A surface gravity wave with 50 s period propagating over a monotonously shallowing sea floor would generate seismic waves of equal period around the point of 300 m ocean depth (Ardhuin et al., 2015). The slope controls the amplitude of the generated wave. This means that long period microseisms

(greater 30 s) originate mainly at the shelve breaks, while the primary microseisms, typically around 14 s, are generated by sea-floor topography on the continental shelves.

The secondary microseim peak

Similar to the case of an undulating sea floor, interaction of two surface-gravity-wave trains can cause wave groups with high velocity. This effect is largest for waves traveling in opposing directions with almost the same frequency (if they had the same frequency, it would create a standing wave, meaning infinite group velocity). Such an ocean wave group gives rise to pressure waves propagating vertically downward through the fluid, thus independent of ocean depth (Miche, 1944; Longuet-Higgins, 1950; Hasselmann, 1963). This means that the mechanism causing secondary microseisms can act anywhere in the oceans and is not limited to shallow water as the primary mechanism, as long as the excited pressure fluctuations at the ocean bottom meet seismic wave speeds (Ardhuin and Herbers, 2013). In the case of two waves with similar, but opposing wave number and almost identical frequency, the resulting wave group will have twice that frequency, therefore the alternative denomination double-frequency microseisms (Hasselmann, 1963; Ardhuin and Herbers, 2013). Of course, in the ocean, waves of different frequencies and wavenumbers interact at all times, but the opposing wavenumber and similar frequency case is the most effective one for the excitation of seismic waves. Traer and Gerstoft (2014) show that also obliquely interacting waves are an important source of secondary microseisms and hum, however this case might be more important in shallow water as in this case the pressure waves are evanescent at large depth. Opposing waves can be generated for example by two storms or by reflection at the coastlines.
The fact that primary microseisms are observed mostly around 14 s and secondary microseisms at half that period indicates that the spectrum of surface-gravity waves in the oceans should also have a peak at 14 s. Indeed, ocean wave spectra show a clear peak between 10 and 20 s, but not the double-frequency peak (e.g., Haubrich et al., 1963). As excitation of microseismic sources is directly caused by ocean waves, which are in turn related to storm activity in the oceans, it becomes clear that there are strong seasonal shifts in the microseismic activity (e.g., Hillers et al., 2012). Storm occurrence coincides typically with the winter season in the respective hemisphere. Consequently, in ambient-noise seismological applications, often year-long recordings are used in order to have an equal intensity of noise sources from all directions.

1.3.3 Main methodological questions

- **How reliable are ambient-noise derived phase-velocity measurements?**
  The theory behind the ambient-noise method (see above and chapter 2) is subject to several assumptions. The noise sources are assumed to be independent and randomly distributed in the far field, generating a diffuse wave field. The measurements may also be influenced by non-homogeneous structures, attenuation, higher modes and the presence of several wave types in the noise signal (body- and surface-waves, earthquake signals, repetitive signals). In chapter 2 a set of synthetic tests is presented to show how some of these effects may influence the ambient-noise measurements. Similar tests have been performed before (e.g., Tsai, 2009; Weaver et al., 2009; Yao and Van Der Hilst, 2009; Sadeghisorkhani et al., 2017). However, some of these sources of error are difficult to test for and may influence each other. In order to validate the measurements, a comparison with the more classical earthquake-based two-station method is performed in a more thorough fashion than earlier studies (e.g., Yao et al., 2006; Yang and Ritzwoller, 2008; Zhou et al., 2012; Shen et al., 2013; Xie et al., 2016). The two approaches use different data and are based on different methods but measure the same quantity (phase or group velocity of surface waves between station pairs). Comparison can thus give a good estimate of the reliability of both methods.

- **What is the quality of measurements from horizontal components, i.e. Love waves and radial component Rayleigh waves?**
  In ambient-noise studies it is becoming increasingly popular to not just use the Z-component (vertical) of the wave field, but all three components (Z, R, T) to obtain surface-wave phase- or group-velocity measurements (e.g, Campillo and Paul, 2003; Bensen et al., 2008; Lin et al., 2008; Yang and Ritzwoller, 2008; Li et al., 2010; Ekström, 2014). Within this procedure it has often been ignored that the relation of Green's function to the stacked ambient-noise cross-correlations is different for Z- and T-/R-component (Haney et al., 2012). The R-component measurements can be used to double check the Rayleigh-wave measurements made on the Z component and the T-component measurements are used to obtain Love-wave velocities.

- **What degree of detail can be resolved with the combination of ambient-noise and earthquake-based surface-wave measurements?**
  Surface waves from ambient noise are most energetic around the two microseismic peaks at 7 and 14 s period. In this work, phase-velocities are extracted between 4 and 75 s. At shorter periods the noise signal is too attenuated for the typically

given station distance in the used networks. At longer periods the signal is not energetic enough, however, with the two-station earthquake method the period range is extended to 250 s. Greater period means greater depth sensitivity of the surface waves due to longer wavelength. The wavelength (approximately 10 km at 4 s and 1000 km at 250 s) is a first proxy for the resolution capabilities of the method. However, the final model resolution depends on the number of crossing paths of the two-station measurements, their quality, the measured period range and the different depth sensitivities of Rayleigh and Love waves.

- **Can we gain information on the radial anisotropic structure of the upper mantle from using Love and Rayleigh waves?**
  It is well known that the Earth is radially anisotropic in the upper mantle (Dziewonski and Anderson, 1981). This kind of anisotropy is often related to the direction of material flow (horizontal vs. vertical) in the lithosphere and asthenosphere (e.g., Schaefer et al., 2011). The fact that Rayleigh waves are mostly sensitive to v_{SV} (vertically polarized shear velocity) and Love waves to v_{SH} (horizontally) can be used to study radial anisotropy (Muyzert and Snieder, 2000). Differences in measurement errors and resolution capability of Rayleigh and Love waves can, however, result in apparent anisotropy. Interpretations have thus to be made with caution.

2 Two-Receiver Measurements of Phase Velocity: Cross-Validation of Ambient-Noise and Earthquake-Based Observations

Published in Geophysical Journal International 207.3 (2016).

This article comprises three major parts of the presented thesis:

1. Theoretical derivations of the ambient-noise method, starting from a simple 2-D expression of a surface wave. Two different approaches are followed that show how by cross-correlation and stacking over a long time period, surface-wave phase-velocities between arbitrary station pairs can be determined. It is shown that the two approaches will lead to the same result when the vertical (Z) component of Rayleigh waves is used. However, there is a difference for horizontal (R,T) components of Love and Rayleigh waves. This has not been shown before in direct comparison and can be explained by the high-frequency approximation applied in the stationary-phase approach. This result is important to understand possible measurement errors when horizontal components are used.

2. An automated scheme for the extraction of phase-velocity measurements, based on a program by Cornelis Weemstra (unpublished) and the original ideas of Aki (1957) and Ekström et al. (2009), is presented. It is implemented in a Python script and is used to evaluate the ambient-noise measurements in central Europe that are the basis of this PhD thesis.

3. A detailed comparison between ambient-noise and earthquake-based recordings is given. Both methods are used to obtain inter-station phase-velocity measurements, but based on different signal sources. Ideally, the results should be identical, however, in the article it is shown that there exists a small bias between the methods. This bias is discussed in detail and possible sources of error

for the ambient-noise method are tested for with synthetic tests. Finally, the influence of this bias is tested in an application example by comparison of two phase-velocity maps of Europe.

Geophysical Journal International

Geophys. J. Int. (2016) **207,** 1493–1512
Advance Access publication 2016 September 20
GJI Seismology

doi: 10.1093/gji/ggw341

Two-receiver measurements of phase velocity: cross-validation of ambient-noise and earthquake-based observations

Emanuel D. Kästle,[1] Riaz Soomro,[2] Cornelis Weemstra,[3] Lapo Boschi[1] and Thomas Meier[2]

[1] *Laboratoire iSTeP, Université Pierre et Marie Curie, Paris, France. E-mail: emanuel.kaestle@etu.upmc.fr*
[2] *Institute of Geosciences, Kiel, SH, Germany*
[3] *Department of Geoscience and Engineering, Delft University of Technology, Delft, The Netherlands*

Accepted 2016 September 19. Received 2016 July 25; in original form 2015 December 15

SUMMARY

Phase velocities derived from ambient-noise cross-correlation are compared with phase velocities calculated from cross-correlations of waveform recordings of teleseismic earthquakes whose epicentres are approximately on the station–station great circle. The comparison is conducted both for Rayleigh and Love waves using over 1000 station pairs in central Europe. We describe in detail our signal-processing method which allows for automated processing of large amounts of data. Ambient-noise data are collected in the 5–80 s period range, whereas teleseismic data are available between about 8 and 250 s, resulting in a broad common period range between 8 and 80 s. At intermediate periods around 30 s and for shorter interstation distances, phase velocities measured from ambient noise are on average between 0.5 per cent and 1.5 per cent lower than those observed via the earthquake-based method. This discrepancy is small compared to typical phase-velocity heterogeneities (10 per cent peak-to-peak or more) observed in this period range.We nevertheless conduct a suite of synthetic tests to evaluate whether known biases in ambient-noise cross-correlation measurements could account for this discrepancy; we specifically evaluate the effects of heterogeneities in source distribution, of azimuthal anisotropy in surface-wave velocity and of the presence of near-field, rather than far-field only, sources of seismic noise. We find that these effects can be quite important comparing individual station pairs. The systematic discrepancy is presumably due to a combination of factors, related to differences in sensitivity of earthquake versus noise data to lateral heterogeneity. The data sets from both methods are used to create some preliminary tomographic maps that are characterized by velocity heterogeneities of similar amplitude and pattern, confirming the overall agreement between the two measurement methods.

Key words: Numerical approximations and analysis; Tomography; Interferometry; Surface waves and free oscillations; Wave propagation.

1 INTRODUCTION

It has been observed that an important contribution to what is classically considered as noise in a seismogram comes from signals that arise from the oceans' coupling with the solid Earth. These signals are generally referred to as microseisms and their generation has first been explained by Longuet-Higgins (1950) and Hasselmann (1963). Their dependence on the ocean activity is reflected by a seasonal variability of the recorded noise intensity (Stehly *et al.* 2006; Hillers *et al.* 2012). Friedrich *et al.* (1998) show that the noise wavefield is dominated by surface waves, with ratios between Love and Rayleigh waves changing with frequency. The wavefield associated with the microseisms is significantly less coherent than the one excited by earthquakes (e.g. Pedersen & Krüger 2007), and its intensity much lower. By means of seismic interferometry, however, the approximate diffusivity of the noise wavefield can be exploited: given sufficiently long recordings of ambient seismic noise at two locations, group and phase velocity between these two locations can be extracted (Boschi & Weemstra 2015, and citations therein).

Microseisms are most energetic in the period band between 5 and 30 s. At the shorter period end of this range, surface waves from teleseismic earthquakes are difficult to observe. Local to regional seismicity is needed to obtain phase velocities from earthquake data in the frequency range between about 3 and 10 s (Endrun *et al.* 2004). Ambient noise can therefore provide information complementary to that obtained from earthquake-based studies (e.g. Meier *et al.* 2004; Lebedev *et al.* 2009; Yoshizawa & Ekström 2010; Endrun *et al.* 2011;

Agius & Lebedev 2013). Because the frequency of a surface wave controls the depth range over which particle motion is excited, high-frequency signals contain information on the shallow part of the earth (e.g. Udías 1999), making ambient-noise studies ideal to assess the structure of the crust and upper mantle. Recordings of earthquake-generated teleseismic surface waves are dominated by lower-frequency signal and thus sensitive to larger depths; their combination with ambient-noise data results in a data set that is sensitive to a broader depth range than ever previously achieved (Yao *et al.* 2006, 2008; Ritzwoller *et al.* 2011; Köhler *et al.* 2012; Zhou *et al.* 2012). We only treat surface-wave phase velocity in this work, which has the advantage that group velocity can be derived from it, while the opposite is not possible. Furthermore, phase velocities are to be preferred in tomographic inversions (e.g. Zhou *et al.* 2006).

Phase-velocity measurements made from ambient noise are only valid under certain conditions such as a uniform distribution of noise sources in space and time, a laterally homogeneous medium velocity, and far-field sources. As these conditions are not strictly met in practical situations, errors in the measured phase velocity are to be expected. These errors have been quantified for certain situations analytically and by synthetic models (Tsai 2009; Weaver *et al.* 2009; Yao & Van Der Hilst 2009; Tsai & Moschetti 2010; Tsai 2011). It is, however, not always possible to correct for them due to the complexity of these effects. It is therefore important to validate data obtained from ambient-noise analysis by comparison with equivalent measurements obtained from earthquake observations by classical methods. We focus here on ambient-noise reconstruction of Rayleigh- and Love-wave dispersion in Europe, comparing our observations with the two-station, earthquake-based dispersion database of Soomro *et al.* (2016).

A similar approach was followed before by Harmon *et al.* (2008), Yang *et al.* (2008a,b), Yao *et al.* (2008), Ritzwoller *et al.* (2011), Köhler *et al.* (2012), Zhou *et al.* (2012) and Shen *et al.* (2013). Yao *et al.* (2008) present a direct comparison of phase-velocity dispersion curves. The other authors compare mapped phase-velocity differences for specific regions. In all cases where differences have been analysed in detail, it is evident that velocities measured from ambient noise tend to be slightly lower, with reported differences between 0.07 and 0.001 km s^{-1}. This indicates that there might be a systematic effect which influences one or both of the methods.

The first objective of this work is to present the automated processing of ambient-noise data in the frequency domain. Our algorithm is based on the ideas of Aki (1957) and Ekström *et al.* (2009); it is essentially an improved version of the 'frequency domain' method employed by Boschi *et al.* (2013) and Korostelev *et al.* (2015), who did not describe in detail the underlying theory. In this approach, the zero crossings of the real part of the cross-correlation spectrum are evaluated to derive the phase-velocity dispersion. Importantly, this means that the Green's function's amplitude does not have to be reconstructed, which is the case when phase is to be determined by analysis of time-domain traces (Bensen *et al.* 2007; Lin *et al.* 2008; Zhou *et al.* 2012; Verbeke *et al.* 2012). We verify that our algorithm can successfully measure the phase velocity of both Love and Rayleigh waves from ambient noise. Ekström (2014), among others, already showed that Love-wave phase velocity can be determined from ambient noise. However, his data set was constructed in the assumption that wave polarization does not affect the data analysis procedure. We verify via synthetic tests that this approximation is acceptable at most periods and explain how to correct for it when taking measures at long periods.

The second objective is to validate ambient-noise observations by comparison with earthquake-based ones. We select central Europe as our study region to exploit the good station coverage found alone and around the Alpine chain. We compare the noise- and earthquake-based data at the same station couples in order to estimate the discrepancy in phase velocity from ambient-noise and earthquake records. The residuals are compared to known effects from noise theory and tested against synthetic experiments. By doing so, we prove the validity of results obtained from ambient noise and justify combining the two data sets in joint phase-velocity mapping.

2 AMBIENT-NOISE THEORY

2.1 Vertical component (Rayleigh waves)

Let us consider a Rayleigh wave in the frequency domain. The displacement is given, for example, by Aki & Richards (2002), eq. (7.144). For now, we are only interested in the displacement along the z-component (perpendicular to the surface) and ignore all higher modes, assuming that the ambient-surface wavefield is dominated by the fundamental mode (Halliday & Curtis 2008). Source and receiver are assumed to be at the surface so that the depth dependent eigenfunctions can be ignored. The amplitude is normalized according to Snieder (1986, 2004). With these simplifications the vertical displacement can be expressed as

$$U_1(\omega) = \underbrace{A(\omega)e^{i\phi(\omega)}}_{\text{source}} \underbrace{\sqrt{\frac{2c(\omega)}{\pi\omega r_1}}e^{i\left(\frac{\omega r_1}{c(\omega)}+\frac{\pi}{4}\right)}}_{2-\text{D Green's function}}, \tag{1}$$

where $A(\omega)$ and $\phi(\omega)$ are the source's amplitude and phase spectra, i is the imaginary unit, ω the angular frequency, $c(\omega)$ the dispersive phase velocity and r_1 is the distance travelled from the source to receiver 1. The expression for the Green's function is analogous to eq. (14) in Snieder (2004) and eq. (E17) in Boschi & Weemstra (2015), except that we prefer here to employ the notation of Aki & Richards (2002). The same wave recorded at a second station will have a slightly different phase and amplitude, according to the difference in distance travelled

$$U_2(\omega) = A(\omega)e^{i\phi(\omega)}\sqrt{\frac{2c(\omega)}{\pi\omega r_2}}e^{i\left(\frac{\omega r_2}{c(\omega)}+\frac{\pi}{4}\right)}. \tag{2}$$

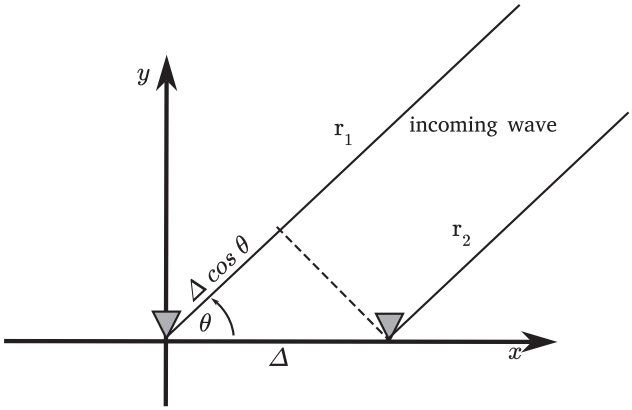

Figure 1. Incoming plane wave at an angle of θ. The distance between the stations depicted as grey triangles is denoted by Δ and the difference in source–station path therefore coincides with $\Delta \cos\theta$.

The cross-correlation of the displacement at two stations located at r_1 and r_2, caused by a single source, is given, in the frequency domain, by multiplication with the complex conjugate (denoted by the superscript $*$)

$$U_1(\omega)U_2^*(\omega) = A^2(\omega)\frac{2c(\omega)}{\pi\omega}\frac{1}{\sqrt{r_1 r_2}}e^{i\left(\frac{\omega r_1}{c(\omega)}+\frac{\pi}{4}+\phi(\omega)\right)}e^{-i\left(\frac{\omega r_2}{c(\omega)}+\frac{\pi}{4}+\phi(\omega)\right)} = A^2(\omega)\frac{2c(\omega)}{\pi\omega}\frac{1}{\sqrt{r_1 r_2}}e^{i\frac{\omega}{c(\omega)}(r_1-r_2)}. \tag{3}$$

For sources distributed along a circle of large radius R, measured from the centre of the coordinate system in Fig. 1, the expressions $r_1 r_2$ and $r_1 - r_2$ can be approximated according to Fig. 1,

$$r_1 - r_2 \approx \Delta\cos\theta$$

$$r_1 r_2 \approx R(R - \Delta\cos\theta) = R^2\left(1 - \frac{\Delta\cos\theta}{R}\right) \approx R^2, \tag{4}$$

where Δ is the distance between the stations and θ is the angle towards the source. Strictly speaking, the above formula is only valid if sources are infinitely far away from the receivers, that is, for plane waves. The error introduced from this simplification will be discussed below with the help of synthetic tests. We now sum the cross-correlation for a large number of sources which we assume to correspond, approximately, to measuring the two-receiver cross-correlation over a long time period. Substituting the expressions from eq. (4) in eq. (3) and summing over N sources gives

$$C(\omega) \approx \frac{2c(\omega)}{\pi\omega}\lim_{N\to\infty}\frac{1}{N}\left(\sum_j^N \frac{A_j^2(\omega)}{R}e^{i\frac{\omega}{c(\omega)}\Delta\cos\theta_j}\right) = \frac{2c(\omega)}{\pi\omega R}\frac{1}{2\pi}\int_{-\pi}^{\pi} A^2(\omega,\theta)e^{i\frac{\omega\Delta}{c(\omega)}\cos\theta}\,\mathrm{d}\theta. \tag{5}$$

$C(\omega)$ is the stacked cross-correlation resulting from an infinitely dense source distribution. Eq. (5) differs from its pure plane-wave counterpart in that the geometrical spreading term $1/R$ is kept. We expressed the sum as an integral over all azimuths, where $A^2(\omega,\theta)$ is now an amplitude density depending on the azimuth θ of the incoming wave. Note that A^2 includes an implicit normalization dependent on the density of the discrete sources (i.e. it includes a constant with units rad^{-1}), which ensures that the evaluation of the integral and the result of the summation give equal values and have equal units.

In case of simultaneously acting sources, constructive interference of signal coming from different sources gives rise to spurious travel-time delays. These spurious peaks in the cross-correlation are generally referred to as 'cross-terms' (e.g. Weemstra *et al.* 2015). Assuming the behaviour of different sources is uncorrelated, however, stacking over time renders these cross-terms negligible. Consequently, even if some of the N sources in eq. (5) act simultaneously, the time-averaged cross-correlation will still coincide with the right-hand side of eq. (5). Summing cross-correlations over time is what is generally implemented in practice (e.g. Bensen *et al.* 2007).

2.1.1 Exact integration

We assume that the amplitude term in eq. (5) is independent of θ, that is, there are sources with equal intensity everywhere around the receivers. It then follows that

$$C(\omega) \approx \frac{2c(\omega)}{\pi\omega R}\frac{1}{2\pi}\int_{-\pi}^{\pi} A^2(\omega,\theta)e^{i\frac{\omega\Delta}{c}\cos\theta}\,\mathrm{d}\theta = \frac{2c}{\pi\omega R}\frac{1}{2\pi}A^2(\omega)\int_{-\pi}^{\pi} e^{i\frac{\omega\Delta}{c(\omega)}\cos\theta}\,\mathrm{d}\theta = \frac{2c(\omega)}{\pi\omega R}A^2(\omega)J_0\left(\frac{\omega\Delta}{c(\omega)}\right), \tag{6}$$

where the definition of the Bessel function of the first kind and order n from Abramowitz & Stegun (1964) (eq. 9.1.21) has been used:

$$J_n(z) = \frac{i^{-n}}{\pi}\int_0^{\pi} e^{iz\cos\theta}\cos(n\theta)\,\mathrm{d}\theta. \tag{7}$$

Eq. (6) is equivalent to eq. (72) in Boschi & Weemstra (2015). The important result from eq. (6) is that cross-correlating the noise wavefield at two locations of known separation Δ, gives an estimation of the phase velocity $c(\omega)$ between the stations (the detailed procedure is explained in the following sections). This relationship was first derived by Aki (1957) and is at the basis of the SPAC (spatial autocorrelation) method (Aki 1957; Bettig *et al.* 2001) for local arrays. The equivalence of temporal (as in this work) and spatial cross-correlation (as in the SPAC method) is discussed by Tsai & Moschetti (2010).

We obtained eq. (6) in the assumption that A is independent of the direction of propagation. For a strongly non-uniform illumination pattern, the deviations from a Bessel function can be quite large and the imaginary part will not vanish (Tsai 2009; Weaver *et al.* 2009; Yao & Van Der Hilst 2009; Basini *et al.* 2013). This can result in erroneous phase velocities. In most applications, however, this approximation is good enough. Examples using synthetic tests are shown below.

2.1.2 Stationary-phase integration

It is also possible to solve the integral in eq. (6) by a stationary-phase approximation (e.g. Snieder 2004; Boschi & Weemstra 2015). In this case, ω and/or Δ is assumed to be large, which means that $\exp(i(\omega\Delta\cos\theta/c))$ is a rapidly oscillating function of θ. A rapid oscillation around zero means equal positive and negative contributions to the integral over θ which will approximately cancel out. It is thus enough to evaluate the integral at the stationary points where the phase term $\psi(\theta) = \Delta\cos\theta/c$ is stationary, that is, $\mathrm{d}\psi(\theta)/\mathrm{d}\theta = 0$. This gives

$$I(\omega) = \int_{-\infty}^{\infty} f(\theta) e^{i\omega\psi(\theta)}\,\mathrm{d}\theta \approx f(a) e^{i\left(\omega\psi(a)\pm\frac{\pi}{4}\right)}\sqrt{\frac{2\pi}{\omega|\psi''(a)|}}, \tag{8}$$

for a single stationary point at a, valid for $\omega\to\infty$ and assuming that the second derivative ψ'' with respect to θ is not zero at $\theta = a$ (e.g. Bender & Orszag 1978). The sign of $\pi/4$ in the exponent is positive for $\psi''(a) \geq 0$ and negative otherwise. If we have a definite integral and the stationary point is at one of the integration limits, a factor of $\frac{1}{2}$ has to be included. In eq. (6), there are three stationary points at

$$\frac{\mathrm{d}}{\mathrm{d}\theta}\frac{\Delta\,\cos\theta}{c(\omega)} = -\frac{\Delta\,\sin\theta}{c(\omega)} = 0, \quad \texttt{for} \quad \theta = -\pi, 0, \pi, \tag{9}$$

with two of the stationary points at the integration limits. We can thus solve the integral in eq. (6),

$$C(\omega) \approx \frac{2c(\omega)}{\pi\omega R}\frac{1}{2\pi}\int_{-\pi}^{\pi} A^2(\omega,\theta) e^{i\frac{\omega\Delta}{c(\omega)}\cos\theta}\,\mathrm{d}\theta \approx \frac{c(\omega)}{\pi^2\omega R}\left[\frac{1}{2}A^2(\omega,-\pi)\sqrt{\frac{2\pi}{\frac{\omega\Delta}{c(\omega)}}}e^{-i\left(\frac{\omega\Delta}{c(\omega)}-\frac{\pi}{4}\right)}\right.$$
$$\left. + A^2(\omega,0)\sqrt{\frac{2\pi}{\frac{\omega\Delta}{c(\omega)}}}e^{i\left(\frac{\omega\Delta}{c(\omega)}-\frac{\pi}{4}\right)} + \frac{1}{2}A^2(\omega,\pi)\sqrt{\frac{2\pi}{\frac{\omega\Delta}{c(\omega)}}}e^{-i\left(\frac{\omega\Delta}{c(\omega)}-\frac{\pi}{4}\right)}\right]. \tag{10}$$

Since $A(\omega,-\pi) = A(\omega,\pi)$, we can write

$$C(\omega) \approx \frac{c(\omega)}{\pi^2\omega R}\left[A^2(\omega,0)\sqrt{\frac{2\pi}{\frac{\omega\Delta}{c(\omega)}}}e^{i\left(\frac{\omega\Delta}{c(\omega)}-\frac{\pi}{4}\right)} + A^2(\omega,\pi)\sqrt{\frac{2\pi}{\frac{\omega\Delta}{c(\omega)}}}e^{-i\left(\frac{\omega\Delta}{c(\omega)}-\frac{\pi}{4}\right)}\right]. \tag{11}$$

The terms $\exp(\pm i(\frac{\omega\Delta}{c(\omega)} - \frac{\pi}{4}))$ describe a wave travelling from receiver 1 to receiver 2 and vice versa, which are often referred to as causal and anti-causal parts of the cross-correlation.

Eq. (11) shows that the contributions to the cross-correlation associated with sources at $\theta = 0$ and $\theta = \pi$ have phases of $\omega\Delta/c - \pi/4$ and $\omega\Delta/c + \pi/4$, respectively. This $\pi/4$ phase shift was something being thought of as a 'discrepancy' between causal/acausal terms and the phase of an impulse travelling with speed c between the locations. Due to the fact that we are dealing with a circular source distribution, the solution is characterized by a Bessel function (eq. 6). In the high-frequency and/or long interstation distance limit, the Bessel function is approximated by a cosine with $\pi/4$ phase shift (Fig. 2). This explains the stationary-phase solution in eq. (11). Most time-domain approaches use this approximation and consequently it is important to apply the $\pi/4$ correction. However, this introduces an error at low frequencies and/or short interstation distance (Tsai 2009; Boschi *et al.* 2013). The frequency-domain algorithm presented here does not require such correction as we determine phase velocities using directly the properties of the Bessel function.

The source intensity A in eq. (11) is allowed to be a smoothly varying function of θ. We can see that the forward and backward terms are scaled by the amplitude term in 0- and π-direction, that is, aligned with the station pair (Fig. 1). This means that in the infinite frequency limit, only sources on the x-axis contribute constructively. For lower frequencies, the Fresnel zone is characterized by two hyperbolae aligned with the x-axis (e.g. Snieder 2004). The azimuths where noise sources contribute constructively can be expressed in an approximate formula from Yao & Van Der Hilst (2009)

$$|\Delta\cos(\theta) - \Delta| < \frac{c(\omega)}{2\omega}, \tag{12}$$

referring to the definition of Δ and θ from Fig. 1.

Note that in the stationary-phase approach, eq. (11) can be derived as well without the plane wave approximations from eq. (4) (Boschi & Weemstra 2015).

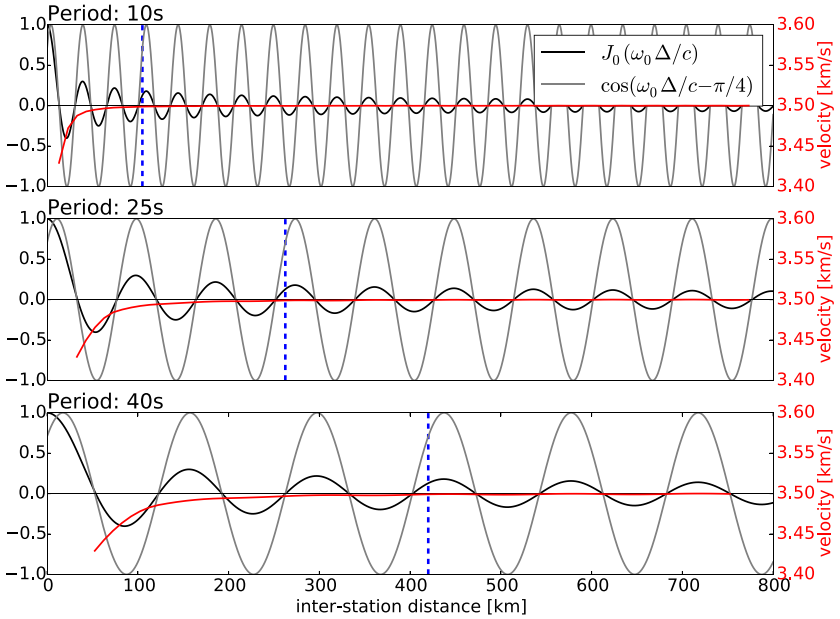

Figure 2. Bessel function (black line) compared to its high-frequency/long interstation distance approximation (grey), which is often used in time domain approaches. Both curves are shown with respect to interstation distance and at three different periods. The velocity c is set to 3.5 km s^{-1} for both curves. In time domain approaches, the phase velocity is determined by evaluating the phase of the stacked cross-correlation spectrum and correcting it by $\pi/4$. This introduces an error at long periods and short interstation distances, plotted here as red curve. Accordingly, data associated with short (typically less than three wavelengths, blue dashed line) interstation distance are often discarded (e.g. Bensen *et al.* 2007).

Using $i = \exp(i\pi/2)$, eq. (11) can be rewritten as

$$C(\omega) \approx \frac{c(\omega)}{i\pi\omega R}\left(A^2(\omega,0)\sqrt{\frac{2c(\omega)}{\pi\omega\Delta}}e^{i\left(\frac{\omega\Delta}{c(\omega)}+\frac{\pi}{4}\right)} - A^2(\omega,\pi)\sqrt{\frac{2c(\omega)}{\pi\omega\Delta}}e^{-i\left(\frac{\omega\Delta}{c(\omega)}+\frac{\pi}{4}\right)}\right), \tag{13}$$

which contains the far-field approximation of the Hankel function (eq. C4-5 in Boschi & Weemstra 2015), yielding

$$C(\omega) \approx \frac{c(\omega)}{\pi\omega R}\left[A^2(\omega,0)\left(J_0\left(\frac{\omega\Delta}{c(\omega)}\right)+iY_0\left(\frac{\omega\Delta}{c(\omega)}\right)\right)+A^2(\omega,\pi)\left(J_0\left(\frac{\omega\Delta}{c(\omega)}\right)-iY_0\left(\frac{\omega\Delta}{c(\omega)}\right)\right)\right]. \tag{14}$$

If we assume as before, that $A(\omega,\theta)$ is equal for all directions we get

$$C(\omega) \approx \frac{2c(\omega)}{\pi\omega R}A^2(\omega)J_0\left(\frac{\omega\Delta}{c(\omega)}\right) \tag{15}$$

which is the same as eq. (6). It is clear from the above treatment that if $A(0) \neq A(\pi)$ the imaginary part of the cross-correlation spectrum does not vanish. From eq. (14), it may also look like that in this case the real part of the cross-correlation spectrum still follows a Bessel function. However, this is strictly speaking only true in the high frequency limit, for which the stationary-phase result was derived.

2.2 Horizontal components (Rayleigh and Love waves)

When applying this method to Love waves, we are interested in the horizontal displacement, perpendicular to the great-circle identified by the receiver locations (y-axis in Fig. 1). With the same assumptions as for eq. (1), eq. (7.143) from Aki & Richards (2002) can be simplified as

$$U_{1L}(\omega) = A_L(\omega)\sqrt{\frac{2c_L(\omega)}{\pi\omega r_1}}e^{i\left(\frac{\omega r_1}{c_L(\omega)}+\frac{\pi}{4}+\phi(\omega)\right)}\cos(\theta), \tag{16}$$

which is the same as eq. (1), apart from the $\cos(\theta)$ term, where θ is the angle from station 1 towards the source (Fig. 1). Hence, the $\cos(\theta)$ term assures that, for Love waves and the geometry in Fig. 1, we are only looking at the y-component of the displacement. The radial (parallel to the receiver-receiver great circle) Rayleigh-wave displacement has the same expression, with A_R and c_R replacing A_L and c_L, respectively. With the same far-field assumptions as above (meaning also that θ is equal for both stations), the cross-correlation of horizontal surface-wave displacement at the two stations reads

$$C_h(\omega) \approx \frac{2c(\omega)}{\pi\omega R}A^2(\omega)\frac{1}{2\pi}\int_{-\pi}^{\pi}e^{i\frac{\omega\Delta}{c(\omega)}\cos\theta}\cos^2(\theta)\,\mathrm{d}\theta, \tag{17}$$

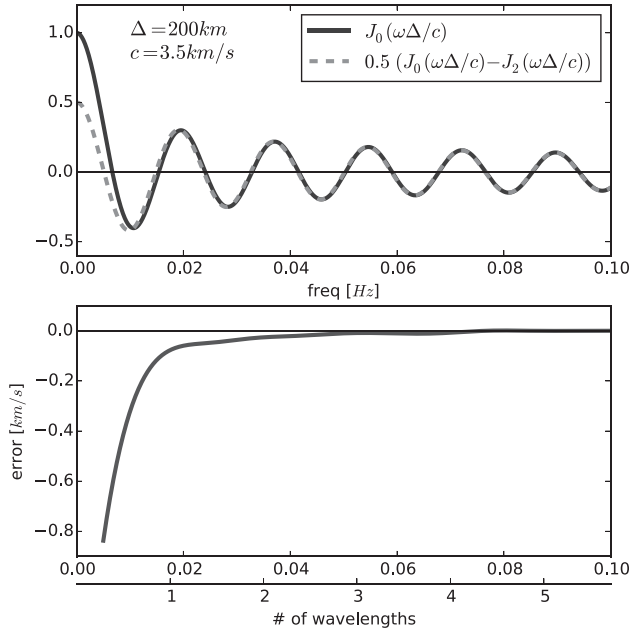

Figure 3. Top panel: zero-order Bessel function J_0 of $\frac{\omega\Delta}{c}$, and difference between J_0 and the second-order Bessel function J_2 of the same argument. These functions control the vertical- and horizontal-component cross-correlations according to eqs (15) and (19), respectively, for the particular case of constant $c = 3.5$ km s^{-1} (no dispersion). In the literature, the contribution of J_2 to the horizontal component is sometimes neglected, resulting in an error that can be significant at low frequencies and/or short interstation distances. We quantify this error by applying our measurement algorithm on the cross-correlations of the top panel, and plotting (bottom panel) the difference between the resulting dispersion curves. The secondary x-axis of the bottom plot shows the number of wavelengths that correspond to an interstation distance of 200 km and a phase velocity of 3.5 km s^{-1} at the respective frequency.

where A and c have to be adapted for Rayleigh and Love waves, accordingly. Eq. (17) can be seen as the radial- and transverse counterpart of eq. (6). Making use of the trigonometric identity for $\cos^2(\theta) = (\cos(2\theta) + 1)/2$ and rearranging yields

$$C_h(\omega) \approx \frac{2c(\omega)}{\pi\omega R}A^2(\omega)\frac{1}{2\pi}\int_{-\pi}^{\pi} e^{i\frac{\omega\Delta}{c(\omega)}\cos\theta}\frac{1+\cos(2\theta)}{2}\,\mathrm{d}\theta$$
$$= \frac{c(\omega)}{\pi\omega R}A^2(\omega)\frac{1}{2\pi}\left[\int_{-\pi}^{\pi} e^{i\frac{\omega\Delta}{c(\omega)}\cos\theta}\,\mathrm{d}\theta + \int_{-\pi}^{\pi} e^{i\frac{\omega\Delta}{c(\omega)}\cos\theta}\cos(2\theta)\,\mathrm{d}\theta\right]. \tag{18}$$

After substituting eq. (7) into eq. (18), the latter equation takes the simpler form

$$C_h(\omega) \approx \frac{c(\omega)}{\pi\omega R}A^2(\omega)\left[J_0\left(\frac{\omega\Delta}{c(\omega)}\right) - J_2\left(\frac{\omega\Delta}{c(\omega)}\right)\right]. \tag{19}$$

This result is also given by Aki (1957) and Sánchez-Sesma & Campillo (2006).

Alternatively, the integral in eq. (17) can be solved via the stationary-phase approximation, since $cos^2(\theta)$ is smooth relative to the rapid oscillation of the phase term for high ω. This gives for the three stationary points at $-\pi$, 0 and π

$$C_h(\omega) \approx \frac{2c(\omega)}{\pi\omega R}\frac{1}{2\pi}\int_{-\pi}^{\pi} A^2(\omega,\theta)e^{i\frac{\omega\Delta}{c(\omega)}\cos\theta}\cos^2(\theta)\,\mathrm{d}\theta \approx \frac{c(\omega)}{\pi^2\omega R}\left[\frac{1}{2}A^2(\omega,-\pi)\cos^2(-\pi)\sqrt{\frac{2\pi}{\frac{\omega\Delta}{c(\omega)}}}e^{-i\left(\frac{\omega\Delta}{c(\omega)}-\frac{\pi}{4}\right)}\right.$$
$$\left. + A^2(\omega,0)\cos^2(0)\sqrt{\frac{2\pi}{\frac{\omega\Delta}{c(\omega)}}}e^{i\left(\frac{\omega\Delta}{c(\omega)}-\frac{\pi}{4}\right)} + \frac{1}{2}A^2(\omega,\pi)\cos^2(\pi)\sqrt{\frac{2\pi}{\frac{\omega\Delta}{c(\omega)}}}e^{-i\left(\frac{\omega\Delta}{c(\omega)}-\frac{\pi}{4}\right)}\right]$$
$$= \frac{2c(\omega)}{\pi\omega R}A^2(\omega)J_0\left(\frac{\omega\Delta}{c(\omega)}\right), \tag{20}$$

if we assume, as above, that $A(0) = A(\pi)$. The right-hand side of eq. (20) coincides with that of eq. (15) (e.g. Snieder 2004) and differs from the exact integration in eq. (19). This is consistent with the high frequency behaviour of eq. (19), which we have verified numerically as shown in Fig. 3, that is,

$$\lim_{\omega\to\infty}\frac{1}{2}\left[J_0\left(\frac{\omega\Delta}{c(\omega)}\right) - J_2\left(\frac{\omega\Delta}{c(\omega)}\right)\right] = J_0\left(\frac{\omega\Delta}{c(\omega)}\right). \tag{21}$$

Estimating phase velocities of Love waves or the horizontal component of Rayleigh waves with a simple Bessel function will therefore introduce an error, but only at low frequencies. An example of this effect is shown in Fig. 3. Most researchers do not apply the ambient-noise method (ANM) at periods longer than 30 s (0.033 Hz), where the discrepancy shown in Fig. 3 is lower than 0.03 km s^{-1} (0.9 per cent) for an

interstation distance of 200 km. With increasing interstation distance Δ this effect reduces further. Discarding all data where the interstation distance is shorter than three wavelengths (e.g. Bensen *et al.* 2007) reduces the error to 0.25 per cent over all frequencies. Consequently, this issue is often ignored when extracting Love waves (e.g. Lin *et al.* 2008; Ekström 2014). However, Fig. 3 shows that at low frequencies the error can be as large as 10–20 per cent, which corresponds to typically mapped peak-to-peak phase-velocity differences in the earth (e.g. Verbeke *et al.* 2012; Ekström 2014; Soomro *et al.* 2016). As we aim to exploit all available data and extend the limits of the method to lower frequencies, we include this modification in the presented procedure.

2.3 Pre-processing and correlation

Our algorithm measures the phase-velocity curve for a given station couple by cross-correlation and stacking of noise records. It is applied to pairs of sufficiently long seismograms, which ensures that signals from a relatively large number of sources at different azimuths are recorded. At regional/continental scale, it is preferable to work with one-year-long recordings, since the azimuth of noise propagation has been shown to change seasonally (e.g. Stehly *et al.* 2006; Yang & Ritzwoller 2008). For the same reason, the benefit of using more than one year of data with respect to one full year might be negligible. More detailed discussions on the time span of noise recordings can be found in Bensen *et al.* (2007) and Seats *et al.* (2012).

Records are filtered in the frequency band of interest (2–200s). First, this allows decimation (reduction of sample rate) for all seismograms where 1 Hz sampling rate data are not readily available, which saves disk space and speeds up processing. Second, it restricts the following restitution filtering to a valid frequency range. In our case, pre-processing includes removing the instrument response (restitution), to avoid that different phase responses of used seismometers change the phase-velocity measurement. However, broad-band instruments have often a zero phase shift over a large frequency range and our tests show accordingly that the effects from restitution are marginal.

Wherever gaps appear in the recordings we zero-pad the data in order to get continuous time series. The data is then cut into overlapping time windows (e.g. half an hour with 50 per cent overlap), cosine-tapered at both ends and Fourier transformed. The effects of different window lengths and overlaps are discussed by Seats *et al.* (2012). Spectral whitening (e.g. Bensen *et al.* 2007) equalizes all amplitudes, therefore broadening the spectrum, downweighting strong signals from earthquakes and reducing influence from monochromatic sources:

$$C_{\text{whitened}}(\omega) = \frac{U_1(\omega)U_2^*(\omega)}{|U_1(\omega)||U_2(\omega)|}. \tag{22}$$

There are also other approaches to achieve this (e.g. Bensen *et al.* 2007; Ekström *et al.* 2009); Ekström (2014), however, notes that effects of whitening or removal of earthquake signals have only very small influence on the phase-velocity measurement.

This procedure is applied to the Z- or R-component recordings for Rayleigh waves and T-component recordings for Love waves. The R direction is defined as parallel to the great circle connecting the station pair; T is perpendicular to both R and Z.

2.4 Phase-velocity determination

In the following, we discard the imaginary part of the stacked cross-correlation spectrum which should ideally be zero (eq. 14). Its real part is often characterized by strong high-frequency variability that causes additional, spurious zero crossings (Fig. 4). This can be overcome by a smoothing filter, in our case a simple low-pass filter. The corner frequency depends on the interstation distance and on estimated minimum phase velocity. In the next step, the zero crossings of the smoothed curve are identified and compared to the Bessel function.

Let us denote z_m ($m = 1, 2, \ldots, \infty$) the discrete set of values of the argument of J_0, such that $J_0(z_m) = 0$. Eq. (6) shows that the vertical-component ambient-noise cross-correlation coincides with the Bessel function $J_0(\omega\Delta/c(\omega))$. By estimating a realistic minimum value for the phase velocities $c(\omega)$, we can reduce z_m to a finite set, $m = 1, 2, \ldots, M$. Ekström *et al.* (2009) proposed to estimate the dispersion curve $c(\omega)$ from the observed ambient-noise cross-correlation, by simply identifying the values ω_n of ω for which the observed cross-correlation is zero. Each ω_n corresponds to a discrete frequency where the spectrum is zero.

$$\frac{\omega_n \Delta}{c(\omega_n)} = z_m, \tag{23}$$

from which we can derive all possible phase velocities as

$$c(\omega_n) = \frac{\omega_n \Delta}{z_m}, \tag{24}$$

giving M possible phase velocities corresponding to ω_n. This number of possible values can be reduced by one half by only taking into account the zero crossings where the derivative of the Bessel function has the same sign as that of the (real part of the) observed spectrum. The problem is further simplified by limiting the result to a range of realistic phase velocities for the region, which is especially helpful at long periods where only a few points to choose from remain. To measure Love-wave phase velocity, or to have an alternative estimate of Rayleigh wave phase velocity via the radial component, the zero crossings of $J_0(z) - J_2(z)$ have to be determined; recall, however, that at high frequencies those coincide approximately with the zero crossings of $J_0(z)$.

In Fig. 4(b), an example of the real part of a cross-correlation spectrum and its smoothed version are shown. For each of the zero crossings at the frequencies ω_n, all of the M resulting phase velocities are plotted in Fig. 4(c). The goal is now to implement an automated

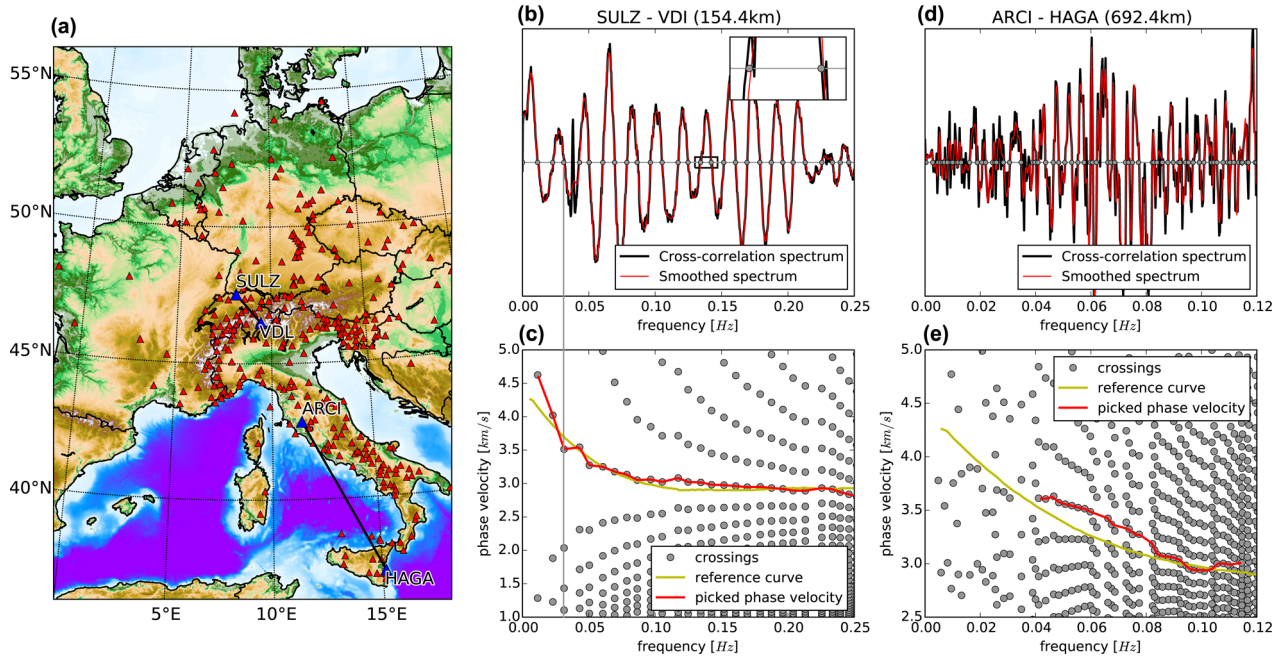

Figure 4. Processing of ambient-noise cross-correlation spectrum. (a) Station map. The selected stations for the examples are highlighted in blue. (b) Real part of the stacked cross-correlation spectrum for an approx. 1000 d record at SULZ and VDL before (black) and after (red) smoothing. A clear peak at 0.038 Hz is visible which does not fit the period of the rest of the spectrum. It is ignored by the smoothing as it would cause a velocity jump in the phase-velocity measurement. The inset zooms in on two zero crossings, where smoothing prevents additional zero crossings that are caused by unwanted noise in the spectrum. (c) Phase velocities from the spectrum's zero crossings. Each spectrum's zero crossing can be explained by several possible phase velocities as indicated by the grey line crossing between plots (b) and (c). The reference model is shown as yellow curve. The phase velocities are picked successively starting from the lowest frequencies. (d) Same as (b) for station couple ARCI and HAGA. The higher frequency of oscillation in the spectrum is due to the larger interstation distance. Only 200 d of correlation are available which causes a very noisy spectrum. (e) The low data quality makes phase-velocity picking difficult. Automated picks are only taken in a very limited frequency range [note the different scales of the frequency axis between (c) and (e)].

procedure that chooses the most realistic dispersion curve $c(\omega)$ by picking the right phase velocities. The least ambiguity is found at the low frequency end, where only few possible phase velocities fall within a realistic range. In order to choose the most likely value, the algorithm relies on a reference model (yellow curve in Fig. 4c). This model may come from a reference earth model, previous studies or by manual picking the dispersion curve for a couple of station pairs that represent a good average in the region of interest.

At the low frequency end, the automated picking relies only on this reference curve and will choose the phase velocities that are closest to it. After the first few values have been determined, more criteria are taken into account. Such criteria are defined based on the properties of Bessel functions:

(i) The frequency step $d\omega$ from one zero crossing to the next is approximately π, which becomes clear when one looks at the asymptotic approximation of the Bessel function by a cosine with $\pi/4$ phase shift. So when choosing the next phase-velocity value at frequency ω_{k+1}, it should be verified that

$$d\omega = \omega_{k+1} - \omega_k \approx \pi \frac{c(\omega_k)}{\Delta}, \tag{25}$$

assuming that $c(\omega_k)$ is not too different from $c(\omega_{k+1})$. This should be the case since surface-wave velocity implicitly averages, and thus smooths, Earth structure over depth. If the frequency step $d\omega$ is much smaller than the prediction, the spectrum is probably noisy, resulting in spurious zero crossings and therefore a jump to a higher phase velocity. Consequently, values of ω_n are ignored (up to an acceptable threshold) until a zero crossing is found whose frequency has an acceptable frequency-step width. On the other hand it can also happen that the spectrum does not have any zero crossing in a realistic range. This causes the algorithm to stop, because it is not possible to choose the next phase-velocity value without ambiguity.

(ii) In Fig. 4(c), several branches are visible that are sub-parallel to the red curve. The existence of these branches is linked to the ambiguity in m. The velocity jump from one branch to the next, that is, z_m to $z_{m\pm2}$ in eq. (24), is associated with 2π ($z_{m\pm1}$ has another crossing direction as z_m and can therefore be excluded). As phase velocities are supposed to vary smoothly, only picks that are at a certain threshold below 2π are considered.

Each picked phase-velocity value has to comply with the two above criteria. After a couple of points have been picked, a linear extrapolation over the last picks predicts the next possible value for the dispersion curve. Additional stabilizing criteria are a comparison of the gradient of the picked curve with the reference model, for example when steeply increasing phase velocities are picked while the model indicates rather decreasing values. The algorithm also tries to choose automatically where to start the picking of the phase-velocity curve,

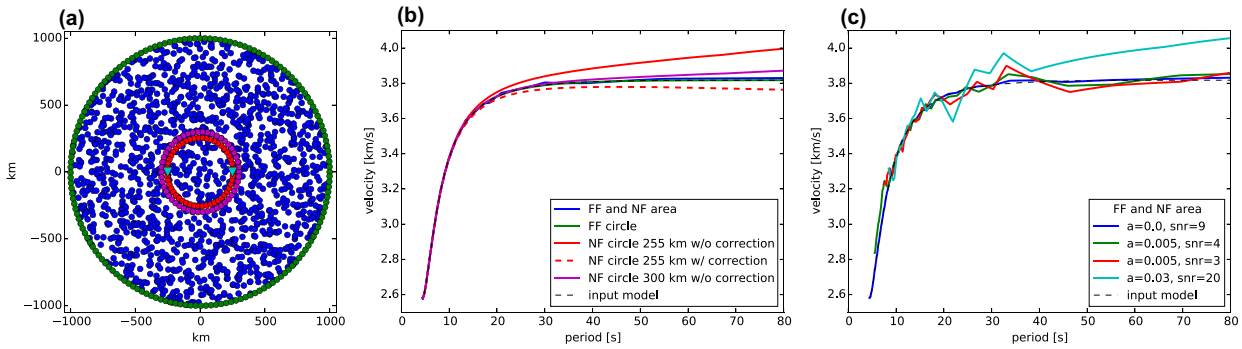

Figure 5. Phase-velocity estimation for four different scenarios of synthetic source distributions. (a) Map view of two stations at 500 km distance (triangles) and four example distributions of noise sources are shown. Blue circles: circular area of randomly distributed noise sources; green circles: sources in the far-field (FF); red circles: sources in the near field (NF), 255 km radius; magenta circles: sources in the near field, 300 km radius. (b) Respective phase-velocity estimations are shown in comparison with the dispersive input-velocity model. For explanation of the correction applied to the near-field sources, see the text. (c) Synthetic phase-velocities for the random source distribution in (a). *a* is the attenuation factor and snr is the signal-to-noise ratio.

when the cross-correlation spectrum is very noisy at low frequencies. For example, in Fig. 4(e), it only starts at 0.04 Hz and stops at 0.11 Hz, because the $d\omega$ criterion (i) has been violated too often.

3 SYNTHETIC TESTS OF SOURCE DISTRIBUTION EFFECTS

In this section, a station pair is placed in a simple medium with homogeneous velocity. Point sources are distributed in a number of ways around the station couple. Each source has a random amplitude and phase spectrum and the signal at the station is calculated by convolution with the 2-D Green's function (e.g. Boschi & Weemstra 2015, E15). The synthetic signals are cross-correlated for each source and the cross-correlation spectrum is stacked. No additional random error is applied to the data. The synthetic data are cross-correlated and evaluated in the same way as the real data, as explained in the previous section, in order to obtain a phase-velocity curve.

3.1 Far-/near-field sources

In Fig. 5, we compare the effects of far- and near-field source distributions. We use a dispersive phase-velocity distribution as 'input model'. We first assume a far-field source distribution covering all azimuths (green circles in Fig. 5a), reproducing the idealized setup assumed in the analytical derivation of Section 2. A source-receiver distance of 1000 km corresponds to 3.3 wavelengths at a period of 80 s and velocity of 3.8 km s^{-1}, which is large enough to meet the far-field criteria and indeed, the dispersion curve is perfectly recovered as shown in Fig. 5(b). In this setup, the maximum azimuth difference for a given source amounts to 28°.

In a second test, we assume again a circular source distribution, but with the circle lying in the near field of the receivers (red circles in Fig. 5a). The resulting discrepancy between input and output dispersion curves, illustrated in Fig. 5(b), can be explained in terms of the approximations made in the derivation of Section 2.1, which can be summarized as follows:

(i) to simplify our forward calculations, we have made use of a far-field approximation of the Green's function (eq. 1);
(ii) eq. (4) is valid for far-field sources (plane waves) only;
(iii) the stationary phase approximation in eq. (11) is valid only for high frequencies and/or large interstation distance Δ.

Point (iii) is not relevant to the rest of this study because our algorithm does not rely on the stationary-phase solution but uses the solution of the exact integration, that is, a Bessel function (eq. 6 or 15). The problem arising from (ii) is associated with the fact that in the near field the distance difference from source to station 1 and source to station 2 is generally smaller than what the far-field approximation requires (eq. 4). It is possible to correct for this effect by taking the exact definition of $r_1 - r_2$ which invokes, however, an estimation of the average distance R of sources providing the main contribution to observations. It is thus necessary to repeat the derivation that lead to eq. (5) without the far-field approximations from eq. (4). Again, we assume a circular source distribution, but with sources at a relatively small radius R. We find,

$$C(\omega) = \frac{2c(\omega)}{\pi\omega}\frac{1}{2\pi}\int_{-\pi}^{\pi}\frac{A^2(\omega,\theta)}{\sqrt{r_1(\theta)r_2(\theta)}}e^{i\frac{\omega}{c(\omega)}(r_1(\theta)-r_2(\theta))}\,\mathrm{d}\theta. \tag{26}$$

According to Fig. 1, we can write

$$r_1(\theta) - r_2(\theta) = R - \left[(R\cos\theta-\Delta)^2 + (R\sin\theta)^2\right]^{1/2} = R - \left[\Delta^2 - 2\Delta R\cos\theta + R^2\right]^{1/2},$$
$$r_1(\theta)r_2(\theta) = R\left[(R\cos\theta-\Delta)^2 + (R\sin\theta)^2\right]^{1/2} = R\left[\Delta^2 - 2\Delta R\cos\theta + R^2\right]^{1/2}, \tag{27}$$

which we substitute into eq. (26):

$$C(\omega) = \frac{2c(\omega)}{\pi\omega}\frac{1}{2\pi}\int_{-\pi}^{\pi}\frac{A^2(\omega,\theta)}{\sqrt{R\left[\Delta^2 - 2\Delta R\cos\theta + R^2\right]^{1/2}}}e^{i\frac{\omega}{c(\omega)}\left(R-\left[\Delta^2-2\Delta R\cos\theta+R^2\right]^{1/2}\right)}\,\mathrm{d}\theta. \tag{28}$$

We now define another function $f(x)$ which is independent of $c(\omega)$,

$$f(x) = \frac{2}{\pi\omega}\frac{1}{2\pi}\int_{-\pi}^{\pi}\frac{A^2(\omega,\theta)}{\sqrt{R\left[\Delta^2 - 2\Delta R\cos\theta + R^2\right]^{1/2}}}e^{i\omega\left(R-\left[\Delta^2-2\Delta R\cos\theta+R^2\right]^{1/2}\right)}\,\mathrm{d}\theta. \tag{29}$$

For a given station couple with interstation distance Δ, making a reasonable guess for R and assuming an idealized source distribution $A(\omega, \theta)$, which is 1 for all θ, we can integrate the right hand side of eq. (29) numerically. We can then extract (also numerically) the zero crossings z_m of $f(x)$. The following procedure is the same as described in Section 2.4. Each zero-crossing of the data-derived spectrum $C(\omega)$ is compared to the zero crossings of the near-field corrected function $f(x)$. All possible phase velocities $c_m(\omega_0)$ for a zero crossings in $C(\omega)$ at ω_0 are given by

$$c(\omega_0) = \frac{\omega_0}{z_m}. \tag{30}$$

This is the same as eq. (24), but without Δ, which we already took into account when we integrated eq. (29) numerically.

If the signal is whitened prior to cross-correlation (eq. 22) and if sources are not acting simultaneously, the $\frac{A^2(\omega,\theta)}{\sqrt{r_1(\theta)r_2(\theta)}}$ term in eq. (26) cancels out. This has to be taken into account when integrating eq. (29). This approach results in the dashed red line of Fig. 5.

An analytical near-field correction is proposed by Tsai (2009) which is, however, only valid if $\Delta/R \leq 1$, which is not the case in the presented example. His approximation also requires an estimation of R.

The remaining difference between the dashed red line in Fig. 5 and the input model is due to (i): the far-field approximation of the Green's function. Note also that in the test setup we worked with point sources which is unlikely to be realistic for longer period waves. It is clear from Fig. 5 that the near-field effects are only important at long periods. Additional tests (not shown here) indicate that the near-field error becomes larger with smaller interstation distance. The effect reduces quickly with increasing R, as seen from the magenta curve in Fig. 5(b).

For a combination of far- and near-field sources, no correction is necessary. Fig. 5 shows that this holds even in the presence of attenuation. a denotes the attenuation factor which reduces the signal amplitude by $exp(-a\Delta)$, where Δ is the distance between source and receiver. snr is the signal-to-noise ratio, defined by taking the time-domain cross-correlation and comparing the average absolute amplitude in the signal window to the amplitude in the trailing noise window. An attenuation value of $a = 0.005$ could be realistically found at around 5 s (e.g. Prieto *et al.* 2009). In all our tests, geometrical spreading is also modelled. Attenuation only shows an effect on the phase velocity in combination with random noise. Otherwise, whitening the contributions from each individual source would cancel out any attenuation effect. Our tests show that for very high attenuation values far sources get damped enough to see some near-field effect. In standard situations we recover the dispersion curve reasonably well. Weemstra *et al.* (2014) show that for simultaneously acting sources there is no effect from attenuation on the phase-velocity estimation.

We infer that only when near-field signal is dominant, and a reasonable guess of the average distance R can be made, it is worth comparing the fit to a corrected function $f(x)$ (eq. 29). Such a near-field correction might be necessary in the case of island stations, where the main noise caused by the surge is very close and where a good approximation of R can be made.

3.2 Non-uniform illumination pattern

Ambient-noise imaging relies on the assumption that sources of ambient noise be uniformly distributed with respect to azimuth (A being independent of θ as in eq. 6). In real-world applications, this can only be approximately true. The influence of a non-uniform illumination pattern is shown in Fig. 6. In this example, the intensity of the sources changes with azimuth. The distribution roughly resembles the average source intensities for central Europe, with more sources in the North, associated with the Atlantic Ocean. Details on the determination of the azimuthal dependent source intensity in Europe are given in the following section. The changing number of noise sources causes deviations from the spatially uniform velocity of 3.8 km s^{-1}. Depending on the orientation of the station pair, the errors are around $\pm$0.02 km s^{-1} at 30 s, corresponding to about 0.5 per cent (Fig. 6c). The behaviour is complex and the relation between the source distribution and the velocity bias is non-linear, changing with period and azimuth of the station couple (see also Yang & Ritzwoller 2008; Tsai 2009; Weaver *et al.* 2009; Yao & Van Der Hilst 2009). Averaging over all station pairs gives, however, the velocity of the initial model. This well-known fact is used in the SPAC method, where no homogeneous distribution of noise sources is needed because of the averaging over different station-station azimuths (Aki 1957; Tsai & Moschetti 2010). As explained above, only the symmetric part of the cross-correlation spectrum is considered (i.e. the imaginary part is discarded). Therefore, the velocity deviations in Fig. 6(c) are symmetric for a station couple orientation $\pm$180°.

The influence of a non-uniform illumination pattern gets smaller at high frequencies and large interstation distance (Weaver *et al.* 2009; Yao & Van Der Hilst 2009), which can be understood when looking at eq. (12), showing that the area of noise sources contributing to the measurement reduces in this case. If only few sources in a very narrow area contribute, the variability in source density is negligible. With

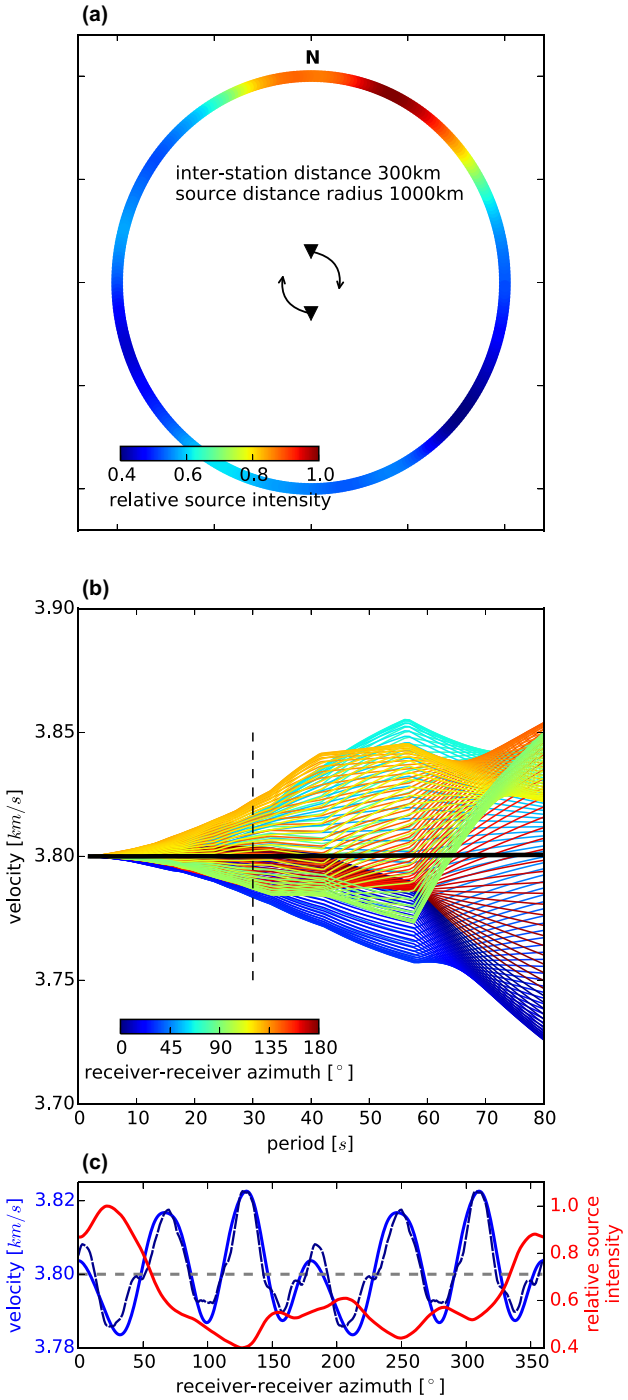

Figure 6. Synthetic tests with non-uniform illumination pattern. (a) Map view of station and source positions. The source intensity follows the average noise-illumination pattern at 30 s for central Europe; details on the determination are given in the following section. All angles in this figure are given in the geographic coordinate system, that is, an azimuth of zero represents the N–S direction. The station couple is rotated in one degree steps. (b) Phase-velocity curves for different station-couple orientations (colours) for the source distribution given in (a). The thick black line is the average of all different azimuth curves. (c) Phase velocity (blue) measured at 30 s [dashed black line in (b)] depending on the station–station azimuth. The isotropic, constant velocity model is shown as grey dashed line. The blue dashed line gives an approximation of the expected velocity bias according to Weaver *et al.* (2009). The intensity of the illumination pattern is shown as red curve.

increasing period (or smaller interstation spacing), the Fresnel area gets larger and the effect of source distribution becomes more important, causing larger deviations from the medium velocity. This explains the behaviour seen in Fig. 6(b), where the variability gets larger with increasing period.

Weaver *et al.* (2009) show that the velocity bias from a non-uniform source illumination is approximately proportional to $\frac{B''(\theta)}{B(\theta)}$, where $B(\theta)$ is the source intensity in dependence of the angle θ and $B''(\theta)$ is its second derivative with respect to θ. In Fig. 6(c), we show that the approximation fits well the general pattern of the velocity bias. The fit becomes better towards shorter periods (not shown here). This is due to

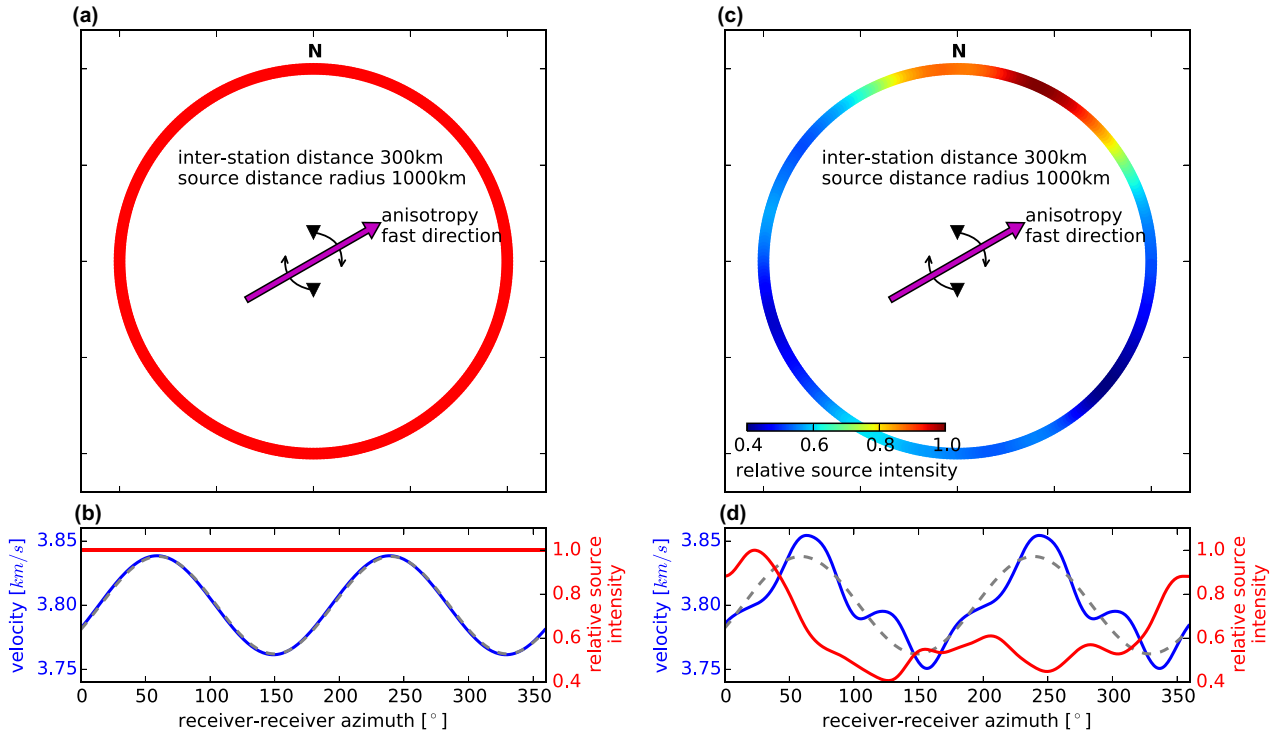

Figure 7. Synthetic model with laterally constant surface wave azimuthal anisotropy. (a) The fast axis of the azimuthal anisotropic medium is at 60° with 1 per cent higher phase velocity compared to the reference velocity of 3.8 km s^{-1}. The slow axis is perpendicular and is 1 per cent slower. (b) Measured phase velocity (blue line) and input medium velocity (grey dashed line), assuming a homogeneous source distribution (red line). The method is able to reproduce the correct velocities in an azimuthally anisotropic velocity model. (c) Same as (a) but with non-homogeneous source distribution, equal to Fig. 6. (d) The resulting phase velocity is a superposition of the influence of anisotropy (b) and source distribution (Fig. 6c).

the high-frequency approximation applied by Weaver *et al.* (2009). Note that in Fig. 6(c) we use a symmetric version of the formula of Weaver *et al.* (2009), given by $\frac{1}{2}\left[\frac{B''(\theta)}{B(\theta)} + \frac{B''(\theta+\pi)}{B(\theta+\pi)}\right]$. This way we account for the fact that in the presented method we only consider the symmetric part of the cross-correlation spectrum.

3.3 Azimuthal anisotropy of surface-wave velocity

In Fig. 7, the influence of an anisotropic surface-wave velocity model is shown, with 1 per cent velocity increase on the fast axis and a 1 per cent decrease on the slow axis. The fast direction is indicated in Fig. 7(a). Recovered phase velocities are exactly the same as in the model. This apparently contradicts the calculations of Yao & Van Der Hilst (2009), who expect a negative velocity bias in this situation. However, this is explained by their assumption of plane waves, as opposed to our derivation in terms of point sources. As this difference in method concerns the calculation of the synthetic data, we expect no discrepancy in applications to real data for azimuthal anisotropy.

The velocity curve in Fig. 7(d) shows the effect of anisotropic velocities in combination with a non-homogeneous source distribution. The same velocity curve can be obtained by summing the effects of anisotropy and non-homogeneous source distribution separately from the corresponding curves in Fig. 6(c) and Fig. 7.

We infer that azimuthal anisotropy can be recovered without bias by the ANM—at least with the straight ray assumption in this work. The results might be slightly different when ray bending is allowed or finite frequency kernels are used.

4 COMPARISON BETWEEN AMBIENT-NOISE AND EARTHQUAKE DATA

The 'Two-Station Method' for measuring surface-wave phase velocity (e.g. Sato 1955; Kovach 1978; Meier *et al.* 2004; Soomro *et al.* 2016) is based on using earthquakes as signal sources. When the epicentre is approximately aligned with the station couple, the phase term of the cross-correlation can be evaluated and gives an estimate of the phase velocity. However, selection of smooth parts of the dispersion curves and averaging over a large number of events is necessary to obtain a reliable path-average phase velocity (de Vos *et al.* 2013; Soomro *et al.* 2016). In this section, the phase-velocity measurements from the ANM described above are compared to those obtained from the two-station or 'earthquake' method (EQM). Since the parameters of interest are the same as well as the wave types (Rayleigh and Love), the methods are supposed to give coherent results. However, the signal sources are completely independent, although some scattered earthquake coda waves are certainly making a minor contribution to the ambient-noise wavefield. The difference in approach leads to different, method-specific problems. The EQM has to cope with the influence of strong heterogeneity between the stations and on the path from the epicentre to the

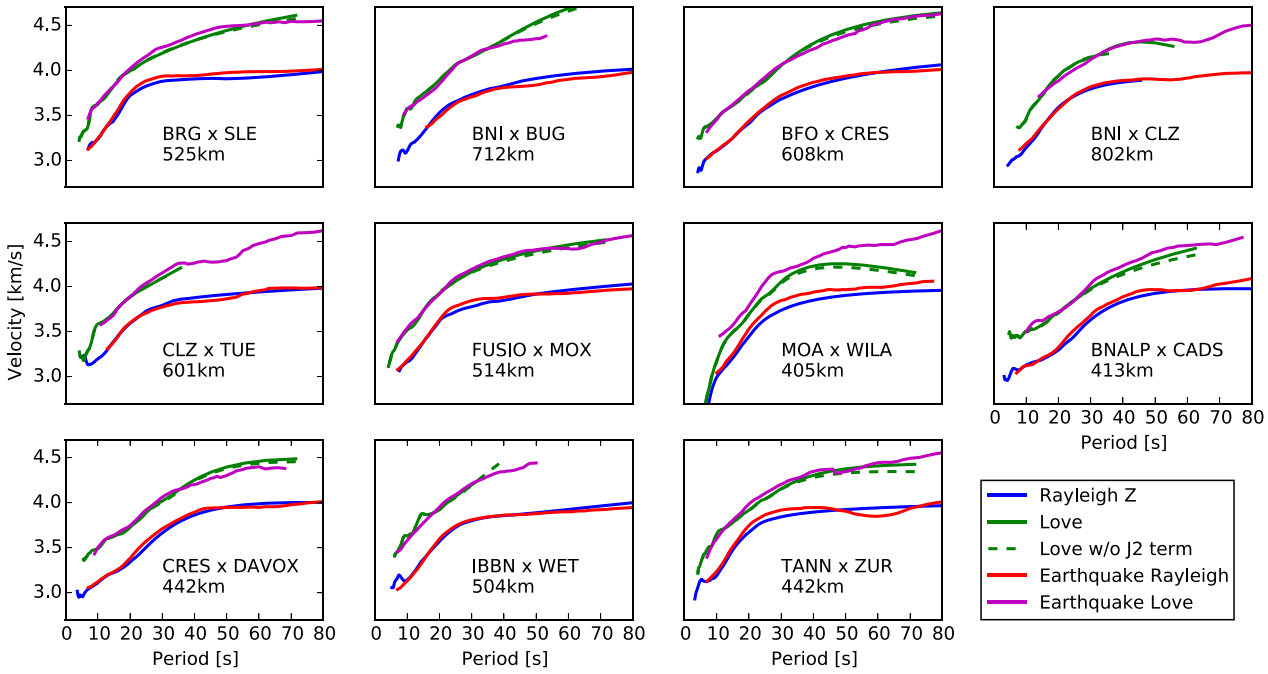

Figure 8. Rayleigh- and Love-wave dispersion curves for different station couples. Each plot gives the phase velocities measured with ambient-noise and earthquake data. For Love waves, the curve is shown with and without correction from eq. (19). Station names and interstation distance are indicated in each window.

stations, the influence of higher modes and noise. It has been shown that time–frequency analysis of the cross-correlation, averaging and selection of smooth parts of single event measurements diminish these effects strongly. However, especially at shorter interstation distances a small positive bias may remain (Soomro *et al.* 2016). The ANM hinges on the assumption of a perfect distribution of sources and scatterers that have to be uncorrelated and suffers from the low energy content of the coherent part of the wavefield.

The presented data were recorded in central Europe, mostly the Alpine region and are publicly available. The ambient-noise data is prepared and evaluated according to the method presented above. Details on the compilation of the earthquake-based data set based on an automated processing scheme involving a number of quality checks are given in Soomro *et al.* (2016).

4.1 Dispersion curves

In Fig. 8, we compare phase-velocity dispersion curves as measured via EQM versus ANM for several station couples. The phase velocity has been picked using the averaged EQM as reference in order to introduce no bias (see also Fig. 4). We have not noticed any dependence of the results on the reference curve as long as it does not deviate more than ± 1 km s^{-1} from the expected value. Both Love and Rayleigh wave phase velocities agree well, with discrepancies generally well below 0.1 km s^{-1}. The effects from the Love wave correction from eq. (19), that is, including the J_2 term, are shown (see also Fig. 3). The difference is largest at long period and short interstation distance, and becomes approximately negligible below 40 s. Not all measurements are of equal quality: just one or two wrong picks due to noise at the low-frequency end of the cross-correlation spectrum can lead to important deviations such as for station couple MOA-WILA.

Fig. 9 provides a more general comparison by showing the averaged measurements from all station pairs for which data from both methods are available. The average discrepancies are as large as almost 0.05 km s^{-1} for Rayleigh and 0.06 km s^{-1} for Love waves; in both cases this amounts to approx. 1 per cent of the reference velocity. Fewer Love-wave dispersion measurements are available which could cause the slightly higher discrepancies seen in Fig. 9(b). Apart from the dispersion curves, also the data coverage for the ANM depending on the period is shown. For this comparison, we choose only station pairs where measurements at all sampled periods between 20 and 50 s are available. The Love-wave discrepancy is reduced, on average, by accounting for the J_2 term in Love-wave cross-correlation (Section 2.4). The effect of the J_2 term is also shown for the R-component dispersion curve. However, this correction alone cannot explain the discrepancies between the methods.

The differences between ANM and EQM are highest between 25 and 35 s. The histogram in Fig. 9(d) shows how the differences between the two methods are distributed at 25 s period. Few outliers can be identified for the Rayleigh-wave comparison, but they are not numerous enough to contribute significantly to this discrepancy.

Average faster velocities from the EQM in comparison to the ANM have also been reported by Zhou *et al.* (2012) (0.012 km s^{-1} from comparison of phase-velocity maps), Ritzwoller *et al.* (2011) (0.004 km s^{-1} from comparison of phase-velocity maps), Shen *et al.* (2013) (0.001 km s^{-1} from comparison of phase-velocity maps) and Yao *et al.* (2008) (0.06 km s^{-1} from comparison of averaged phase velocity

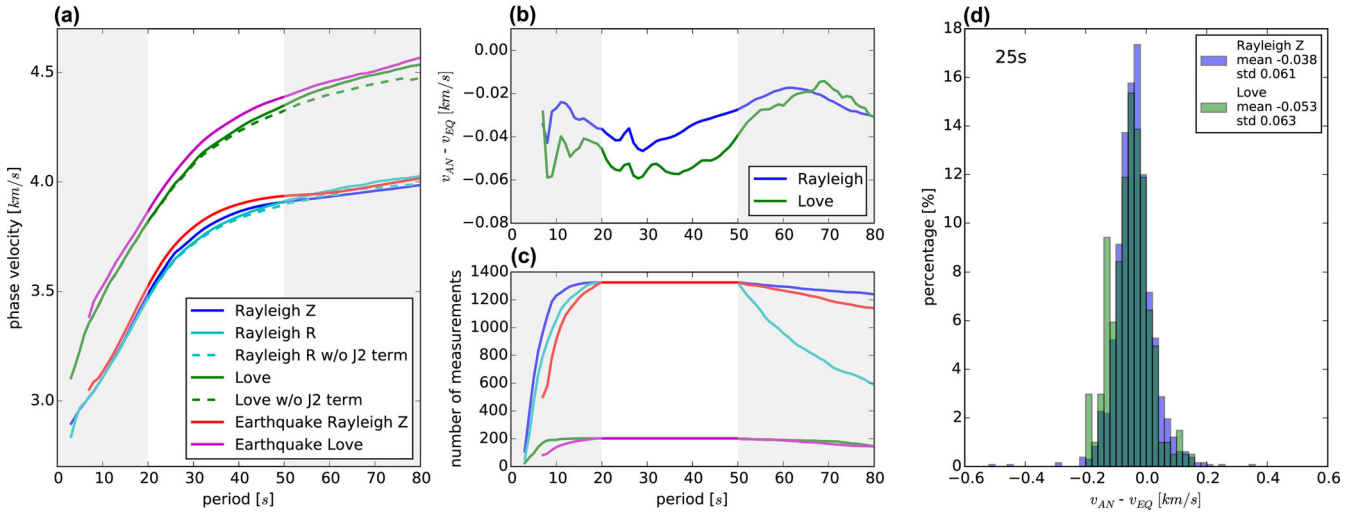

Figure 9. (a) Average of the phase-velocity dispersion curves, comparing EQM and ANM. The ANM covers periods down to about 4 s whereas the EQM allows measurements up to very long periods of 250 s and beyond. The same station couples are compared. The valid range for comparison is distinguished by a white background. Noise measurements predict slightly slower velocities, with differences around 0.04–0.06 km s^{-1}. The dispersion curves for Love and Rayleigh R-component correlations are shown with (solid line) and without (dashed line) the additional J2-term of eq. (19). (b) Difference between average dispersion curves from (a). (c) Number of data points used in the comparison. Only station pairs where data between 20 and 50 s are available are used. Fewer Love-wave measurements are available for the comparison. Line colours correspond to the legend in (a). (d) Differences between EQ and AN measurements at 25 s period. Their distribution is approximately Gaussian, with few outliers.

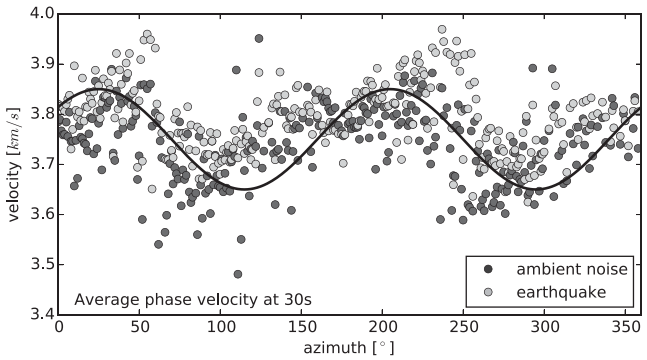

Figure 10. Rayleigh phase velocity at 30 s period for different receiver–receiver azimuth; averaged over all station couples with identical orientation. The ANM and the EQM show the same pattern of fast and slow direction, with fast direction around 25° and 205° and ±0.1 km s^{-1} variability as shown by the black line. The average discrepancy of 0.05 km s^{-1} between the earthquake and the ambient-noise measurements is well visible.

curves) - all taken around 30 s. Without stating whether the discrepancy is positive or negative, Köhler *et al.* (2012) also find residuals of up to 1.5 per cent at 25 s. To our knowledge, there are no studies that show faster measurements from the ANM, which leads us to believe that this discrepancy is systematic. There are several possible reasons for the bias between ambient-noise and earthquake results:

(i) In Fig. 5, we show that near-field sources represent a possible reason for erroneous phase-velocity measurements from ambient noise. However, we can infer from Fig. 9 that our ANM measurements are not biased by the (a priori possible) presence of many near-field sources: this would have resulted in ANM estimates of velocity being higher than EQM ones, contradicting the data in Fig. 9. This is in agreement with the fact that most ambient-noise signal recorded in Europe is generated in the surrounding seas/oceans.

(ii) Non uniformity in noise-source distribution with respect to azimuth. This influence is hard to quantify as the effects of a non-uniform illumination pattern are complex and can cause positive as well as negative velocity deviations (e.g. Yang & Ritzwoller 2008; Tsai 2009; Yao & Van Der Hilst 2009). However, this should cancel out in the averaging procedure applied in Fig. 9, as shown in Section 3.2.

(iii) Off-path propagation between the earthquake event and the station couple. The EQM uses the difference in epicentral distances and not the interstation distance to calculate phase differences, which reduces the effect from earthquakes which are not located exactly on the station great circle. The bias from event mislocation would be frequency independent. Therefore, event mislocation is an unlikely cause for the discrepancies evidenced in Figs 9 and 11. Velocity heterogeneity causes deviations from the direct path and introduces an error in the differential path. For short interstation distances, this will result in a positive bias of the estimated phase velocities. At larger interstation distances this effect is however reduced by wave front healing and by averaging over events from different source regions (Soomro *et al.* 2016), because earth heterogeneity additionally curves wave fronts, which can result in both positive and negative perturbations of the phase velocity (Wielandt 1993).

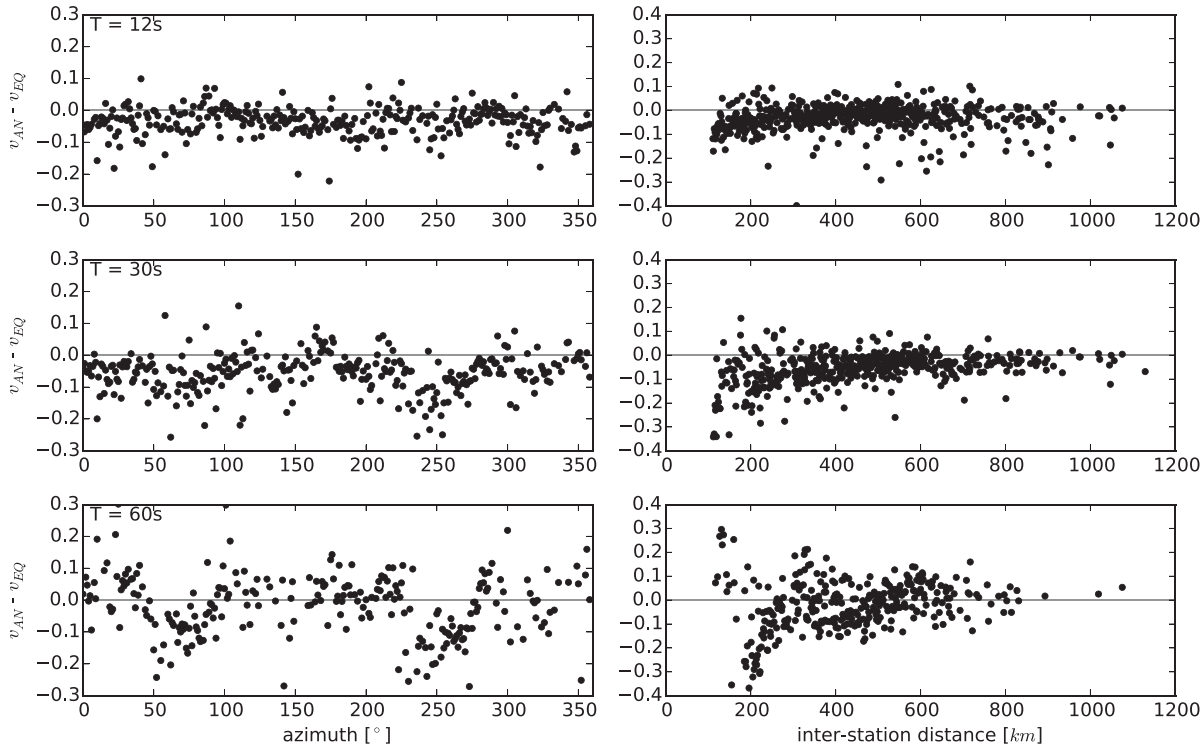

Figure 11. Difference in the Rayleigh-wave phase velocity from earthquake (v_{EQ}) and ambient-noise (v_{AN}) measurements in km s^{-1}. The differences are an average of all station couples sorted according to the azimuth of the station couple orientation (left) and interstation distance (right) at three different periods. An azimuth of zero stands for a north–south orientation. The variability gets higher with longer periods, which is because of the decrease in number of measurements but also because of the larger Fresnel zone. The Fresnel zone effect is also visible in the variation with distance, getting smaller for large interstation distances.

(iv) Teleseismic, single-event measurements will have a broader sensitivity kernel. This effect is diminished by averaging (de Vos *et al.* 2013). In general, the sensitivity to structure will be slightly different for the ANM and the EQM, which can give different velocity estimations when the medium velocity is laterally changing.

(v) Soomro *et al.* (2016) mention the influence of surface-wave overtones as another possible cause for a positive bias in the EQM estimates of phase velocity. This effect is minimized by the time-frequency analysis. No fk-filter or time window selection is done in case of the ambient-noise data. The relative contribution of higher modes to the ambient-noise wavefield are estimated quite differently in the literature and seem to be dependent of the region. However, most authors state that fundamental-mode surface waves dominate the ambient-noise records, especially at periods longer than 5 s (Lacoss *et al.* 1969; Pedersen & Krüger 2007; Nishida *et al.* 2008; Yao *et al.* 2011). Some preliminary numerical tests of our method indicate that even in the presence of a secondary, faster signal emitted by each noise source, roughly corresponding to the first higher mode, the fundamental mode phase-velocity signal dominates the phase-velocity measurement procedure and the fundamental mode phase velocity is correctly reconstructed. Finally, it should be noted that misidentification of fundamental-mode versus overtone phases would result in an overestimate (rather than the observed, suspected underestimate) of fundamental mode phase velocity. We infer that higher mode contamination in the ambient-noise measurements is unlikely to explain the observed EQM-ANM discrepancy.

(vi) In principle, scattering may introduce spurious correlations and therefore influence the measured velocity (e.g. Boschi *et al.* 2013). However, on the scale considered here, it is reasonable to assume that many scattering structures are present and that their geographic distribution is relatively uniform. In such a situation, it has been shown (Larose *et al.* 2008) that scatterers will actually contribute to a better reconstruction of the Green's function. If present, scattering might have some systematic effects on EQM data, but these are presumably small and their analysis is beyond the scope of this study.

We show in Fig. 10 phase-velocity estimates from both ANM and EQM at 30 s period, for all possible station couples, as a function of receiver-receiver azimuth. The discrepancy between ANM and EQM does not show any strong dependence on azimuth, indicating that, if the European crust/upper mantle is azimuthally anisotropic, both methods should resolve this equally well. Indeed, Fig. 10 does suggest that the region of interest is anisotropic. Fry *et al.* (2010) show that, at 30 s, the average anisotropy fast direction in the western and central Alpine region is around 0° with 2.5 per cent anisotropic anomaly. The magnitude fits our results very well, with 2.5 per cent of 3.8 km s^{-1} being around 0.1 km s^{-1}. The direction deviates slightly from the one shown in Fig. 10, but this is probably because we average over a larger region.

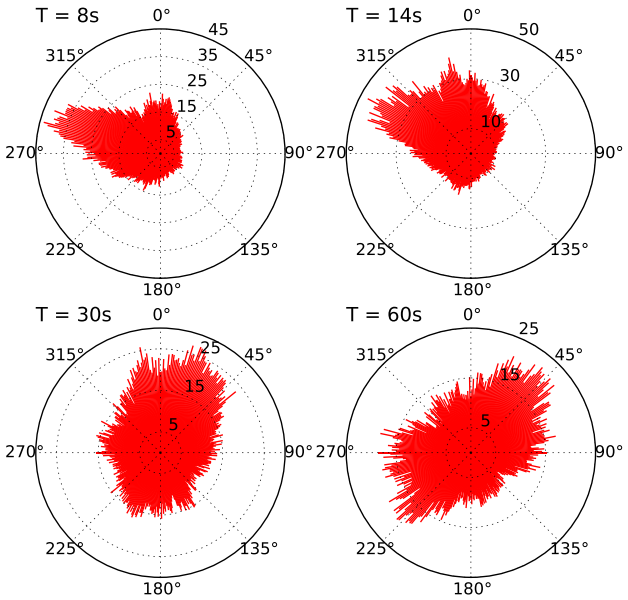

Figure 12. Signal-to-noise ratio at different periods according to the azimuth. A high signal-to-noise ratio shows strong sources generating ambient noise coming from the specific direction. The periods at 8 and 14 s stand for the primary and secondary microseisms band, respectively. In both cases, the strongest source activity comes from the Atlantic. The long-period sources are distributed more isotropically. The distribution at 30 s serves as model for the synthetic test in Fig. 7.

Fig. 11 separates the effects from station couple orientation, interstation distance and period. The effect of the sensitivity kernels can be recognized easily: the variability of the noise data increases as the station-station spacing gets smaller and with increasing period. This effect could be explained with a non-uniform illumination pattern as indicated above (Fig. 7).

The fluctuations with azimuth are most likely not associated with anisotropy, since that seems to be resolved by both ANM and EQM (Fig. 10). In the shown case, the average velocity discrepancies are as high as 2.5 per cent for certain orientations. The difference decreases for longer interstation distances. This might be partly caused by a small remaining positive bias in the EQM for small interstation distances.

4.2 Distribution of noise sources

Fig. 12 shows the signal-to-noise ratio for Rayleigh waves at different periods, obtained by filtering the stacked cross-correlations and comparing the maximum signal amplitude with the trailing noise in the time domain, according to Yang & Ritzwoller (2008). The bounds of the signal window are given by the interstation distance divided by the maximum (5 km s^{-1}) and minimum (2 km s^{-1}) expected velocity, respectively. We thus obtain a signal-to-noise estimate for each station couple for the forward (waves travelling from station 1 to 2) and backwards (vice-versa) empirical Green's function. In the first and secondary microseisms band, a preferential direction of noise sources is clearly visible with most of the energy coming from the Atlantic (Pedersen & Krüger 2007; Campillo & Roux 2015).

The illumination pattern used to construct synthetic data in Section 3 (Fig. 7) was derived from the signal-to-noise distribution at 30 s shown in Fig. 12. We already demonstrated that such noise source distribution does not cause any systematic bias. Further synthetic tests of ANM, focused on the effects of non-uniform station distribution (results not shown here in the interest of brevity) did not result in systematic errors, either. This suggests that the actual station distribution covers sufficiently well the whole azimuthal range. The synthetic tests, however, significantly simplify the illumination pattern and the medium. For example, the source intensity distribution will change for every station pair considered, so that the zero-average bias, as seen in the synthetic test, might not hold. A non-uniform velocity model causes also deviations from the ray-theoretical measurement between two stations (e.g. Tsai 2009). The expected effects are, however, small for a sufficiently large number of stations considered.

4.3 Phase-velocity maps

The analysis of Section 4 suggests that a small, but possibly significant discrepancy exists between phase-velocity estimates based on the ANM and the EQM. To quantify its practical relevance, we next determine phase-velocity maps from both ANM and EQM data and evaluate their agreement (Fig. 13). The phase velocities at a period of 25 s are taken as an intermediate value where both approaches have good data coverage. In the inversion process. the test region is divided in 0.1° wide squares and the sensitivities are calculated in ray-theory approximation, following, for example, Verbeke *et al.* (2012). Both ANM and EQM inversions are parametrized and regularized in the same way, via roughness damping only (e.g. Boschi & Dziewonski 1999). Importantly, we only include in this exercise station couples for which data from both methods are available at the period in question.

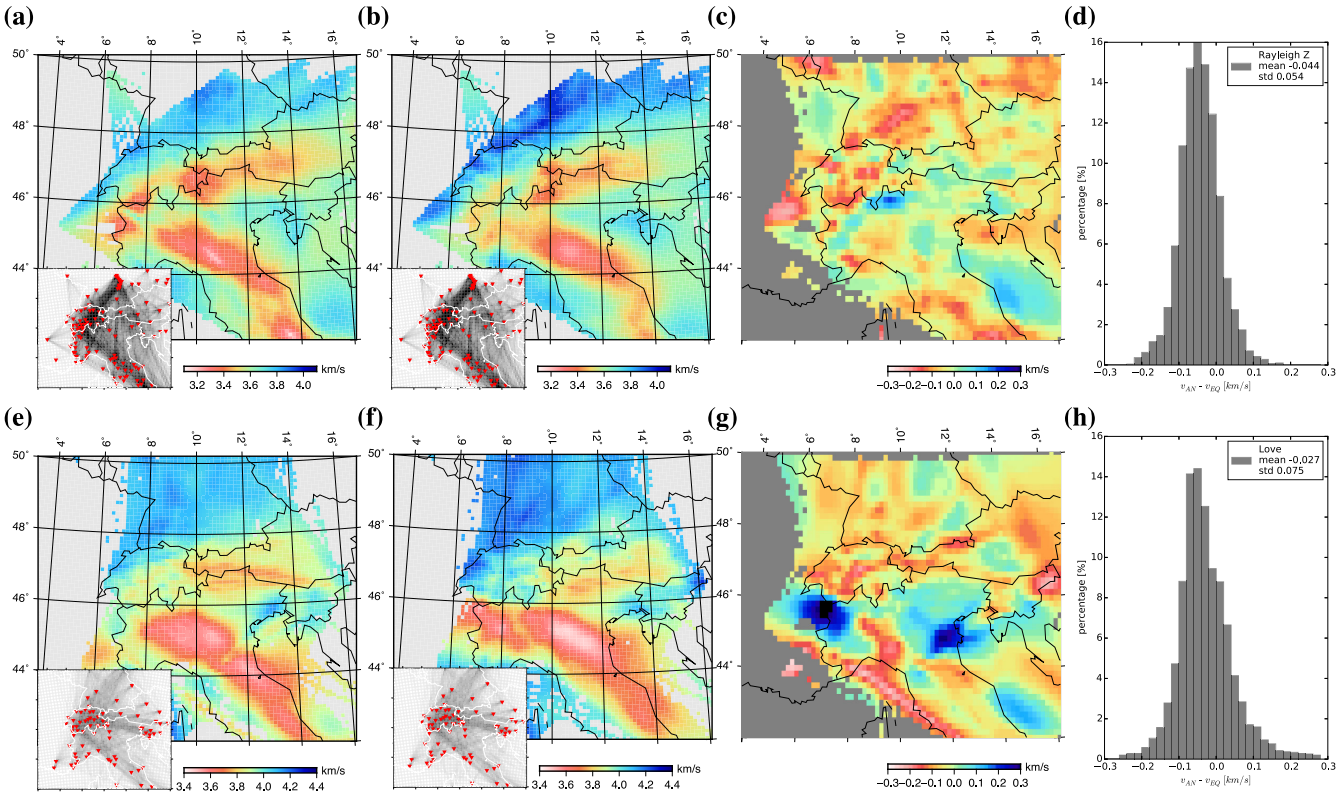

Figure 13. Comparison of phase-velocity maps at 25 s period for Rayleigh (top) and Love (bottom) waves. (a) Rayleigh, ANM, (b) Rayleigh, EQM, (c) difference between (a) and (b). (d) Differences from (c) as histogram. (e–h) Same as (a–d) for Love waves.

The Rayleigh-wave maps (Fig. 13) should be seen as a depth-average of the lower-crust/upper mantle velocity structures. Both ANM and EQM show the thickened crust underneath the Alpine orogen, corresponding to low phase velocities. Pronounced velocity reductions characterize also the Po-plain basin in northern Italy and the Apennines. The overall structures of Fig. 13 are in good agreement with phase-velocity maps from Stehly *et al.* (2009); Verbeke *et al.* (2012); Molinari *et al.* (2012).

Differences between ANM and EQM are in the range of ± 0.3 km s^{-1} for both Love- and Rayleigh waves. The inversion and smoothing process suppresses outliers that are visible in 9d. Otherwise, discrepancies in the phase-velocity maps are comparable to the ones from direct comparison of the phase-velocity curves.

Several studies similarly compare Rayleigh phase-velocity maps: Zhou *et al.* (2012) report maximum phase-velocity differences of 0.2 km s^{-1}, but with a smaller mean of -0.012 km s^{-1}. Yang & Ritzwoller (2008) find deviations of 0.15 km s^{-1}. Very small discrepancies are found in the maps of Shen *et al.* (2013) who give a maximum of 0.08 km s^{-1} and a mean of -0.001 km s^{-1}. This is similar to the small mean deviation of -0.004 km s^{-1} reported by Ritzwoller *et al.* (2011).

Phase-velocity curves from the EQM are determined for each event aligned with a station pair, and then averaged over all such events. This results in smoother estimates of the phase-velocity dispersion. Additionally, (Soomro *et al.* 2016) applied certain smoothness constraints, discarding parts of the dispersion curve that are particularly rough. We do not smoothen our phase-velocity curves and some roughness remains as seen in Fig. 4. This results in higher standard deviations and higher/lower maximum/minimum values of c. We have seen that an inhomogeneous source distribution influences the measured phase velocity for individual station couples: we show above that this does not influence the mean, but it could cause a higher standard deviation.

Love waves at a given period are sensitive to shallower structures than Rayleigh waves at the same period. The Love-wave maps of Fig. 13 show similar structures as the Rayleigh-wave ones. Higher sensitivities to shallower crustal structures result in a very prominent low-velocity zone associated with the Po-plain. The mean discrepancy gets smaller in the phase-velocity map comparison, compared to the phase-dispersion curves (Fig. 9). This is presumably explained by the geographic distribution of station-station phase-velocity measurements on the map and by the smoothing in the inversion process. To our knowledge, no other studies compare the results of ANM and EQM for Love waves. Our results suggest that the bias between the methods is independent of the wave type.

We evaluate the size of the structures that are resolvable by the station configuration of Fig. 13 with a checkerboard test in Fig. 14. Theoretical receiver-receiver dispersion curves corresponding to this synthetic model are computed using ray-theory (but neglecting ray bending) and a finer parametrization (1 km) than that of the tomographic inversions. They are then inverted with the same parametrization and regularization parameters as on the maps above. The comparison shows that high discrepancies in Fig. 13 even occur in regions of good coverage.

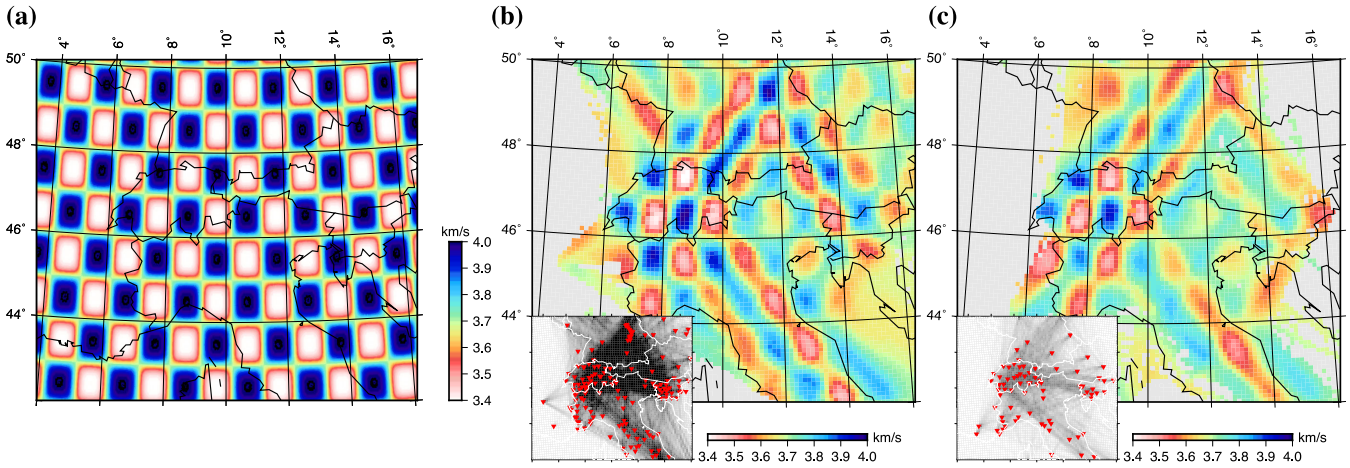

Figure 14. Resolution test with the ray coverage from Fig. 13. (a) Synthetic checkerboard model with 1° cells. (b) Recovered phase-velocity map for the Rayleigh-wave case. (c) Same as (b) for the Love-wave case.

5 CONCLUSIONS

In this work, we prove the validity of the ANM by comparison with the well-established EQM (Sato 1955; Kovach 1978; Meier *et al.* 2004; Soomro *et al.* 2016). The basic theory of the ANM is revised in order to evaluate its limitations and the approximations that it involves. This includes a far-field assumption, the effects of anisotropic source distribution and azimuthal velocity anisotropy, whose influence is examined using synthetic tests. We also discuss in detail how Love-wave phase velocity can be extracted from ambient noise, show that the mathematical expression for noise cross-correlation is slightly different for Love waves with respect to the vertical component of Rayleigh waves, and verify that the error caused by neglecting such difference (as has sometimes been done) is, generally, small, but can become important for short interstation distance and long periods. We show that the same issue arises when extracting Rayleigh waves from the radial, rather than vertical component of recorded noise.

The central European Alps are taken as example region to test the differences between the two methods. A good agreement in the resulting phase velocities is found with average discrepancies smaller than 0.06 km s^{-1}. ANM-based velocity estimates are, on average, slightly lower than those obtained by the EQM, as indicated also by other authors (Yao *et al.* 2008; Ritzwoller *et al.* 2011; Zhou *et al.* 2012; Shen *et al.* 2013), reporting average discrepancies for Rayleigh-wave phase velocity of −0.07, −0.004, −0.012 and −0.001 km s^{-1}, respectively. The fact that this bias seems to be very stable and not randomly changing with period, distance and/or azimuth suggests that it should be explained by methodological differences. The largest average discrepancy is found for both Love and Rayleigh waves at periods around 30 s, where Rayleigh waves are particularly sensitive to heterogeneous Moho topography (Meier *et al.* 1997).

We extract the azimuthally dependent signal-to-noise ratio at this period and use it in a synthetic model in order to test for the effects of a non-uniform illumination pattern. Our synthetic results suggest that, on average, the observed bias in noise-source distribution does not affect significantly our ANM phase-velocity estimates. We verify also that azimuthal anisotropy in surface-wave velocity can be reconstructed properly by the ANM. We infer that the small residual discrepancy between EQM and ANM dispersion measurements is the result of a combination of factors, including lateral velocity variations and differences in sensitivity of EQM versus ANM data to structure, which are not accounted for if, like here, the ray-theory approximation is used. We also assume a small influence from higher modes on the EQM. Further research will be necessary to fully explain the bias between the methods.

We finally show that, in the context of applications to crust and upper mantle imaging, the discussed discrepancy is sufficiently small to be negligible with respect to other effects: the good agreement between phase-velocity maps based on EQM versus ANM is illustrated by Fig. 13. This compatibility is key to combining the results of both methods in order to cover a wider period range as done, for example, by Yao *et al.* (2008) or Zhou *et al.* (2012). We suggest that joint inversion of ANM and EQM dispersion data will provide 3-D images of the uppermost mantle at resolution significantly higher than achieved by either data set when inverted alone. In this endeavour, it will be important to take into account some complex effects that we quantified here, namely the contribution of J_2 to the Love-wave and radial-component ANM cross-correlation spectra.

ACKNOWLEDGEMENTS

We are grateful to Göran Ekström, Jean-Paul Montagner, the editor Michael Ritzwoller and the two anonymous reviewers for their helpful comments. We are grateful to all the network operators providing data to the EIDA archive (http://www.orfeus-eu.org/eida, last accessed April 2015). We thank the makers of Obspy (Beyreuther *et al.* 2010). Graphics were created with Python Matplotlib and GMT (Wessel *et al.* 2013). CW is supported by the Netherlands Research Centre for Integrated Solid Earth Science (ISES). This project has received funding from the European Union's Horizon 2020 research and innovation programme under the Marie Sklodowska-Curie grant agreement No. 641943.

REFERENCES

Abramowitz, M. & Stegun, I.A., 1964. *Handbook of Mathematical Functions: With Formulas, Graphs, and Mathematical Tables,* no. 55, Courier Corporation.

Agius, M.R. & Lebedev, S., 2013. Tibetan and Indian lithospheres in the upper mantle beneath Tibet: evidence from broadband surface-wave dispersion, *Geochem. Geophys. Geosyst.,* **14**(10), 4260–4281.

Aki, K., 1957. Space and time spectra of stationary stochastic waves, with special reference to microtremors, *Bull. Earthq. Res. Inst.,* **35,** 411–451.

Aki, K. & Richards, P.G., 2002. *Quantitative Seismology,* University Science Books.

Basini, P., Nissen-Meyer, T., Boschi, L., Casarotti, E., Verbeke, J., Schenk, O. & Giardini, D., 2013. The influence of nonuniform ambient noise on crustal tomography in Europe, *Geochem. Geophys. Geosyst.,* **14**(5), 1471–1492.

Bender, C.M. & Orszag, S.A., 1978. *Advanced Mathematical Methods for Scientists and Engineers,* McGraw-Hill.

Bensen, G., Ritzwoller, M., Barmin, M., Levshin, A., Lin, F., Moschetti, M., Shapiro, N. & Yang, Y., 2007. Processing seismic ambient noise data to obtain reliable broad-band surface wave dispersion measurements, *Geophys. J. Int.,* **169**(3), 1239–1260.

Bettig, B., Bard, P., Scherbaum, F., Riepl, J., Cotton, F., Cornou, C. & Hatzfeld, D., 2001. Analysis of dense array noise measurements using the modified spatial auto-correlation method (SPAC): application to the Grenoble area, *Boll. Geofis. Teor. Appl.,* **42**(3–4), 281–304.

Beyreuther, M., Barsch, R., Krischer, L., Megies, T., Behr, Y. & Wassermann, J., 2010. ObsPy: a Python toolbox for seismology, *Seismol. Res. Lett.,* **81**(3), 530–533.

Boschi, L. & Dziewonski, A.M., 1999. High-and low-resolution images of the earth's mantle: implications of different approaches to tomographic modeling, *J. geophys. Res.,* **104**(B11), 25 567–25 594.

Boschi, L. & Weemstra, C., 2015. Stationary-phase integrals in the cross-correlation of ambient noise, *Rev. Geophys.,* **53**(2), 411–451.

Boschi, L., Weemstra, C., Verbeke, J., Ekström, G., Zunino, A. & Giardini, D., 2013. On measuring surface wave phase velocity from station–station cross-correlation of ambient signal, *Geophys. J. Int.,* **192**(1), 346–358.

Campillo, M. & Roux, P., 2015. Crust and lithospheric structure – Seismic imaging and monitoring with ambient noise correlations, in *Treatise on Geophysics,* 2nd edn, Vol. 1, pp. 391–417, eds Romanowicz, B. & Dziewonski, A., Elsevier, Amsterdam.

de Vos, D., Paulssen, H. & Fichtner, A., 2013. Finite-frequency sensitivity kernels for two-station surface wave measurements, *Geophys. J. Int.,* **194**(2), 1042–1049.

Ekström, G., 2014. Love and Rayleigh phase-velocity maps, 5–40 s, of the western and central USA from USArray data, *Earth planet. Sci. Lett.,* **402,** 42–49.

Ekström, G., Abers, G.A. & Webb, S.C., 2009. Determination of surface-wave phase velocities across USArray from noise and Aki's spectral formulation, *Geophys. Res. Lett.,* **36**(18), doi:10.1029/2009GL039131.

Endrun, B., Meier, T., Bischoff, M. & Harjes, H.-P., 2004. Lithospheric structure in the area of Crete constrained by receiver functions and dispersion analysis of Rayleigh phase velocities, *Geophys. J. Int.,* **158**(2), 592–608.

Endrun, B., Lebedev, S., Meier, T., Tirel, C. & Friederich, W., 2011. Complex layered deformation within the Aegean crust and mantle revealed by seismic anisotropy, *Nat. Geosci.,* **4**(3), 203–207.

Friedrich, A., Krüger, F. & Klinge, K., 1998. Ocean-generated microseismic noise located with the Gräfenberg array, *J. Seismol.,* **2**(1), 47–64.

Fry, B., Deschamps, F., Kissling, E., Stehly, L. & Giardini, D., 2010. Layered azimuthal anisotropy of Rayleigh wave phase velocities in the European Alpine lithosphere inferred from ambient noise, *Earth planet. Sci. Lett.,* **297**(1), 95–102.

Halliday, D. & Curtis, A., 2008. Seismic interferometry, surface waves and source distribution, *Geophys. J. Int.,* **175**(3), 1067–1087.

Harmon, N., Gerstoft, P., Rychert, C.A., Abers, G.A., Salas de La Cruz, M. & Fischer, K.M., 2008. Phase velocities from seismic noise using beamforming and cross correlation in Costa Rica and Nicaragua, *Geophys. Res. Lett.,* **35**(19), doi:10.1029/2008GL035387.

Hasselmann, K., 1963. A statistical analysis of the generation of microseisms, *Rev. Geophys.,* **1**(2), 177–210.

Hillers, G., Graham, N., Campillo, M., Kedar, S., Landès, M. & Shapiro, N., 2012. Global oceanic microseism sources as seen by seismic arrays and predicted by wave action models, *Geochem. Geophys. Geosyst.,* **13**(1), doi:10.1029/2011GC003875.

Köhler, A., Weidle, C. & Maupin, V., 2012. Crustal and uppermost mantle structure of southern Norway: results from surface wave analysis of ambient seismic noise and earthquake data, *Geophys. J. Int.,* **191**(3), 1441–1456.

Korostelev, F. *et al.*, 2015. Magmatism on rift flanks: Insights from ambient noise phase velocity in Afar region, *Geophys. Res. Lett.,* **42**(7), 2179–2188.

Kovach, R.L., 1978. Seismic surface waves and crustal and upper mantle structure, *Rev. Geophys.,* **16**(1), 1–13.

Lacoss, R.T., Kelly, E.J. & Toksöz, M.N., 1969. Estimation of seismic noise structure using arrays, *Geophysics,* **34**(1), 21–38.

Larose, E., Roux, P., Campillo, M. & Derode, A., 2008. Fluctuations of correlations and Green's function reconstruction: role of scattering, *J. Appl. Phys.,* **103**(11), 114907, doi:10.1063/1.2939267.

Lebedev, S., Boonen, J. & Trampert, J., 2009. Seismic structure of Precambrian lithosphere: new constraints from broad-band surface-wave dispersion, *Lithos,* **109**(1), 96–111.

Lin, F.-C., Moschetti, M.P. & Ritzwoller, M.H., 2008. Surface wave tomography of the western United States from ambient seismic noise: Rayleigh and Love wave phase velocity maps, *Geophys. J. Int.,* **173**(1), 281–298.

Longuet-Higgins, M.S., 1950. A theory of the origin of microseisms, *Phil. Trans. R. Soc. A,* **243**(857), 1–35.

Meier, T., Malischewsky, P. & Neunhöfer, H., 1997. Reflection and transmission of surface waves at a vertical discontinuity and imaging of lateral heterogeneity using reflected fundamental Rayleigh waves, *Bull. seism. Soc. Am.,* **87**(6), 1648–1661.

Meier, T., Dietrich, K., Stöckhert, B. & Harjes, H.-P., 2004. One-dimensional models of shear wave velocity for the eastern Mediterranean obtained from the inversion of Rayleigh wave phase velocities and tectonic implications, *Geophys. J. Int.,* **156**(1), 45–58.

Molinari, I., Raileanu, V. & Morelli, A., 2012. A crustal model for the Eastern Alps region and a new Moho map in southeastern Europe, *Pure appl. Geophys.,* **169**(9), 1575–1588.

Nishida, K., Kawakatsu, H. & Obara, K., 2008. Three-dimensional crustal S wave velocity structure in Japan using microseismic data recorded by Hi-net tiltmeters, *J. geophys. Res.,* **113**(B10), doi:10.1029/2007JB005395.

Pedersen, H.A. & Krüger, F., 2007. Influence of the seismic noise characteristics on noise correlations in the Baltic shield, *Geophys. J. Int.,* **168**(1), 197–210.

Prieto, G.A., Lawrence, J.F. & Beroza, G.C., 2009. Anelastic Earth structure from the coherency of the ambient seismic field, *J. geophys. Res.,* **114**(B7), doi:10.1029/2008JB006067.

Ritzwoller, M.H., Lin, F.-C. & Shen, W., 2011. Ambient noise tomography with a large seismic array, *C. R. Geosci.,* **343**(8), 558–570.

Sánchez-Sesma, F.J. & Campillo, M., 2006. Retrieval of the Green's function from cross correlation: the canonical elastic problem, *Bull. seism. Soc. Am.,* **96**(3), 1182–1191.

Sato, Y., 1955. Analysis of dispersed surface waves by means of Fourier Transform: Part 1, *Bull. Earthq. Res. Tokyo Univ.,* **33,** 33–47.

Seats, K.J., Lawrence, J.F. & Prieto, G.A., 2012. Improved ambient noise correlation functions using Welch's method, *Geophys. J. Int.,* **188**(2), 513–523.

Shen, W., Ritzwoller, M.H. & Schulte-Pelkum, V., 2013. A 3-D model of the crust and uppermost mantle beneath the Central and Western US by joint inversion of receiver functions and surface wave dispersion, *J. geophys. Res.,* **118**(1), 262–276.

Snieder, R., 1986. 3-D linearized scattering of surface waves and a formalism for surface wave holography, *Geophys. J. Int.,* **84**(3), 581–605.

Snieder, R., 2004. Extracting the Green's function from the correlation of coda waves: a derivation based on stationary phase, *Phys. Rev. E,* **69**(4), 046610, doi:10.1103/PhysRevE.69.046610.

Soomro, R., Weidle, C., Cristiano, L., Lebedev, S., Meier, T. & PASSEQ Working Group, 2016. Phase velocities of Rayleigh and Love waves in central and northern Europe from automated, broad-band, interstation measurements, *Geophys. J. Int.,* **204**(1), 517–534.

Stehly, L., Campillo, M. & Shapiro, N., 2006. A study of the seismic noise from its long-range correlation properties, *J. geophys. Res.,* **111**(B10), doi:10.1029/2005JB004237.

Stehly, L., Fry, B., Campillo, M., Shapiro, N., Guilbert, J., Boschi, L. & Giardini, D., 2009. Tomography of the Alpine region from observations of seismic ambient noise, *Geophys. J. Int.,* **178**(1), 338–350.

Tsai, V.C., 2009. On establishing the accuracy of noise tomography travel-time measurements in a realistic medium, *Geophys. J. Int.,* **178**(3), 1555–1564.

Tsai, V.C., 2011. Understanding the amplitudes of noise correlation measurements, *J. geophys. Res.,* **116**(B9), doi:10.1029/2011JB008483.

Tsai, V.C. & Moschetti, M.P., 2010. An explicit relationship between time-domain noise correlation and spatial autocorrelation (SPAC) results, *Geophys. J. Int.,* **182**(1), 454–460.

Udías, A., 1999. *Principles of Seismology,* Cambridge Univ. Press.

Verbeke, J., Boschi, L., Stehly, L., Kissling, E. & Michelini, A., 2012. High-resolution Rayleigh-wave velocity maps of central Europe from a dense ambient-noise data set, *Geophys. J. Int.,* **188**(3), 1173–1187.

Weaver, R., Froment, B. & Campillo, M., 2009. On the correlation of non-isotropically distributed ballistic scalar diffuse waves, *J. acoust. Soc. Am.,* **126**(4), 1817–1826.

Weemstra, C., Westra, W., Snieder, R. & Boschi, L., 2014. On estimating attenuation from the amplitude of the spectrally whitened ambient seismic field, *Geophys. J. Int.,* **197**(3), 1770–1788.

Weemstra, C., Snieder, R. & Boschi, L., 2015. On the estimation of attenuation from the ambient seismic field: inferences from distributions of isotropic point scatterers, *Geophys. J. Int.,* **203**(2), 1054–1071.

Wessel, P., Smith, W.H.F., Scharroo, R., Luis, J. & Wobbe, F., 2013. Generic mapping tools: improved version released, EOS, *Trans. Am. geophys. Un.,* **94**(45), 409–410.

Wielandt, E., 1993. Propagation and structural interpretation of non-plane waves, *Geophys. J. Int.,* **113**(1), 45–53.

Yang, Y. & Ritzwoller, M.H., 2008. Characteristics of ambient seismic noise as a source for surface wave tomography, *Geochem. Geophys. Geosyst.,* **9**(2), doi:10.1029/2007GC001814.

Yang, Y., Li, A. & Ritzwoller, M.H., 2008a. Crustal and uppermost mantle structure in southern Africa revealed from ambient noise and teleseismic tomography, *Geophys. J. Int.,* **174**(1), 235–248.

Yang, Y., Ritzwoller, M.H., Lin, F.-C., Moschetti, M. & Shapiro, N.M., 2008b. Structure of the crust and uppermost mantle beneath the western United States revealed by ambient noise and earthquake tomography, *J. geophys. Res.,* **113**(B12), doi:10.1029/2008JB005833.

Yao, H. & Van Der Hilst, R.D., 2009. Analysis of ambient noise energy distribution and phase velocity bias in ambient noise tomography, with application to SE Tibet, *Geophys. J. Int.,* **179**(2), 1113–1132.

Yao, H., van Der Hilst, R.D. & Maarten, V., 2006. Surface-wave array tomography in SE Tibet from ambient seismic noise and two-station analysis-I. Phase velocity maps, *Geophys. J. Int.,* **166**(2), 732–744.

Yao, H., Beghein, C. & Van Der Hilst, R.D., 2008. Surface wave array tomography in SE Tibet from ambient seismic noise and two-station analysis-ii. Crustal and upper-mantle structure, *Geophys. J. Int.,* **173**(1), 205–219.

Yao, H., Gouédard, P., Collins, J.A., McGuire, J.J. & van der Hilst, R.D., 2011. Structure of young East Pacific Rise lithosphere from ambient noise correlation analysis of fundamental-and higher-mode Scholte-Rayleigh waves, *C. R. Geosci.,* **343**(8), 571–583.

Yoshizawa, K. & Ekström, G., 2010. Automated multimode phase speed measurements for high-resolution regional-scale tomography: application to North America, *Geophys. J. Int.,* **183**(3), 1538–1558.

Zhou, L., Xie, J., Shen, W., Zheng, Y., Yang, Y., Shi, H. & Ritzwoller, M.H., 2012. The structure of the crust and uppermost mantle beneath South China from ambient noise and earthquake tomography, *Geophys. J. Int.,* **189**(3), 1565–1583.

Zhou, Y., Nolet, G., Dahlen, F. & Laske, G., 2006. Global upper-mantle structure from finite-frequency surface-wave tomography, *J. geophys. Res.,* **111**(B4), doi:10.1029/2005JB003677.

2.1 Concluding remarks

In this chapter, the main aspects of the ambient-noise method are presented. It is explained how the second order Bessel function J_2 has to be taken into account when measuring phase-velocities on the horizontal components, e.g. Love waves. The herein presented scheme for the automated extraction of phase-velocity curves is used to obtain the ambient-noise dataset that forms the basis for the Alpine model given in the following chapter.

The comparison between the ambient-noise and the earthquake methods shows on the one hand side that both approaches agree well and a combination of the two data sets can be used to achieve a coverage of a broader period range. This is used in the next chapter to obtain a 3-D model, which covers the Earth's crust and upper mantle down to 200 km depth. On the other hand, it provides an error estimate for both types of measurements. The synthetic tests also show how the ambient-noise measurements can be influenced by non-uniform noise source distribution, giving therefore a more detailed understanding of measurement uncertainties.

In the following chapter, an even larger data set of ambient-noise and earthquake-based two-station measurements is presented from which a set of phase-velocity maps is created. These are then used in a second inversion to create a 3-D model of the Alpine crust and upper mantle.

3 Surface-wave Tomography of the Alps using Ambient-Noise and Earthquake Phase-velocity Measurements

submitted to Journal of Geophysical Research: Solid Earth on the 12th of July, 2017

This article presents the shear-velocity models obtained from surface-wave phase-velocity measurements from ambient-noise and earthquake-based data.
In the manuscript an explanation is given of how the phase-velocity maps are created and of the following inversion for the depth structure. Data errors are discussed and resolution test for the phase-velocity maps as well as the 1-D depth profiles are presented. Thereafter, models of the crust and the upper mantle are shown and discussed. The crustal structures are compared to earlier studies from receiver functions and a Moho map is given. The mantle anomalies are presented individually for western Alps, central Alps, eastern Alps, Apennines and Dinarides. This is followed by a general discussion of subduction slabs and in relation to some of the main question formulated in sec. 1.2.3.

Surface-wave Tomography of the Alps using Ambient-Noise and Earthquake Phase-velocity Measurements

Emanuel D. Kästle[1], Amr El-Sharkawy[2,3], Lapo Boschi[1], Thomas Meier[2], Claudio Rosenberg[1], Nicolas Bellahsen[1], Luigia Cristiano[2], and Christian Weidle[2]

[1]Institut des Sciences de la Terre, Paris (ISTeP), Université Pierre et Marie Curie, Paris, France.
[2]Universität Kiel, Germany
[3]National Research Institute of Astronomy and Geophysics (NRIAG), 11421, Helwan, Cairo, Egypt.

A large data set of surface-wave phase-velocity measurements is compiled to study the structures of crust and upper mantle underneath the Alpine continental collision zone. Records from both ambient-noise and earthquake-based methods are combined to obtain a high-resolution 3-D v_S model. The applied techniques allow to image the shallow crust and sedimentary basins with a lateral resolution of 25 km. We find that our model is in good agreement with receiver-function studies in the crust, reproducing reliably the complex variations in Moho depth. It has thus the potential to serve as v_S reference model for the Alpine region. The mantle structures show nearly vertical subducting lithospheric slabs of the European and Adriatic plates. Pronounced differences between western, central and eastern Alps provide indications of the respective geodynamic evolution: relatively low velocities in the upper mantle below the southwestern Alps suggest that the European slab is detached. We propose that in the northeastern Alps, both European and Adriatic slabs are present in the upper mantle to explain the complex pattern of the imaged anomalies. A variable upper mantle structure is found beneath the Apennines with an attached Adriatic slab in the northern Apennines and a slab window in the central Apennines. There is also evidence for shallow subduction of Adriatic lithosphere to the east beneath the Pannonian Basin and the Dinarides down to a maximum depth of about 150 km.

1 Introduction

The evolution of the Alpine region is characterized by creation, subduction, and collision of rather small and mobile microplates caught between the larger Eurasian and African plates that are slowly converging since about 85 Ma (Stampfli and Borel, 2002; Handy et al., 2010). This configuration results in a high variability of subduction and collision in time and space compared e.g. to Pacific subduction zones and the Himalayan continental collision zone as evident already from the small dimensions and the strong curvature of the Alps.

Because of the absence of intermediate deep seismicity in the Alps, the slabs can only be resolved by seismic imaging. Resolving small slab segments and the highly variable crust and mantle lithosphere represents, however, a challenge. Large scale P-wave travel-time tomography shows convincing evidence for the presence of slabs beneath the Alps, in some parts down to the mantle transition zone but do not resolve details of the slab geometry (Piromallo and Morelli, 2003; Spakman and Wortel, 2004; Li et al., 2008; Koulakov et al., 2009; Giacomuzzi et al., 2011). The high-resolution model by Lippitsch et al. (2003) is obtained by local P-wave travel-time tomography with careful crustal corrections. It shows in the western-central Alps a Eurasian slab subducting steeply to the SE and a NE dipping Adriatic slab in the eastern Alps with a slab gap between these segments. Furthermore, there is evidence for horizontal slab tearing in the western Alps. The view that Adriatic and not Eurasian lithosphere is subducting in the eastern Alps has been opposed by Mitterbauer et al. (2011) essentially because high-resolution models do not include the forelands and consequently the continuation of the mantle lithosphere into the forelands has not been resolved unambiguously yet. The slab tearing in the western Alps has recently been questioned by Zhao et al. (2016).

Up to now there are no high-resolution S-wave velocity models for the Alpine region available. Because of the high sensitivity of surface waves to vertical velocity variations, their inversion for S-wave velocity models is the most promising approach to resolve properties of the mantle lithosphere and the asthenosphere. S-wave velocity models can help to constrain the composition of the lithosphere using the Vp/Vs ratio (Lombardi et al., 2008; Giacomuzzi et al., 2012) and they are very sensitive to temperature variations (Goes et al., 2000). On a larger, regional scale, S-wave velocity models are calculated by waveform inversions of surface and S-waveforms of regional and teleseismic (Legendre et al., 2012) or of regional seismic events (Zhu et al., 2012) or by inversions including surface-wave dispersion measurements (Auer et al., 2014; Meier et al., 2016).

They resolve main properties of the upper mantle in the forelands beneath Adria, central Europe, the Pannonian Basin and the Ligurian Sea but the resolution in the Alpine region remains limited. S-wave velocity models may also be determined by inversion of surface-wave phase velocities obtained from ambient-noise (AN) studies. For the Alpine region, isotropic (Verbeke et al., 2012) and anisotropic (Fry et al., 2010) phase-velocity maps have been calculated. Molinari et al. (2015) present an isotropic 3D crustal model for the Alps from AN.
Kästle et al. (2016) show, using existing data for the Alpine region, that surface-wave analyses of earthquake (EQ) data and AN are in a very good agreement in the period range between about 10 s and 35 s. AN studies can give additional information at shorter periods that means for upper crustal depths, whereas earthquake data yield information for longer periods larger than 35 s up to about 250 s and are therefore essential to resolve the mantle lithosphere, the lithosphere-asthenosphere boundary (LAB), slab segments and the asthenosphere.

The crust of the Alps has been intensively studied by active seismic soundings along several transects (EGT: Pfiffner (1992); ECORS-CROP: Hirn et al. (1987); ECORS et al. (1989); Bois and Party (1990); Roure et al. (1996); NFP20: Pfiffner et al. (1997); TRANSALP: TRANSALP Working Group et al. (2002); Lüschen et al. (2004); Bleibinhaus and Gebrande (2006); Castellarin et al. (2006); Western Alps: Thouvenot et al. (2007); Eastern Alps: Oeberseder et al. (2011)) as well as by passive local P-wave tomography (Béthoux et al., 2007; Diehl et al., 2009) and receiver-function studies (Kummerow et al., 2004; Lombardi et al., 2008; Zhao et al., 2015). The crust thickens to more than 50 km on the Eurasian side of the Alpine suture and shows a very sharp step of about 20 km across the suture towards the Adratic plate in the western and central Alps. In the eastern Alps the transition appears to be more smooth. Diehl et al. (2009) resolve lateral and vertical P-wave velocity gradients in the crust and Spada et al. (2013) the Moho topography combining passive and active methods but particularly in the eastern Alps the Moho remains poorly resolved. A comparable S-wave velocity model for the crust is not yet available. It has however been shown that Vp/Vs ratios are helpful to characterize the composition of the crust (Lombardi et al., 2008). Furthermore, receiver function and active seismic studies show that the deeper parts of the crust as well as the mantle lithosphere at sub-Moho depths possess a highly complicated structure that has not been clearly resolved yet (Thouvenot et al., 2007; Lombardi et al., 2008; Oeberseder et al., 2011; Spada et al., 2013).
Surface-wave tomography is complementary to local earthquake tomography and tele-

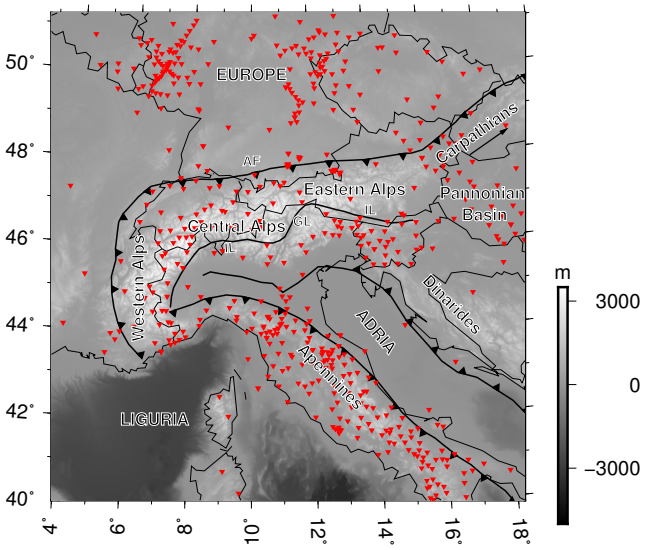

Figure 1: Map of the main tectonic units involved in the Alpine continental collision. Triangles indicate locations of stations used in this study. AF: Alpine frontal thrust, IL: Insubric line, GL: Giudicarie line. Tectonic limits from Faccenna et al. (2014).

seismic body wave tomography. The former is mainly restricted to the crust as the slabs in the Alps are essentially seismically inactive. The vertical resolution of the latter is limited in the lithosphere and asthenosphere because of nearly vertical ray paths at these depths. Because of their high sensitivity to depth variations of velocities, surface waves are well suited to study properties of the crust, the Moho depth, the mantle lithosphere, the lithosphere-asthenosphere boundary (LAB) and the asthenosphere.

In this study, we will extract fundamental mode Love- and Rayleigh-wave phase-velocity measurements to constrain the shear-velocity structure underneath the Alpine system. The limited period range of AN sources is extended by the addition of EQ-based surface-wave velocity measurements, which means that we are able to extend the measurements to longer periods and thus greater depth. The combination of the two methods allows for a better resolution than each individual method and has therefore been applied in different parts of the earth (e.g., Yang et al., 2008a,b; Köhler et al., 2012; Zhou et al., 2012; Shen et al., 2013; Ward et al., 2016). Thus augmenting the completeness of data coverage, we are able to constrain the structure of the Alpine lithosphere more robustly compared to earlier, similarly-minded studies (Verbeke et al., 2012; Stehly et al., 2009; Fry et al., 2010; Molinari et al., 2015). We can therefore provide

an alternative model for the upper mantle with respect to the body-wave studies.
We present a 3D shear-velocity model, which shows the structure of crust and upper mantle down to a depth of 200 km. We derive it from the phase-velocity maps for Love and Rayleigh waves, using a fully nonlinear direct-search algorithm (Wathelet, 2008). As the model is continuous both laterally, covering the whole Alpine chain and parts of the surrounding regions, and vertically from sedimentary basins to the upper mantle slabs, it allows to shed new light on the geometry of the colliding European and Adriatic plates.

2 Data sets

2.1 Ambient-noise measurements

We derive a phase-velocity dispersion data set for both Rayleigh and Love waves by cross correlation of AN records for station couples in central Europe. Our raw data covers the years 2007, 2008, 2012 and 2013 including a total of 313 stations. For each station couple, records are split into Z- (vertical), R- (radial) and T- (transverse) components which are correlated separately to obtain the phase-velocity dispersion for Rayleigh (from Z- and R-components) and Love waves (T-components). The cross-correlation spectra are related to the phase velocity according to Aki (1957) and the method of extracting the phase-velocity at the zero-crossings is based on the idea of Ekström et al. (2009). We use a modified scheme for which pre-processing, cross-correlation and the phase-velocity determination is explained in Kästle et al. (2016).
The data set comprises 32,874 Rayleigh Z phase-velocity curves, 25,001 for Rayleigh R and 27,090 for Love. It covers periods between 4 and 75 s, although the number of measurements reduces rapidly above 40 s (Fig. 2).

We estimate the average error of our measurements by comparing station triplets which are located on the same great-circle path (Fig. 3). For each of these triplets, we use the phase-velocity measurement from the most distant pair of stations and compare it to the weighted average of the two shorter-path measurements (Lin et al., 2008). The differences can be used as proxy for the random error in our phase-velocity estimations. We show in Figure 3 that for most of our data, the differences between long- and short-path measurements is around 0.05 km/s. The deviations increase towards longer and shorter periods. For distances between 150 and 1200 km, a trend can be observed which indicates that short inter-station distances give more reliable phase-velocity estimations at short periods and vice-versa.

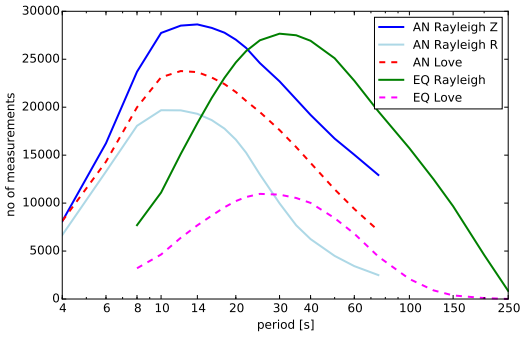

Figure 2: Number of measurements for the ambient-noise (AN) and the earthquake (EQ) two-station methods. Z and R refer to the component on which the phase velocity has been measured with the AN data.

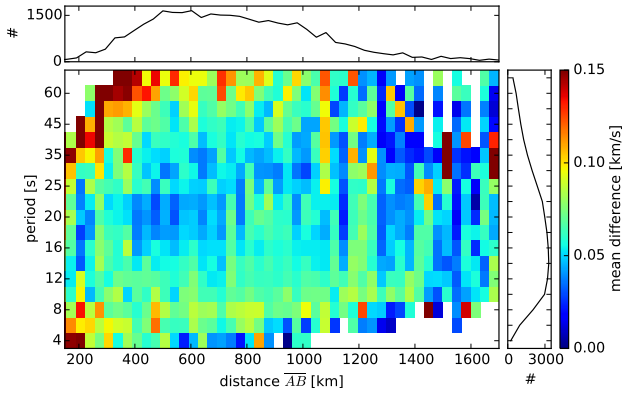

Figure 3: Estimation of measurement uncertainty of AN Rayleigh records by comparison of station triplets. We compare the phase-velocity measurements between three stations (A, B, C) along the same great-circle path. The difference in velocity between the outer stations (AB) and the path-weighted average phase-velocity of the two shorter paths (AC and CB) is shown. We define that the great-circle deviation of the third station (C) must not be greater than 0.1°. This gives approximately 5000 station triplets for the Rayleigh-wave data set.The absolute differences between long and short path measurements are binned and averaged according the the period and distance of the long-path measurement. The curves at both sides of the plot give the number of measurements (#) used in this analysis.

Using the station triplets, we can also estimate the average standard deviation of our Rayleigh-wave measurements: it is about 0.06 km/s at 25 s and increases to 0.08 km/s towards very short (<8 s) and long periods (>50 s). The same applies for Love waves, however, the standard deviation increases to higher values (0.1 km/s) towards both ends of the period spectrum.
This kind of misfit estimation takes potential errors from a biased source distribution or heterogeneous media only partially into account. A biased source distribution will affect both long and short path measurements, however, the magnitude of the error is reduced with increasing inter-station distance.

2.2 Earthquake two-station measurements

The Two-Station Method for measuring surface-wave phase velocity is based on using earthquakes as signal sources (e.g., Sato, 1955; Kovach, 1978; Meier et al., 2004; Soomro et al., 2016). An automated algorithm for inter-station phase velocity measurements (Soomro et al., 2016) is applied to a large data set to obtain the fundamental-mode Rayleigh and Love phase velocities. We utilize a database consisting of more than 3000 seismic regional and teleseismic events in the time period 1990 – 2015 and recorded by 387 broadband seismic stations distributed within and around the greater Alpine region and provided by the European Integrated Data Archive (WebDc/EIDA) and IRIS (Fig. 1). For each station pair, approximately located on the same great circle path or within 7° of off path propagation, the recorded waveforms are cross correlated and the dispersion curves of fundamental modes are calculated from the phase of the cross-correlation functions weighted in the time-frequency plane (Meier et al., 2004). The cross-correlation function is filtered with a set of frequency-dependent Gaussian band-pass filters and windowed in the time domain to minimize the effects from other signals. The automated selection of acceptable phase-velocity measurements for each event is performed in the frequency domain based on a number of fine-tuned quality criteria including the difference to a 3D path-specific reference model, smoothness and the length of the selected dispersion curves (Soomro et al., 2016). To suppress the errors due to the influence of lateral heterogeneity and off-path propagation, rejection of the perturbed inter-station phase velocity measurements and the averaging of many single-event measurements from both propagation directions are applied. Between 5 and 2500 single-event dispersion measurements are averaged for the inter-station paths in order to obtain unique, robust, more accurate broad-band dispersion curve representing the area of the Earth's structure between the considered two stations with uncertainty estimates.

In total, around 16,000 Rayleigh- and 14,000 Love-wave dispersion curves in the period range (8 - 250 seconds) have been determined, with a standard deviations lower than 2 per cent and standard errors lower than 0.6 percent.
A detailed comparison between the phase-velocity measurements obtained from this method and the above mentioned AN method is given in Kästle et al. (2016). Dispersion measurements from both processing techniques are overall in very good agreement. At periods around about 30 s there is a slight discrepancy between ambient noise and earthquake measurements with the latter being a bit faster ($0.05 km/s$). This may result either from stronger sensitivity of earthquake data to scattering especially from Moho topography or from lower resolution of the zero-crossing method to measure phase velocities from ambient noise at lower frequencies.

2.3 Earthquake-station measurements

We add the global surface-wave phase-velocity data set of from Ekström (2011), which includes first order structures in central Europe between 22 and 250 s period and provides a good background model. These earthquake-station measurements have the least influence on the phase-velocity maps, but complete the presented model in regions where otherwise no measurements from the two-station methods are available.

3 Model creation

3.1 Phase-Velocity Maps

We jointly invert dispersion measurements from the three mentioned data sets to derive phase-velocity maps (e.g., Boschi and Dziewonski, 1999) at different periods. The AN dispersion curves are smoothed before inversion by fitting a fifth order polynomial to the data. This is justified by the fact that jumps in the dispersion curves are unrealistic given the depth averaging properties of the surface-wave dispersion. These jumps are caused by noise in the cross-correlation spectra and errors in the automated picking of the curves. The EQ two-station method provides smooth phase-velocity curves by averaging over two-station measurements from several events; very noisy data or data where forward and backward measurements (phase velocity for a wave traveling from station one to station two and vice versa) differ strongly are furthermore rejected (Soomro et al., 2016).

The study region is subdivided in a 0.1 x 0.1 (great-circle) degree raster, which is the same for all periods and for both Love and Rayleigh waves. We use a ray-theoretical approach for the signal propagation between each station couple along a great-circle path. This will introduce errors from finite frequency effects and multipathing, which, however, we expect to be small based, e.g., on Boschi (2006). The inversion is based on an iterative, linear least-squares algorithm (LSQR, Paige and Saunders, 1982). It is regularized according to the criteria of Boschi and Dziewonski (1999); we use only roughness damping and no norm damping. We increase roughness damping with period to account for the structural averaging properties of long period waves, so that mapped structures should not smaller than half a wavelength. Additionally, we tuned the damping parameters to show a maximum of consistency with known geological structures.

The Love- and Rayleigh-wave data sets for AN R- and Z-component are inverted jointly with the EQ measurements. Different weights are attributed to the data sets, so that the AN R-component measurements are weighted lower than the Z-component ones, because of the difference in data quality. EQ two-station measurements are weighted higher, so that for Rayleigh waves, the relative weights are 0.8, 1.0, 1.5 and 5 for AN R-component, AN Z-component, EQ two-station and EQ single station measurements, respectively. More important for the influence on the phase-velocity maps are, however, the number of data and the path coverage, so that the single station measurements show the least influence on the mapped structures despite the larger weight. In case of Love waves, the weights are 1, 1 and 5 for AN, EQ two-station and EQ single-station measurements, respectively (Fig. 5).

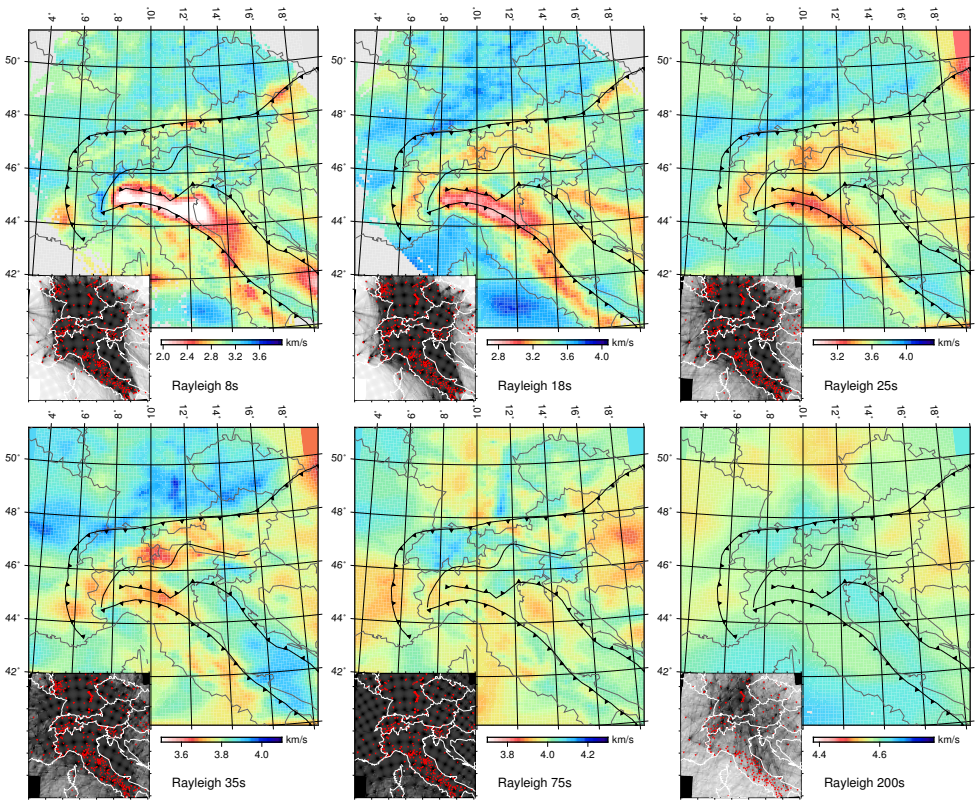

Figure 4: Rayleigh wave phase-velocity maps at different periods. Blocks where less than 3 rays are passing are grayed out. The smaller map shows the path coverage for each block of the inversion raster.

For each phase-velocity map we determine the misfits between our data and the model predictions and calculate the misfit standard deviation. We discard data with misfits larger than three times the standard deviation as outliers, which is about 2% of the data, both for Love and Rayleigh waves. The inversion procedure is then repeated to obtain our final maps (Fig. 4 and 5).

3.2 Resolution of phase-velocity maps

We perform checkerboard resolution tests for the Rayleigh phase-velocity maps with block sizes of 2 and 0.5 degrees (Fig. 6). We add random Gaussian noise with a standard deviation of 0.1 km/s to the synthetic data. This value is taken as high-noise proxy (see sec. 2). Due to the very good ray path coverage, the blocks are reproduced accurately

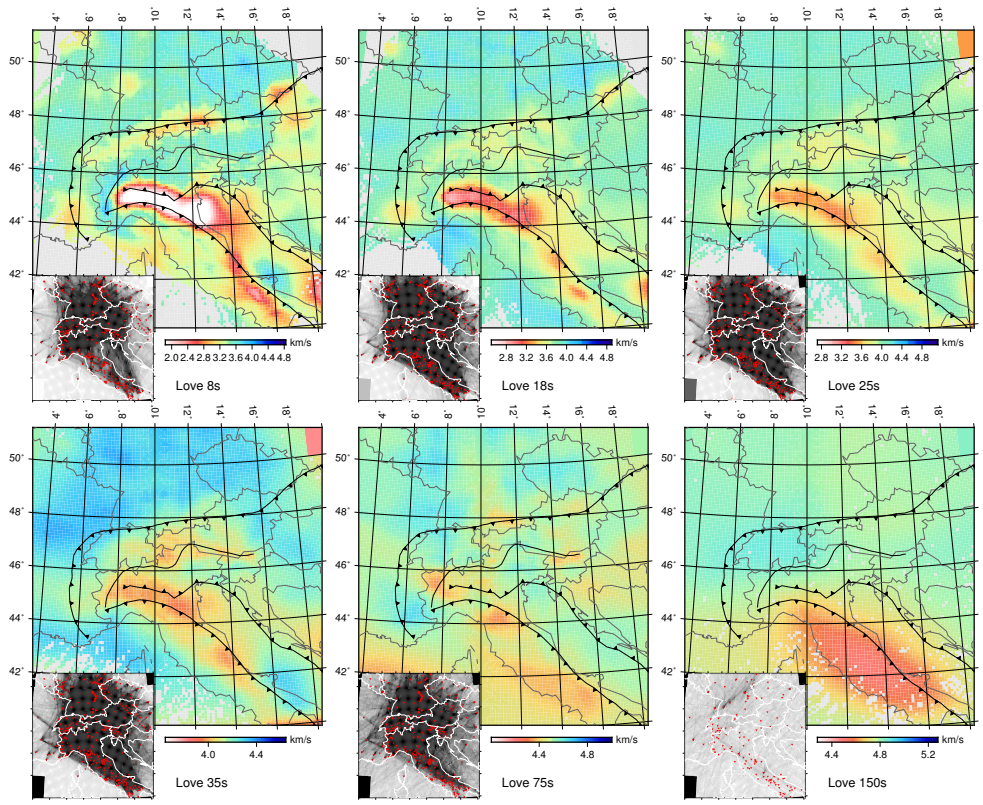

Figure 5: Love wave phase-velocity maps at different periods. Blocks where less than 3 rays are passing are grayed out. The smaller map shows the path coverage for each block of the inversion raster.

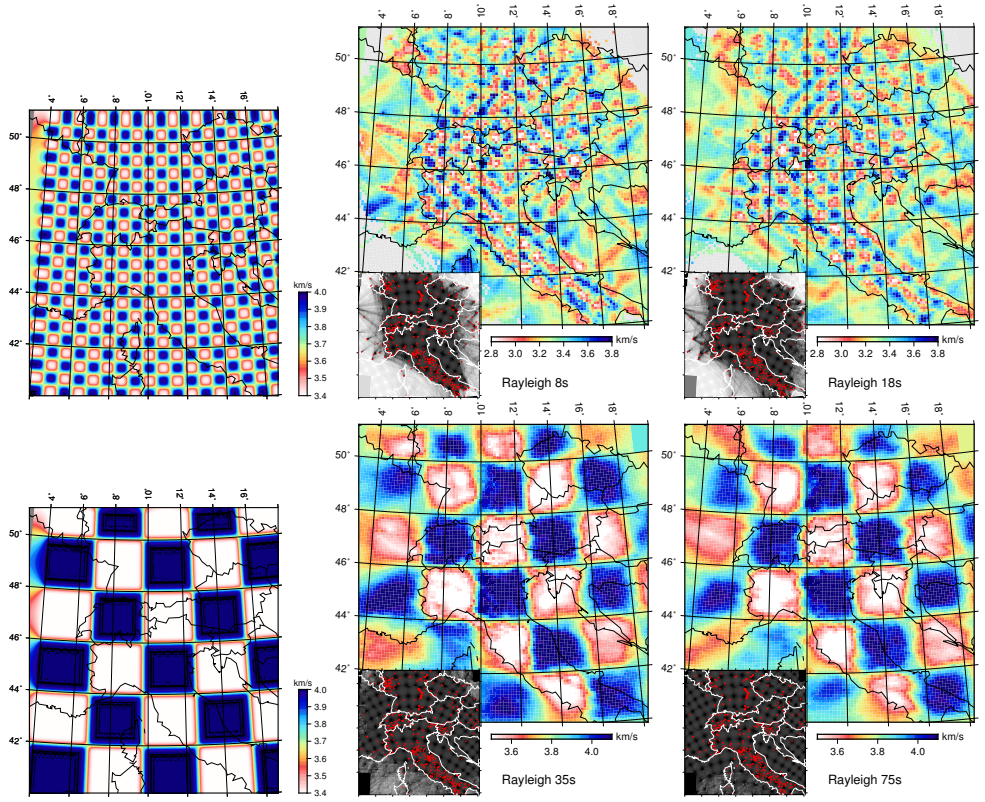

Figure 6: Checkerboard test for the Rayleigh phase-velocity maps. The top panel shows an input model with 0.2° structure size. The recovered maps at 8 and 18 s are shown next to it, where noise with 0.1 km/s standard deviation has been added to the synthetic data. The smaller maps at the bottom of each figure show the path coverage for each block. The bottom panel shows the same for a 2° checkerboard model at 35 and 75 s

in the central regions of the model, showing the highest resolution in Switzerland and northwestern Italy. We are especially interested in the orogenic structures which are all in the high-resolution areas of our model apart from the southern Dinarides and beginning Carpathians (compare Fig. 1). Some lateral smearing is expected in the southern Apennines and the eastern limits of the eastern Alps.

3.3 Depth Structure Inversion

At each cell of the phase-velocity map, we extract a dispersion curve for Rayleigh and Love waves, ranging from 4 to 250 s. We then use the neighborhood algorithm (Sambridge, 1999; Wathelet, 2008), a stochastic direct search, to find the best-fitting layered

model for P- and S-wave velocity (v_P, v_S). The model search is performed by choosing randomly 8000 starting models from the solution space and calculating phase-velocity dispersion curves for each of these models. For each model, a misfit estimate is calculated where we weight the Rayleigh-wave misfit slightly higher than the Love-wave misfit (1 vs. 0.8). The reason for this is the larger amount of Rayleigh-wave data and the lower measurement error (see sec. 2). The algorithm then continues to generate 200 new models in the parameter regions with the lowest misfit, which is repeated during 100 iterations giving a total of 28,000 models.

The relative misfit of one modeled dispersion curve to the observed Rayleigh- and Love-wave velocity measurements is estimated according to Eq. (3.38) of Wathelet (2005):

$$misfit = \sqrt{\sum_{i=1}^{n_F} \frac{(x_{di} - x_{ci})^2}{x_{di}^2 n_F}}, \tag{1}$$

where n_F is the number of samples of the dispersion curve, x_{di} the data value of the ith sample and x_{ci} the computed value. A misfit value of 0.03 would therefore correspond to 3% misfit between measured and modeled dispersion curve. The dispersion curves are sampled at an approximately logarithmic scale between 4 and 250 s, putting equal weights on short and long periods.

The model space is limited by giving a set of boundary conditions summarized in table 1. We use a 8-layer model over an homogeneous half space. The range of possible values for the upper three layers are chosen to represent approximately a sedimentary layer, upper and lower crust. The three underlying mantle layers all have the same boundary values for v_P and v_S. No density inversion is performed as its influence on the phase-velocity dispersion is very low (Wathelet, 2005). No continuity between layers is required, so that both jumps to higher and lower velocities between layers are possible. The organization of the mantle layers follows loosely PREM, e.g. by having a boundary around 220 km depth (Dziewonski and Anderson, 1981). The thickness of the crustal layer is determined by the model search. After the algorithm has obtained a first guess on the crustal thickness, the thicknesses of the mantle layers are fixed following two requirements: increasing layer thickness with depth and a boundary around 220 km depth (Tab. 1).

Within each of the seven top-layers a linear velocity gradient is imposed, obtained by subdivision into five sub-layers. In order to limit the number of free parameters and thus stabilize the inversion, we only allow positive velocity increments within the crustal layers. A negative velocity jump between layers is nevertheless possible. In the upper mantle layers, between the Moho discontinuity and 220 km depth, we allow also for

Table 1: Boundary conditions used in the stochastic model search. In the last mantle layer and the half space, the velocities have no gradient within the layer.

Layer	bottom depth $[km]$	v_P $[km/s]$	v_S $[km/s]$	density $[g/cm^3]$	velocity gradient
sedimentary layer	0.1 – 12	1.6 – 6.8	0.8 – 3.0	2.400	linear increase
upper crust	5 – 50	5.0 – 7.2	2.8 – 4.3	2.750	linear increase
lower crust	10 – 95	6.0 – 7.2	3.5 – 4.2	2.900	linear increase
mantle layer 1	65 – 120	7.36 – 8.6	4.2 – 4.95	3.370	linear
mantle layer 2	130 – 170	7.36 – 8.6	4.2 – 4.95	3.375	linear
mantle layer 3	200 – 240	7.36 – 8.6	4.2 – 4.95	3.380	linear
mantle layer 4	270 – 310	7.5 – 9.6	4.4 – 5.2	3.481	linear
mantle layer 5	370 – 410	7.5 – 9.6	4.4 – 5.2	3.485	uniform
half space		8.8 – 12.0	4.6 – 6.5	3.800	uniform

linear decreasing velocities, to be able to image the structure of lithospheric subduction slabs (Tab. 1).

The size of the depth sensitivity kernel of surface-waves increases with period, which influences the resolution of our model with increasing depth. By inverting Love and Rayleigh waves jointly, we improve the resolution, as the two wave types have different sensitivity kernels.

In the following we will only discuss v_S profiles as v_S is the best constrained parameter by Love- and Rayleigh-wave phase-velocity dispersion (Wathelet, 2005). Our final model is obtained by calculating the average thickness and shear velocity for each layer of the 500 models with the lowest misfit. We therefore keep the sharp boundaries between layers, which is especially useful in order to interpret the Moho depth.

The applied model search is based on a simplified approach for purely isotropic layers, which is an approximation especially in the upper mantle where we expect pronounced radial anisotropy (Dziewonski and Anderson, 1981). The resulting isotropic 1-D model will therefore not exactly match Rayleigh- and Love-wave dispersion curves at the same time in the presence of radial anisotropy. We test for this effect by additionally performing separate model searches for Rayleigh and Love measurements. Rayleigh waves are mostly sensitive to v_{SV} and Love waves to v_{SH} (Muyzert and Snieder, 2000). By comparing the Voigt-average (Babuska and Cara, 1991) of the resulting profiles with the joint inversion, we test whether our simplified approach introduces significant errors. We find that the imaged structures in the mantle only show minor differences and we con-

clude that the errors from neglecting radial anisotropy are not influencing the presented interpretations of the slab geometries.

3.4 Depth Resolution Tests

We test the resolution capacities of the neighborhood search algorithm by creating synthetic dispersion curves for Love- and Rayleigh-waves from a simple model. In Figure 7 we show different models with sedimentary basin, crust with increasing velocity and underlying mantle following PREM (Dziewonski and Anderson, 1981) apart from one smooth velocity anomaly. The anomaly has a always a peak of $\pm 4\%$ dv_S with respect to PREM. A random error with standard deviation of 0.1 km/s is added to the synethetic dispersion curves.

For each synthetic structural model in Figure 7, we calculate the Love- and Rayleigh-wave phase velocity and start a model search with the parameterization shown in Table 1. The range of tested models is shown as well as the final model, given by the layer-average of the 500 lowest misfit models. The uncertainty of the Moho depth estimation can be seen from the dashed lines in the profiles in Figure 7, which show the standard deviation range from the 500 best-fitting models. It becomes clear that the method is most sensitive to the shallow structure as small deviations in the upper 10 km result in very high misfits. Due to the high sensitivity and good resolution of short period waves, sedimentary basins and shallow crust are well constrained. Very complex crustal structures as in Figure 7f can not be uniquely resolved, which is caused by the decreasing resolution with depth and the non-uniqueness of the inverse problem.
The mean Moho depth shows an error of less than 2 km for the "simple" input models with strong contrast between crust and mantle velocities (Fig. 7a,b). The tests show also that the resolution for a shallow Moho is much higher (Fig. 7e). The depth uncertainty of the Moho is higher in the case of reduced velocities in the mantle, therefore reducing the crust-mantle contrast (compare Fig. 7a and c). The Moho depth is not well resolvable in case of the high-velocity anomaly in the crust in Figure 7f.
All mantle anomalies down to 220 km are recognized by the algorithm in their tendency (positive/negative velocity anomaly with respect to PREM). The peak amplitude is, however, always underestimated. Deeper (Fig. 7b and f) and/or narrower (Fig. 7d and e) anomalies are reconstructed with a larger error. The underestimation of the anomaly seems to cause some leakage into other depth ranges. This is, for example, visible in Figure 7b where the reconstructed velocities underneath the anomaly are too high. The shear velocity below 220 km tends furthermore to be overestimated in several of the

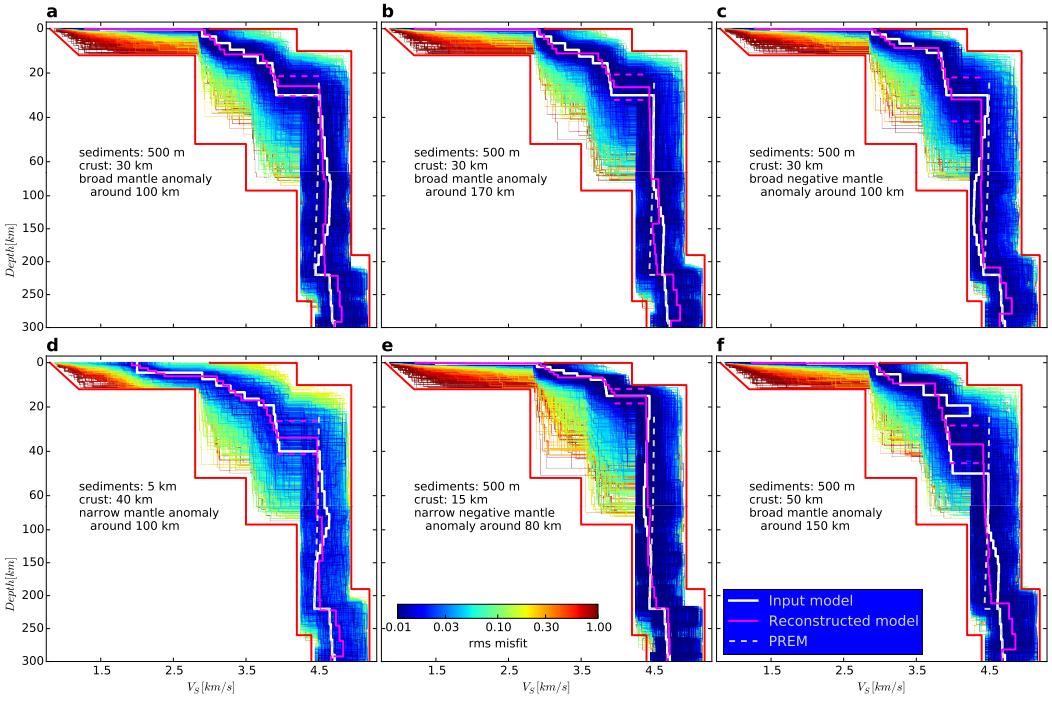

Figure 7: Tests showing the depth resolution of the applied method. Six different synthetic input models are compared to the recovered average of the 500 best-fitting models. The range of tested models is shown as color coded lines according to their misfit. Red boundaries give the limiting values for the model search from Table 1. Dashed pink lines show the uncertainty in the recovered Moho depth by giving the standard deviation.

presented models.

3.5 Model Misfit

We compare the dispersion curves from our measurements to the ones corresponding to the best-fitting shear-velocity structure from the model search. The maps presented in Figure 8 give the relative misfit according to Eq. 1. Regions of higher misfit tend to correspond to the thick sedimentary basins, e.g. in the Po-plain in northern Italy or in the southeasternmost corner of Germany. This is caused by the more complex structure which is not perfectly reproduced by the simplified model and also the higher standard deviation of the measurements at very high frequency. The higher standard deviation by potentially erroneous measurements can be seen in the high-frequency data in Figure 8 at location *D* (compare also sec. *Data*). Additionally, the velocities from Love and Rayleigh waves are often not perfectly matched by a single shear-velocity model: in most cases, Rayleigh data is slightly slower than the model while Love wave data is faster (Fig. 8). This could be an effect of anisotropy.

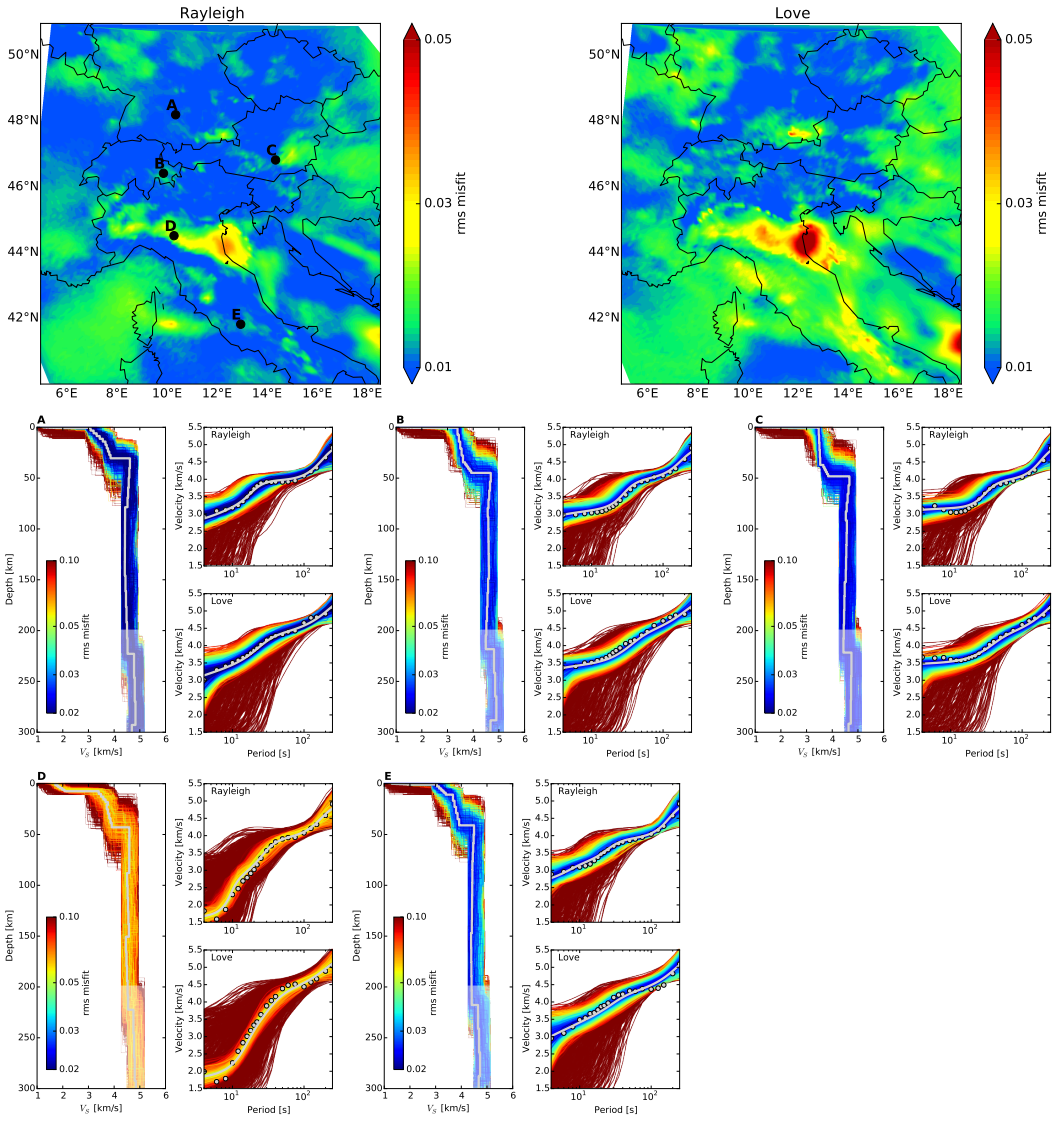

Figure 8: Maps show the relative misfit between the measured and modeled phase-velocity curves, averaged over all periods. The labeled points in the map correspond to individual phase-velocity curves shown below. Each panel shows the shear-velocity models resulting from the model search and their corresponding misfit. The preferred model (grey) is the average of the 500 models with the lowest misfit. The corresponding dispersion curves for Love and Rayleigh waves are shown next to it. Grey dots show the data as extracted from the phase-velocity maps.

4 Shear-velocity structure of the Alps

4.1 Crustal structure

The individual solutions for all points of the raster give a 3-D structural model of the crust and mantle underlying the Alpine orogenic system. No smoothing is applied to the images so that each pixel in Figure 9 relates to one independent 1-D profile. Each of these profiles represents an average of the 500 best models that result from the model search (see section *Depth structure inversion*).
In Figure 9 we present the crustal structure from our model at different depth levels and in a set of cross-sections. The shear-velocity maps show the orogenic roots of Alps, Apennines and Dinarides with reduced velocity in the crust (20 km map, Fig. 9) and elevated crustal thickness (40 km map, Fig. 9). Also the sedimentary basins can be identified in southern Germany and the Italian Po plain. The northern Alpine Molasse basin follows almost continuously the Alpine front from the Mediterranean to the Carpathians (compare also maps in Fig. 4 and 5). From our model, its average depth is of 1 km in Switzerland and southern Germany and increases to 5 km in the southeastern corner of Germany. Previously reported results give a higher thickness in the Swiss Molasses basin (3.5 km), but agree well with the sedimentary thickness in southeastern Germany (4.5 km) (Consiglio Nazionale Delle Ricerche, 1983). The cross-sections show the wedge-like shape of the Po sedimentary basin in Italy with increasing thickness towards the south-east. The average thickness of the slow structure in our model is approximately 5 km and increases to 11 km towards the south and east. Increasing sedimentary thickness towards the south and maximum thicknesses of 3.5–9 km are also shown in the geologic map by Consiglio Nazionale Delle Ricerche (1983).

The crustal sections presented in Figure 9 include the Moho estimates of Spada et al. (2013), derived from receiver functions and controlled-source studies (CSS). The Moho depth in our model is defined by the inversion parameterization as the 4.2 km/s velocity limit (Tab. 1). A good match, showing discrepancies of less than 5 km, is observed for the Moho depth of the European plate. In the model of Spada et al. (2013) the Adriatic Moho depth decreases to 10 km above the Ivrea body, a geophysical anomaly due to the presence of mantle material in the shallow crust above the underthrusting European plate (e.g. Schmid and Kissling, 2000) (profiles A–C between 250 and 400 km in Figure 9). The Ivrea body is represented in our model by anomalously high velocities between 0 and 25 km depth in profiles A–C. The mapped velocity anomaly is likely to be reduced in amplitude compared to the actual anomaly: according to the tests in Figure 7f, the

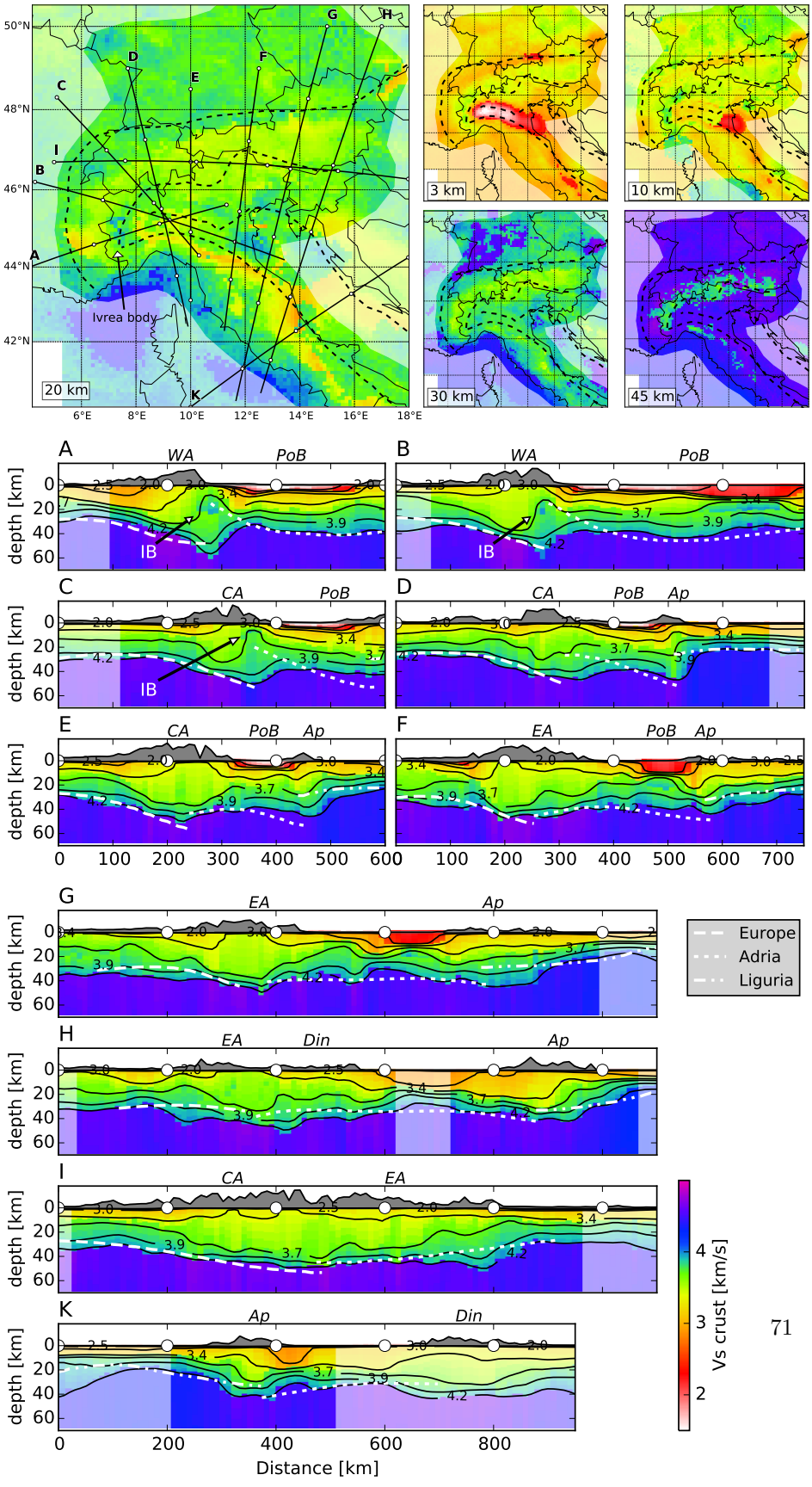
50°N
48°N
46°N
44°N
42°N
6°E
8°E
10°E
12°E
14°E
16°E
18°E
A
B
C
D
E
F
G
H
I
K
Ivrea body
20 km
3 km
10 km
30 km
45 km
depth [km]
WA
PoB
CA
Ap
EA
Din
IB
Distance [km]
Europe
Adria
Liguria
Vs crust [km/s]

Figure 9: Crustal structure in map view and along 10 different cross-sections. Each column in the cross-sections represents the average of the 500 lowest misfit models from the model search. For an explanation of the dashed limits in the maps refer to Figure 1. Moho boundary lines in the cross sections for European, Ligurian and Adriatic plate are taken from the receiver-function and CSS study of Spada et al. (2013). IB marks the position of the Ivrea body. Regions of lower resolution are shown with reduced color intensities, according to the resolution tests in Figure 6. The abbreviations on top of each section refer to the topography: Ap: Apennines; CA: Central Alps; Din: Dinarides; EA: Eastern Alps; PoB: Po sedimentary basin; WA: Western Alps. The depth scale in the cross sections is exaggerated by a factor of two.

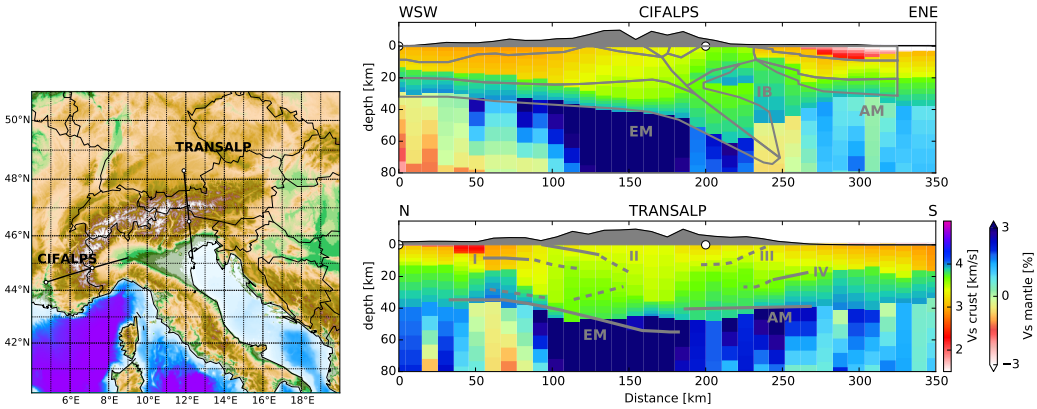

Figure 10: Comparison between the interpreted structures in the CIFALPS cross-section from Zhao et al. (2015) and the TRANSALP cross-section from Kummerow et al. (2004) to our surface-wave model. Mantle anomalies are shown as Voigt-averaged (Babuska and Cara, 1991) PREM deviations (Dziewonski and Anderson, 1981). The study of Zhao et al. (2015) is based on receiver-functions; Kummerow et al. (2004) combine receiver-function and reflection-seismic experiments. EM: European Moho; AM: Adriatic Moho; IB: Ivrea Body; I: Base of Mesozoic sediments; II: Sub-Tauern ramp; III: Sub-Dolomites ramp; IV: Adriatic crust interface. Please see respective publications for more detailed explanations of the shown interfaces.

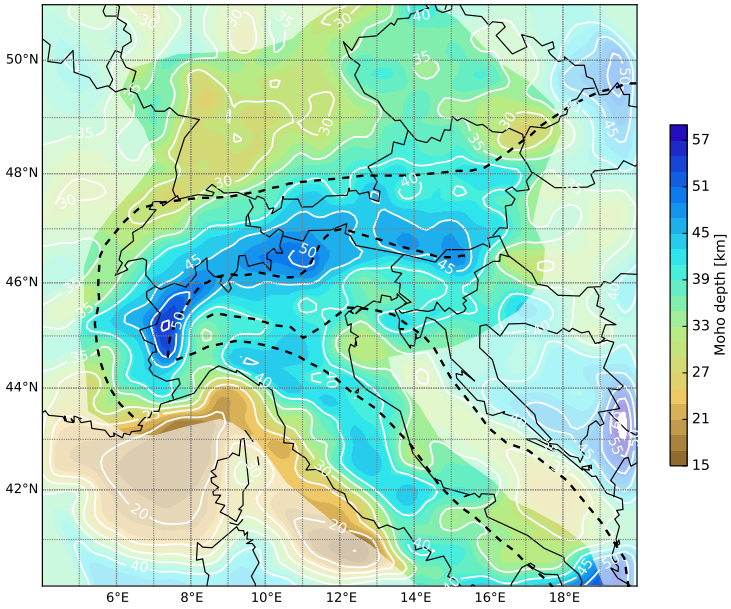

Figure 11: Moho depth map. The Moho depth is defined as average crustal thickness of the 500 best-fitting models (compare sec. 3.3). Regions of lower resolution are shown with reduced color intensities, according to the resolution tests in Figure 6.

applied inversion underestimates the strength of a fast and shallow crustal anomaly. Our models suggest that the Ivrea body is a rather continuous structure that follows the Insubric line from the junction with the Apenninic front in the south to 46°N. Its imaged size is therefore consistent with that inferred from previous studies of Schmid and Kissling (2000) or Diehl et al. (2009). The northernmost part of this fast anomaly is also spatially related to the Ticino gravity anomaly described by Kissling (1984).
The greatest crustal thickness is observed in profile A at the edge of the downgoing European plate. In combination with the fast Ivrea body signature on top of it, this could indicate underthrusting below the collisional wedge down to 60 km. This conclusion corroborates previous results based on receiver functions from a dense station profile (Zhao et al., 2015), showing that parts of the European crust may reach 80 km depth, overlain by the Ivrea body (Fig. 10). The maximal Moho depth of 60 km in our model may also be an expression of onsetting eclogitization of the root of the collisional wedge, which would increase seismic velocities and is expected to occur at a depth of 55–60 km in the Central Alps according to Bousquet et al. (1997). The Moho depth estimation in our model may furthermore be influenced by the complex crustal structure for which the synthetic tests suggest an underestimation of the crustal thickness (Fig. 7f). The crust may therefore extend even below 60 km in the Western Alpine collision zone.
The differences in Moho depth between our model and the one of Zhao et al. (2015) are of approximately 2 km for the European and 5 km for the Adriatic plate (Fig. 10). We initially did not expect our surface-wave model to reproduce weak velocity jumps within the crust, as the surface-wave data are much better suited to constrain the average v_S-structure than specific boundaries. However, our estimates of the depth of the sedimentary layer and of the upper crust agree well with receiver function results along the CIFALPS profile (Fig. 10). A similar conclusion can be drawn from the TRANSALP comparison, also shown in Figure 10: the nappes contacts are only approximately reproduced in our model, but the Moho depth is in good agreement with that derived from receiver functions, with a maximum error of 8 km in the inferred area of the plate interface.

The Moho depth map in Figure 11 shows a shallow Moho especially in the Ligurian sea, in agreement with the young age of oceanic crust there (e.g., Handy et al., 2010). Moho depths of 28 km along the Rhine-graben at 8°E, north of the Alps, are comparable to the results of previous studies, and can be related to crustal thinning (e.g., Ziegler et al., 2004). The areas of greatest Moho thickness are related to the plate boundaries. The inferred plate limit in the Alps is thus closely confined to a zone just north of

the Periadriatic line. In the western Alps, the European Moho depth increases more gradually than the Adriatic one, indicating subduction of the European plate. In the central and eastern Alps the Moho topography is more symmetric.

4.2 Mantle structure

We show in Figure 12 the shear-velocity structure down to 200 km depth. We smooth the mantle structure both vertically and horizontally, in order to make the structures easier to interpret, which would otherwise be influenced by velocity fluctuations that are below our resolution limit (Fig. 7). Stronger smoothing is applied to deeper structures, in order to account for the fact that the depth sensitivity of surface waves is controlled by period (i.e., its wavelength).

A clear distinction between regions of significantly elevated shear velocity and regions of reduced velocities, most importantly the Ligurian plate, the Pannonian basin and large parts of Germany, becomes evident in our maps of the mantle. At depth above 100 km, the moderate fast anomalies are mainly due to cold continental lithosphere, while the strongest anomalies tend to follow the tectonic boundaries and are therefore interpreted as lithospheric subduction under the orogens that in most places continues into deeper parts of the mantle.

Slow velocities in the Ligurian plate can be explained by its oceanic origin and young age: rollback subduction of the Ligurian oceanic plate along the Liguria-Adria plate boundary began 30 Ma ago and led to significant extension in the western Mediterranean (e.g., Handy et al., 2010). In the Pannonian basin, upwelling of the asthenosphere can explain the reduced velocities. A slab break-off of the eastward subducting Adriatic plate that started 35 Ma ago gave rise to hot mantle material and volcanic activity (Handy et al., 2015). Lower velocities in the shallow mantle underneath Germany are also found by earlier studies (e.g. Koulakov et al., 2009) and are explained in terms of a shallower-than-average lithosphere-asthenosphere boundary and reduced velocities in the lithosphere (Geissler et al., 2010; Seiberlich et al., 2013; Meier et al., 2016).

Western Alps

A pronounced fast mantle anomaly is visible in cross-sections A and B of Figure 12 underneath the European plate, between the Moho and 80 – 100 km depth. A secondary moderate fast mantle structure at depth greater than 100 km extends along the same profiles in the distance range 300 – 600 km. The two anomalies are separated by a narrow low velocity structure, especially visible in profile B, which follows approximately the Insubric line (Fig. 12, compare also 100 km depth map).

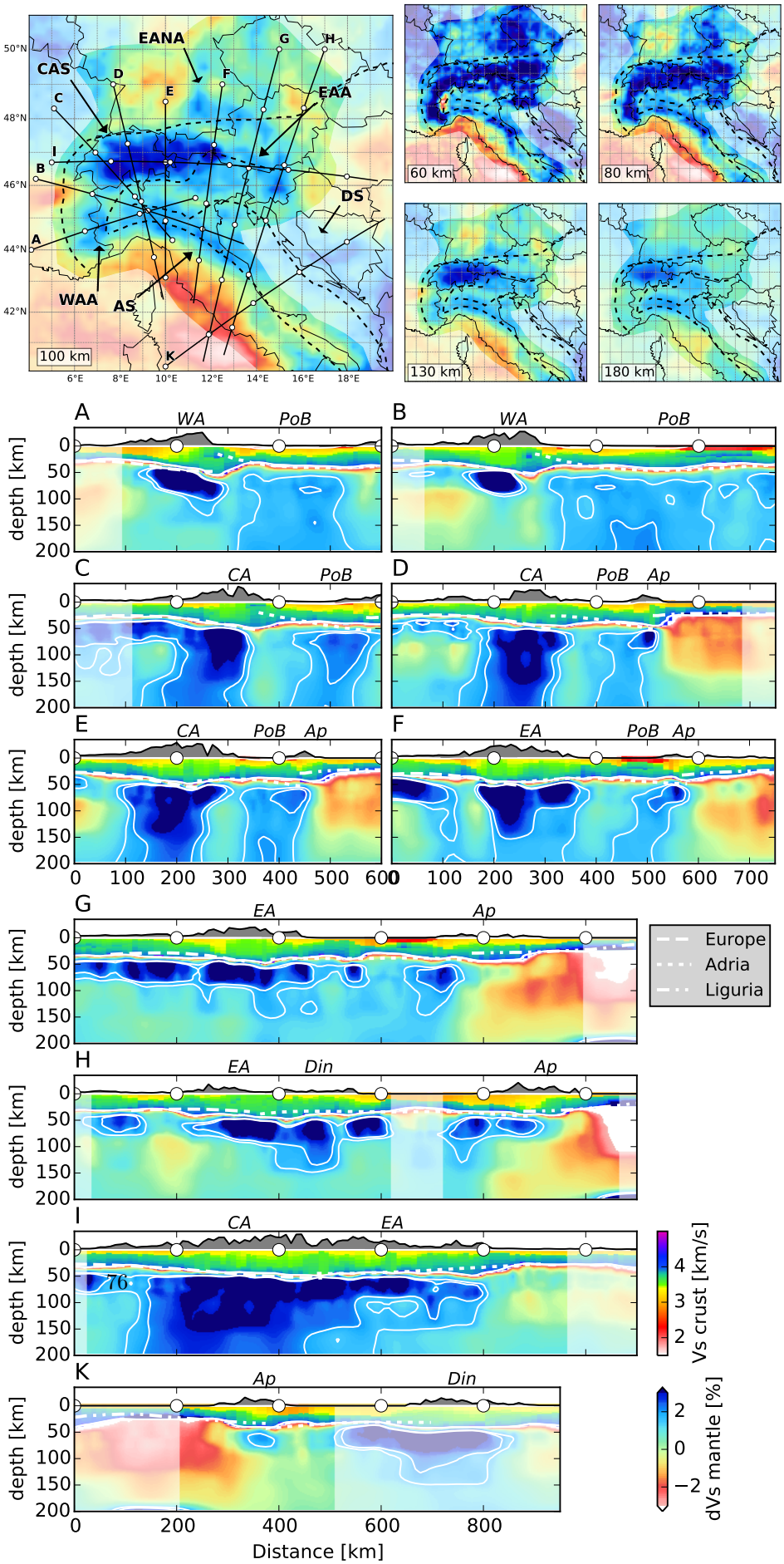
EANA
CAS
EAA
DS
WAA
AS
A
B
C
D
E
F
G
H
I
K
100 km
60 km
80 km
130 km
180 km
50°N
48°N
46°N
44°N
42°N
6°E
8°E
10°E
12°E
14°E
16°E
18°E
WA
PoB
CA
Ap
EA
Din
depth [km]
Distance [km]
Europe
Adria
Liguria
Vs crust [km/s]
dVs mantle [%]
76

Figure 12: Mantle structure in map view and along 10 different cross-sections as shear-velocity deviations from PREM (Dziewonski and Anderson, 1981). For an explanation of the dashed limits in the maps refer to Figure 1. Moho boundary lines in the cross sections for European, Ligurian and Adriatic plate are taken from the receiver-function and CSS study of Spada et al. (2013). Regions of lower resolution are shown with reduced color intensities, according to the resolution tests in Figure 6. The +1.5% and +2.0% contour lines are shown to emphasize the slab anomalies. WAA: western Alpine anomaly; CAS: central Alpine slab; EANA: eastern Alpine northern anomaly; EAA: eastern Alpine anomaly; AS: Apenninic slab; DS: Dinaric slab. The abbreviations on top of each section refer to the topography: WA: Western Alps; CA: Central Alps; EA: Eastern Alps; Ap: Apennines; Din: Dinarides; PoB: Po sedimentary basin.

The maps of Figure 12 show that, in the shallow mantle (between 50 and 100 km), one high-velocity feature is laterally very continuous along the entire Alpine arc. At 100 km and deeper, however, the western Alpine anomaly is separated from the central Alpine one at about 46°N. The v_S anomaly is also not as pronounced and narrower compared to the central Alps.

We interpret the fast structure underneath the western Alps as European slab. The deeper mantle structure under the Po-basin in profiles A and B in Figure 12 is likely to be either part of the western Alpine slab or the Adriatic slab or a mixture of both. Zhao et al. (2016) propose that a complex interaction between eastward subducting Alpine and northwards subducting Adriatic slab results in the thick mantle anomaly under the junction between western Alps and Apennines.

Central Alps

Cross-sections C – F in Figure 12 show a 100 – 150 km thick vertical slab, which we attribute to the European lithospheric plate because it is in continuity with the European Moho. Its northern and southern limit seem to correspond to the Alpine Front and the Insubric line, respectively. It is clearly distinct from the western Alpine slab which shows no pronounced vertical continuation below 100 km. At depth below 150 km the slab seems to be slightly overturned in profiles C and D (Fig. 12). Also in the Rayleigh-wave phase-velocity map, the fast anomaly in the central Alps shifts gradually to the north with increasing period (Fig. 4). This may, however, be caused by insufficient lateral resolution of our maps at very long periods/large depths.

The thick high-velocity slab extends laterally, along the strike of the orogen to about 12.5°E, where the Insubric line steps northward along the Giudicarie line (see also Fig. 1), and continues with reduced thickness and depth extent to almost 13°E. This can also

be observed from the arc-parallel cross-section I in Figure 12 at approx. 500 km distance along the profile.

Eastern Alps

The imaged fast anomalies in the eastern Alps are more complex and do not follow a pattern that is as clearly interpretable as in the western and central Alps. They are lower in amplitude compared to the central Alps and are limited by the Pannonian basin towards the east. The main fast anomalies are located just north of the Insubric Line and connect at 15°E to the Dinaric fast anomaly. A second fast anomaly, also sub-parallel to the Insubric line is visible approx. 1° further to the north. It has its highest amplitude in southeastern Germany hence we denominate the Eastern Alpine Northern Anomaly (Fig. 12).

A thickened crust at the southern boundary of the European plate is shown in profile G (Fig. 10 and 12). However, no clear slab-like structure can be seen below this area and only a moderate increase in shear velocity is visible below 100 km depth. Downwelling of the fast anomaly in profile I at 700 km could be attributed either to the Adriatic or to the European plate.

Dinarides

Due to the limited station coverage in the Dinarides south of 45°N, our checkerboard tests indicate a far lower resolution compared to Italy and the Alpine chain (Fig. 6). The mapped structures have therefore a higher uncertainty.

Two main fast anomalies are observable in our model, separated by a very small structure of reduced velocities at 45.5°N, between 80 and 130 km depth, which may be linked to the larger Pannonian anomaly. South of 45°N, the fast anomaly follows closely the limit of the Adriatic plate with pronounced increase in shear velocity directly beneath the Moho and moderate increase below 100 km depth.

The Adriatic slab under the Dinarides appears almost vertical in our models, with a slight inclination towards the northeast. It is lower in amplitude than the slab in the central Alps but can be followed as moderate high velocity anomaly down to 150 km depth. However, we think that due to the mentioned lack of resolution of our model in this area, comparisons with the Alpine structures should be made with care.

Apennines

The Apenninic mantle north of 43°N is characterized by a fast anomaly following the Apenninic front which is itself separated by a sharp boundary from the low-velocity

Ligurian mantle (Fig. 10, maps). South of 43°N, a gap in the fast anomaly becomes evident. This gap extends southward to about 41°N. The Apenninic slab is always vertical at depth in the profiles of Figure 12, sometimes with a slight tendency of dipping in the opposite direction of the inferred subduction direction (Fig. 12, profile C and profile K).

5 Discussion

The structures in the presented model are clearest under the central Alps, where the fast, vertical anomaly reaches down to the bottom of our model at 200 km depth. Before the continental collision started in the Alps at 35 Ma, Adria acted as upper plate and Europe was subducted. It has been proposed that the central Alpine slab steepened with the beginning continental collision (Kissling, 2008; Singer et al., 2014): the convergence rate reduced while the slab-pull remained strong, therefore steepening the slab and finally causing a break-off of the oceanic slab fragment, after which the slab retreat (rollback) continued at very low rate. This would explain the very steep geometry of the slab shown in our model. There is no indication of an oceanic slab break-off in the top 200 km, which is in agreement with body-wave tomographic images (Lippitsch et al., 2003; Koulakov et al., 2009; Mitterbauer et al., 2011; Zhao et al., 2016). The post-collisional shortening in the central Alps is of the order of 160 km (Schmid and Kissling, 2000), meaning that such a break-off would be at the bottom or even below our model limit. The area showing the continuous central Alpine slab is limited towards the west at 46°N and towards the east at 12°E, close to the Guidicarie line (Fig. 12). The spatial correlation of the eastward termination of the slab and the Giudicarie line has also been observed in the tomographic model of Zhao et al. (2016) and is similar to the modeled structures by Mitterbauer et al. (2011). The pronounced difference in anomaly strengths indicates a different evolution of the central Alpine subduction compared to western and eastern Alps.

The low velocities in our images beneath the western Alps under the Ivrea zone point to a shallow (below 100 km) slab break-off (Fig. 12, sections A, B). The detached part of the slab could cause the fast anomaly in profiles A and B below 100 km underneath the Po basin but may equally correspond to the Adriatic slab (Fig. 12). The model by Lippitsch et al. (2003) also supports the hypothesis of a slab break-off under the western Alps: they image a slab sitting between 150 and 350 km depth, separated from the European lithosphere above by low velocities. This contradicts the results of Zhao et al. (2016), who find a thin (50 km) slab linking the deeper anomaly with the lithosphere.

Such a thin link at 100 km depth is at the resolution limit of our model (Fig. 7d) but is unlikely given the low velocity structure in our model which terminates the shallow slab under the western Alps.
From the difference between central and eastern Alpine anomaly, we infer that the European slab is partially or completely broken off under the eastern Alps. Earlier works show a slab under the eastern Alps, down to 250 – 500 km, respectively (Lippitsch et al., 2003; Mitterbauer et al., 2011; Zhao et al., 2016). Yet, they all agree that the v_P anomaly between approximately 70 and 150 km depth is less pronounced compared to the deep slab. Zhao et al. (2016) give values for the deep anomaly below 150 km that are half as strong as in the central Alps. These findings are consistent with the striking difference in anomaly strength between central and eastern Alps in our model. The moderately increased velocities under the eastern Alps (about 1% compared to 3% under the central Alps) may be caused either by a deeper European slab, due to vertical smearing or by beginning subduction of Adriatic lithosphere, which is characterized by a less pronounced anomaly also under the Apennines and Dinarides. An interaction of partially broken off European slab and shallow Adriatic subduction is also possible.
There is an almost continuous transition between the eastern Alpine anomaly and the Dinaric slab. We interpret that the limit between the two domains should be south of the Periadriatic line, east of 14°E (Fig. 12). The complexity of the eastern Alpine structures is further increased by the presence of the sub-parallel Eastern Alpine Northern Anomaly north of the eastern Alps, which may be related to the slab detachment of the European plate.

The previously reported slab gap (e.g., Piromallo and Morelli, 2003) in the Dinaric subduction zone below 150 km is also visible in our model (Fig. 12, profiles H,K). At shallower depth, only a thin zone (80 km) of low velocities cuts through the Dinaric slab between 80 and 150 km depth (45°N – 45.6°N. The gap at depth is inferred to result from the roll-back of the subduction along the Dinaric-Hellenic front in combination with magmatism and extension in the Pannonian basin, which started at about 22 Ma (Handy et al., 2015). The extensional dynamics have probably started with a break-off of the Adriatic slab during the beginning of the continental collison 35 Ma ago causing the rise of asthenospheric mantle material (Handy et al., 2015). The location of the shallower low-velocity zone in our model at 45°N coincides spatially with the inferred location of the dextral strike-slip fault which was active until 10 Ma and separated the northward Adriatic indentation in the eastern Alps from the roll-back subduction south of it (Handy et al., 2015).

Our model shows that Dinaric and Apenninic slabs are only 200 km apart along profile K (Fig. 12). Both show a significantly weaker anomaly compared to the central Alpine slab (Fig. 12, profile C, K). The less pronounced anomaly may be caused by the large adjacent low-velocity domains under the Ligurian sea and the Pannonian basin, given the volume-averaging properties of long period surface waves and the smoothing in he phase-velocity maps.
The Apenninic slab in our model is vertical and is interrupted by a gap between 42°N and 43°N. Apenninic slab retreat (Vignaroli et al., 2008) can explain the very steep dip and the evidenced roll-back subduction. The geometry of the slab is in agreement with body-wave tomographic models of Koulakov et al. (2009) and Zhao et al. (2016) that show vertical subduction under the northern Apennines down to 150 km depth and a moderate dip to the southwest underneath. Body-wave tomography indicate further that the slab gap reaches down to 200 km depth but that the slab is continuous at greater depth (Wortel and Spakman, 2000; Koulakov et al., 2009; Zhao et al., 2016), which is below our model limit. The gap may indicate a beginning slab tear or intrusion of hot and slow mantle mantle material. Carminati and Doglioni (2012) remark that between 41°N and 42°N the main transition between the lower convergence rates of the northern Apennines and the higher ones of southern Apennines takes place. This is also expressed in orogenic magmatism in the north versus backarc-related magmatism in the south. The asymmetric convergence rates may be related to the slab tearing below.

6 Conclusions

The main goal of this work is to study the potential of combining AN- and EQ-based phase-velocity measurements in order to gain additional insight on the crust and mantle structures of the Alpine, Dinaric and Apenninic collision zones. A large data set of Rayleigh- and Love-wave phase-velocity measurements is compiled and used to derive high-resolution phase-velocity maps. Finally, we apply a non-linear model search to resolve the shear-velocity structure of the uppermost 200 km under the Alps, Apennines and northern Dinarides. Our model is unique in its combination of wide aperture and high lateral resolution in the crust ($\sim 25\ km$) and its continuity from the surface to the upper mantle. This allows us to make comparisons with detailed crustal studies from receiver functions and reflection seismics (Fig. 10) as well as to show the main geometries of the complex plate collisions and to discuss them with respect to earlier body-wave tomographic models.
Our high resolution crustal model reproduces successfully sedimentary basins, mid-

crustal anomalies and crustal thickness. It has therefore the potential to be a v_S reference model for the Alpine crust in future studies.
We derive a sharp Moho boundary from the applied model search which is in good agreement with previous receiver-function studies. We show that in situations with a high v_S contrast between crust and mantle, our results from surface waves differ by less than 5 km from receiver-function measurements. We find evidence for the Ivrea body geophysical anomaly in the western and central Alps, extending approximately along the Insubric line from 44.5°N to 46°N (Fig. 9).

In the western Alps we find indications that the subduction slab is detached below 100 km depth. This finding is based on a low-velocity zone that separates the European slab in the shallow mantle from a deeper, fast anomaly below 150 km depth. This is clearly different from the central Alpine slab, which is broad, continuous down to 200 km depth and shows a pronounced anomaly.
Also in the eastern Alps we find a signature of the fast anomaly that is clearly distinct from the central Alps. We infer that the European slab is detached under the eastern Alps. Results from body-wave tomography indicate that a detached European slab may be present at depth greater than 150 km (e.g., Mitterbauer et al., 2011). We find no unambiguous indication of a Adriatic subduction under the eastern Alps, but note that the moderately increased velocities can be interpreted this way. South of the Periadriatic line we interpret the fast anomaly as Adriatic subduction under the Dinarides.
We describe the Eastern Alpine Northern Anomaly, sub-parallel to the eastern Alps towards the north. This represents a potential area for further studies in order to determine its origin.

The Dinaric slab in our model extends to approximately 150 km depth and seems to be absent below. A thin zone of reduced velocities is also identified at shallower depths at 45°N.
The slab gap in the Apennines is clearly present in our models and is in agreement with previous studies based on body-wave tomography (e.g., Zhao et al., 2016).

The presented surface-wave study shows how the combination of AN and EQ records provide detailed models of the crust and also resolve the main structures of the upper mantle. This is especially important in the Alps where the structures are very complex and many open questions can only be answered if the continuity of the structures from crust to mantle can be followed. Teleseismic body-waves generally lack resolution in

the lithosphere and asthenosphere and are very dependent on the crustal corrections, while local earthquake tomography, reflection seismics or AN methods only provide good constraints on the crust. Therefore, one of the highlights of our model is the good continuous coverage down to 200 km depth. Future efforts would profit very much from the additional inclusion of teleseismic body wave data, to improve the resolution of the imaged structures and to be able to follow the Alpine slabs down to the mantle discontinuities.

Acknowledgements

We are grateful to all the network operators providing data to the EIDA archive (http://www.orfeus-eu.org/eida). We thank the makers of Obspy (Beyreuther et al., 2010) and Geopsy (www.geopsy.org). Graphics were created with Python Matplotlib and GMT (Wessel and Smith, 2001). A. E. acknowledges funding from the German Academic Exchange Service (DAAD). This project has received funding from the European Unions Horizon 2020 research and innovation program under the Marie Sklodowska-Curie grant agreement No. 641943.

References

Aki, K. (1957). Space and time spectra of stationary stochastic waves, with special reference to microtremors. *Bull. Earthq. Res. Inst.*, 35:411–451.

Auer, L., Boschi, L., Becker, T., Nissen-Meyer, T., and Giardini, D. (2014). Savani: A variable resolution whole-mantle model of anisotropic shear velocity variations based on multiple data sets. *Journal of Geophysical Research: Solid Earth*, 119(4):3006–3034.

Babuska, V. and Cara, M. (1991). *Seismic anisotropy in the Earth*, volume 10. Springer Science & Business Media.

Béthoux, N., Sue, C., Paul, A., Virieux, J., Fréchet, J., Thouvenot, F., and Cattaneo, M. (2007). Local tomography and focal mechanisms in the south-western alps: comparison of methods and tectonic implications. *Tectonophysics*, 432(1):1–19.

Beyreuther, M., Barsch, R., Krischer, L., Megies, T., Behr, Y., and Wassermann, J. (2010). ObsPy: A Python toolbox for seismology. *Seismological Research Letters*, 81(3):530–533.

Bleibinhaus, F. and Gebrande, H. (2006). Crustal structure of the Eastern Alps along the TRANSALP profile from wide-angle seismic tomography. *Tectonophysics*, 414(1):51–69.

Bois, C. and Party, E. S. (1990). Major geodynamic processes studied from the ECORS deep seismic profiles in France and adjacent areas. *Tectonophysics*, 173(1-4):397–410.

Boschi, L. (2006). Global multiresolution models of surface wave propagation: comparing equivalently regularized born and ray theoretical solutions. *Geophysical Journal International*, 167(1):238–252.

Boschi, L. and Dziewonski, A. M. (1999). High-and low-resolution images of the Earth's mantle: Implications of different approaches to tomographic modeling. *Journal of Geophysical Research: Solid Earth (1978–2012)*, 104(B11):25567–25594.

Bousquet, R., Goffé, B., Henry, P., Le Pichon, X., and Chopin, C. (1997). Kinematic, thermal and petrological model of the Central Alps: Lepontine metamorphism in the upper crust and eclogitisation of the lower crust. *Tectonophysics*, 273(1):105–127.

Carminati, E. and Doglioni, C. (2012). Alps vs. Apennines: the paradigm of a tectonically asymmetric Earth. *Earth-Science Reviews*, 112(1):67–96.

Castellarin, A., Nicolich, R., Fantoni, R., Cantelli, L., Sella, M., and Selli, L. (2006). Structure of the lithosphere beneath the Eastern Alps (southern sector of the TRANSALP transect). *Tectonophysics*, 414(1):259–282.

Consiglio Nazionale Delle Ricerche (1983). Structural model of Italy, 1:500.000. *Progetto Finalizzato Geodinamica*.

Diehl, T., Husen, S., Kissling, E., and Deichmann, N. (2009). High-resolution 3-D P-wave model of the Alpine crust. *Geophysical Journal International*, 179(2):1133–1147.

Dziewonski, A. M. and Anderson, D. L. (1981). Preliminary reference earth model. *Physics of the earth and planetary interiors*, 25(4):297–356.

ECORS, T. E.-C. D. S., Hirm, A., Nadir, S., Thouvenot, F., Nicolich, R., Pellis, G., Scarascia, S., Tabacco, I., Castellano, F., Merlanti, F., et al. (1989). Mapping the Moho of the Western Alps by wide-angle reflection seismics. *Tectonophysics*, 162(3-4):193–202.

Ekström, G. (2011). A global model of Love and Rayleigh surface wave dispersion and anisotropy, 25-250 s. *Geophysical Journal International*, 187(3):1668–1686.

Ekström, G., Abers, G. A., and Webb, S. C. (2009). Determination of surface-wave phase velocities across USArray from noise and Aki's spectral formulation. *Geophysical Research Letters*, 36(18).

Faccenna, C., Becker, T. W., Auer, L., Billi, A., Boschi, L., Brun, J. P., Capitanio, F. A., Funiciello, F., Horvàth, F., Jolivet, L., et al. (2014). Mantle dynamics in the Mediterranean. *Reviews of Geophysics*, 52(3):283–332.

Fry, B., Deschamps, F., Kissling, E., Stehly, L., and Giardini, D. (2010). Layered azimuthal anisotropy of Rayleigh wave phase velocities in the European Alpine lithosphere inferred from ambient noise. *Earth and Planetary Science Letters*, 297(1):95–102.

Geissler, W. H., Sodoudi, F., and Kind, R. (2010). Thickness of the central and eastern European lithosphere as seen by S receiver functions. *Geophysical Journal International*, 181(2):604–634.

Giacomuzzi, G., Chiarabba, C., and De Gori, P. (2011). Linking the Alps and Apennines subduction systems: new constraints revealed by high-resolution teleseismic tomography. *Earth and Planetary Science Letters*, 301(3):531–543.

Giacomuzzi, G., Civalleri, M., De Gori, P., and Chiarabba, C. (2012). A 3D Vs model of the upper mantle beneath Italy: Insight on the geodynamics of central Mediterranean. *Earth and Planetary Science Letters*, 335:105–120.

Goes, S., Govers, R., and Vacher, P. (2000). Shallow mantle temperatures under Europe from P and S wave tomography. *Journal of Geophysical Research: Solid Earth*, 105(B5):11153–11169.

Handy, M. R., Schmid, S. M., Bousquet, R., Kissling, E., and Bernoulli, D. (2010). Reconciling plate-tectonic reconstructions of Alpine Tethys with the geological–geophysical record of spreading and subduction in the Alps. *Earth-Science Reviews*, 102(3):121–158.

Handy, M. R., Ustaszewski, K., and Kissling, E. (2015). Reconstructing the Alps–Carpathians–Dinarides as a key to understanding switches in subduction polarity, slab gaps and surface motion. *International Journal of Earth Sciences*, 104(1):1–26.

Hirn, A., Damotte, B., Torreilles, G., and Party, E. S. (1987). Crustal reflection seismics: the contributions of oblique, low frequency and shear wave illuminations. *Geophysical Journal International*, 89(1):287–296.

Kästle, E. D., Soomro, R., Weemstra, C., Boschi, L., and Meier, T. (2016). Two-receiver measurements of phase velocity: cross-validation of ambient-noise and earthquake-based observations. *Geophysical Journal International*, 207(3):1493–1512.

Kissling, E. (1984). Three-dimensional gravity model of the northern Ivrea-Verbano Zone. *Wagner, J.-J., St. Müller (Eds.), Geomagnetic and Gravimetric Studies of the Ivrea Zone: Matér. Géol. Suisse. Géophys*, 21:55–61.

Kissling, E. (2008). Deep structure and tectonics of the Valaisand the rest of the Alps. *Bulletin fuer Angewandte Geologie*, 13(2):3–10.

Köhler, A., Weidle, C., and Maupin, V. (2012). Crustal and uppermost mantle structure of southern Norway: results from surface wave analysis of ambient seismic noise and earthquake data. *Geophysical Journal International*, 191(3):1441–1456.

Koulakov, I., Kaban, M., Tesauro, M., and Cloetingh, S. (2009). P-and s-velocity anomalies in the upper mantle beneath europe from tomographic inversion of isc data. *Geophysical Journal International*, 179(1):345–366.

Kovach, R. L. (1978). Seismic surface waves and crustal and upper mantle structure. *Reviews of Geophysics*, 16(1):1–13.

Kummerow, J., Kind, R., Oncken, O., Giese, P., Ryberg, T., Wylegalla, K., Scherbaum, F., Group, T. W., et al. (2004). A natural and controlled source seismic profile through the Eastern Alps: TRANSALP. *Earth and Planetary Science Letters*, 225(1):115–129.

Legendre, C., Meier, T., Lebedev, S., Friederich, W., and Viereck-Götte, L. (2012). A shear wave velocity model of the European upper mantle from automated inversion of seismic shear and surface waveforms. *Geophysical Journal International*, 191(1):282–304.

Li, C., van der Hilst, R. D., Engdahl, E. R., and Burdick, S. (2008). A new global model for P wave speed variations in Earth's mantle. *Geochemistry, Geophysics, Geosystems*, 9(5).

Lin, F.-C., Moschetti, M. P., and Ritzwoller, M. H. (2008). Surface wave tomography of the western United States from ambient seismic noise: Rayleigh and Love wave phase velocity maps. *Geophysical Journal International*, 173(1):281–298.

Lippitsch, R., Kissling, E., and Ansorge, J. (2003). Upper mantle structure beneath the alpine orogen from high-resolution teleseismic tomography. *Journal of Geophysical Research: Solid Earth*, 108(B8).

Lombardi, D., Braunmiller, J., Kissling, E., and Giardini, D. (2008). Moho depth and Poisson's ratio in the Western-Central Alps from receiver functions. *Geophysical Journal International*, 173(1):249–264.

Lüschen, E., Lammerer, B., Gebrande, H., Millahn, K., Nicolich, R., Group, T. W., et al. (2004). Orogenic structure of the Eastern Alps, Europe, from TRANSALP deep seismic reflection profiling. *Tectonophysics*, 388(1):85–102.

Meier, T., Dietrich, K., Stöckhert, B., and Harjes, H.-P. (2004). One-dimensional models of shear wave velocity for the eastern Mediterranean obtained from the inversion of Rayleigh wave phase velocities and tectonic implications. *Geophysical Journal International*, 156(1):45–58.

Meier, T., Soomro, R., Viereck, L., Lebedev, S., Behrmann, J. H., Weidle, C., Cristiano, L., and Hanemann, R. (2016). Mesozoic and Cenozoic evolution of the Central European lithosphere. *Tectonophysics*, 692:58–73.

Mitterbauer, U., Behm, M., Brückl, E., Lippitsch, R., Guterch, A., Keller, G. R., Koslovskaya, E., Rumpfhuber, E.-M., and Šumanovac, F. (2011). Shape and origin of the east-alpine slab constrained by the alpass teleseismic model. *Tectonophysics*, 510(1):195–206.

Molinari, I., Argnani, A., Morelli, A., and Basini, P. (2015). Development and testing of a 3D seismic velocity model of the Po Plain sedimentary basin, Italy. *Bulletin of the Seismological Society of America*, 105(2A):753–764.

Muyzert, E. and Snieder, R. (2000). An alternative parameterisation for surface waves in a transverse isotropic medium. *Physics of the Earth and Planetary Interiors*, 118(1):125–133.

Oeberseder, T., Behm, M., Kovács, I., and Falus, G. (2011). A seismic discontinuity in the upper mantle between the Eastern Alps and the Western Carpathians: Constraints from wide angle reflections and geological implications. *Tectonophysics*, 504(1):122–134.

Paige, C. C. and Saunders, M. A. (1982). Lsqr: An algorithm for sparse linear equations and sparse least squares. *ACM transactions on mathematical software*, 8(1):43–71.

Pfiffner, O.-A. (1992). *Blundell, DJ, Freeman, R, Mueller, S and Button, S: A continent revealed: The European Geotraverse, structure and dynamic evolution.* Cambridge University Press.

Pfiffner, O.-A., Lehner, P., Heitzmann, P., Mueller, S., and Steck, A. (1997). *Deep structure of the Swiss Alps.* Springer.

Piromallo, C. and Morelli, A. (2003). P wave tomography of the mantle under the alpine-mediterranean area. *Journal of Geophysical Research: Solid Earth*, 108(B2).

Roure, F., Choukroune, P., and Polino, R. (1996). Deep seismic reflection data and new insights on the bulk geometry of mountain ranges. *Comptes rendus de l'Académie des sciences. Série 2. Sciences de la terre et des planètes*, 322(5):345–359.

Sambridge, M. (1999). Geophysical inversion with a neighbourhood algorithmii. appraising the ensemble. *Geophysical Journal International*, 138(3):727–746.

Sato, Y. (1955). Analysis of Dispersed Surface Waves by means of Fourier Transform I.

Schmid, S. and Kissling, E. (2000). The arc of the western alps in the light of geophysical data on deep crustal structure. *Tectonics*, 19(1):62–85.

Seiberlich, C., Ritter, J., and Wawerzinek, B. (2013). Topography of the lithosphere–asthenosphere boundary below the Upper Rhine Graben Rift and the volcanic Eifel region, Central Europe. *Tectonophysics*, 603:222–236.

Shen, W., Ritzwoller, M. H., and Schulte-Pelkum, V. (2013). A 3-D model of the crust and uppermost mantle beneath the Central and Western US by joint inversion of receiver functions and surface wave dispersion. *Journal of Geophysical Research: Solid Earth*, 118(1):262–276.

Singer, J., Diehl, T., Husen, S., Kissling, E., and Duretz, T. (2014). Alpine lithosphere slab rollback causing lower crustal seismicity in northern foreland. *Earth and Planetary Science Letters*, 397:42–56.

Soomro, R., Weidle, C., Cristiano, L., Lebedev, S., Meier, T., Group, P. W., et al. (2016). Phase velocities of Rayleigh and Love waves in central and northern Europe from automated, broad-band, interstation measurements. *Geophysical Journal International*, 204(1):517–534.

Spada, M., Bianchi, I., Kissling, E., Agostinetti, N. P., and Wiemer, S. (2013). Combining controlled-source seismology and receiver function information to derive 3-D Moho topography for Italy. *Geophysical Journal International*, 194(2):1050–1068.

Spakman, W. and Wortel, R. (2004). A tomographic view on western Mediterranean geodynamics. In *The TRANSMED atlas. The Mediterranean region from crust to mantle*, pages 31–52. Springer.

Stampfli, G. M. and Borel, G. (2002). A plate tectonic model for the Paleozoic and Mesozoic constrained by dynamic plate boundaries and restored synthetic oceanic isochrons. *Earth and Planetary Science Letters*, 196(1):17–33.

Stehly, L., Fry, B., Campillo, M., Shapiro, N., Guilbert, J., Boschi, L., and Giardini, D. (2009). Tomography of the Alpine region from observations of seismic ambient noise. *Geophysical Journal International*, 178(1):338–350.

Thouvenot, F., Paul, A., Frechet, J., Béthoux, N., Jenatton, L., and Guiguet, R. (2007). Are there really superposed Mohos in the southwestern Alps? new seismic data from fan-profiling reflections. *Geophysical Journal International*, 170(3):1180–1194.

TRANSALP Working Group, Gebrande, H., Lüschen, E., Bopp, M., Bleibinhaus, F., Lammerer, B., Oncken, O., Stiller, M., Kummerow, J., Kind, R., Millahn, K., et al. (2002). First deep seismic reflection images of the Eastern Alps reveal giant crustal wedges and transcrustal ramps. *Geophysical Research Letters*, 29(10).

Verbeke, J., Boschi, L., Stehly, L., Kissling, E., and Michelini, A. (2012). High-resolution Rayleigh-wave velocity maps of central Europe from a dense ambient-noise data set. *Geophysical Journal International*, 188(3):1173–1187.

Vignaroli, G., Faccenna, C., Jolivet, L., Piromallo, C., and Rossetti, F. (2008). Subduction polarity reversal at the junction between the Western Alps and the Northern Apennines, Italy. *Tectonophysics*, 450(1):34–50.

Ward, K. M., Zandt, G., Beck, S. L., Wagner, L. S., and Tavera, H. (2016). Lithospheric structure beneath the northern Central Andean Plateau from the joint inversion of ambient noise and earthquake-generated surface waves. *J. Geophys. Res.: Solid Earth*, 121(11):8217–8238.

Wathelet, M. (2005). Array recordings of ambient vibrations: surface-wave inversion. *PhD Diss., Liége University*, 161.

Wathelet, M. (2008). An improved neighborhood algorithm: parameter conditions and dynamic scaling. *Geophysical Research Letters*, 35(9).

Wessel, P. and Smith, W. H. (2001). The Generic Mapping Tools.

Wortel, M. and Spakman, W. (2000). Subduction and slab detachment in the mediterranean-carpathian region. *Science*, 290(5498):1910–1917.

Yang, Y., Li, A., and Ritzwoller, M. H. (2008a). Crustal and uppermost mantle structure in southern Africa revealed from ambient noise and teleseismic tomography. *Geophysical Journal International*, 174(1):235–248.

Yang, Y., Ritzwoller, M. H., Lin, F.-C., Moschetti, M., and Shapiro, N. M. (2008b). Structure of the crust and uppermost mantle beneath the western United States revealed by ambient noise and earthquake tomography. *Journal of Geophysical Research: Solid Earth*, 113(B12).

Zhao, L., Paul, A., Guillot, S., Solarino, S., Malusà, M. G., Zheng, T., Aubert, C., Salimbeni, S., Dumont, T., Schwartz, S., et al. (2015). First seismic evidence for continental subduction beneath the Western Alps. *Geology*, 43(9):815–818.

Zhao, L., Paul, A., Malusà, M. G., Xu, X., Zheng, T., Solarino, S., Guillot, S., Schwartz, S., Dumont, T., Salimbeni, S., et al. (2016). Continuity of the Alpine slab unraveled by high-resolution P wave tomography. *Journal of Geophysical Research: Solid Earth*.

Zhou, L., Xie, J., Shen, W., Zheng, Y., Yang, Y., Shi, H., and Ritzwoller, M. H. (2012). The structure of the crust and uppermost mantle beneath South China from ambient noise and earthquake tomography. *Geophysical Journal International*, 189(3):1565–1583.

Zhu, H., Bozdağ, E., Peter, D., and Tromp, J. (2012). Structure of the European upper mantle revealed by adjoint tomography. *Nature Geoscience*, 5(7):493–498.

Ziegler, P., Schumacher, M., Dèzes, P., Van Wees, J.-D., and Cloetingh, S. (2004). Post-variscan evolution of the lithosphere in the Rhine Graben area: constraints from subsidence modelling. *Geological Society, London, Special Publications*, 223(1):289–317.

3.1 Supplementary material

3.1.1 Crustal velocity structure

In this section the crustal structure along five cross-sections is studied in more detail (Fig. 3.1, 3.2). The structural model is taken from Schmid et al. (2017) who base their original transects partially on the v_P isolines from Diehl et al. (2009) (Fig. 3.3). In the shear-velocity model the 4.2 km/s iso-velocity corresponds to the crust-mantle boundary. It coincides well with the European Moho from the shown transects with differences less than 5 km. In all transects a lower temperature gradient in the upper crust is observed towards the collision zone which can be explained with the thickened crust. At the plate contact, the velocities in the upper 30 km increase significantly due to the high-pressure Briançonnais and the Ivrea body (intrusion of Adriatic mantle). This effect is most clearly seen in transects b through d. The fact that the Adriatic mantle upwelling is not imaged as crust-mantle velocity jump is also addressed in the text above: Wavelength of the surface-waves and the non-uniqueness of the inverse problem lead to smoothed structures in the crust. The by Schmid et al. (2017) inferred limits between upper and lower crust coincide with the 3.6–3.8 km/s contours from the v_S model.

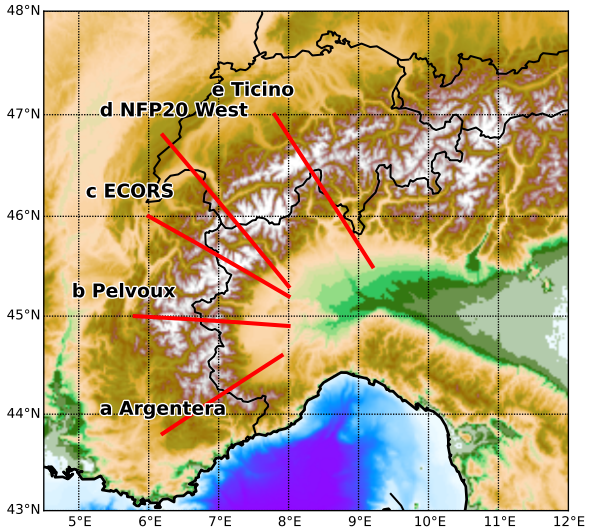

Figure 3.1: Location of the profiles through western and central Alps from Schmid et al. (2017).

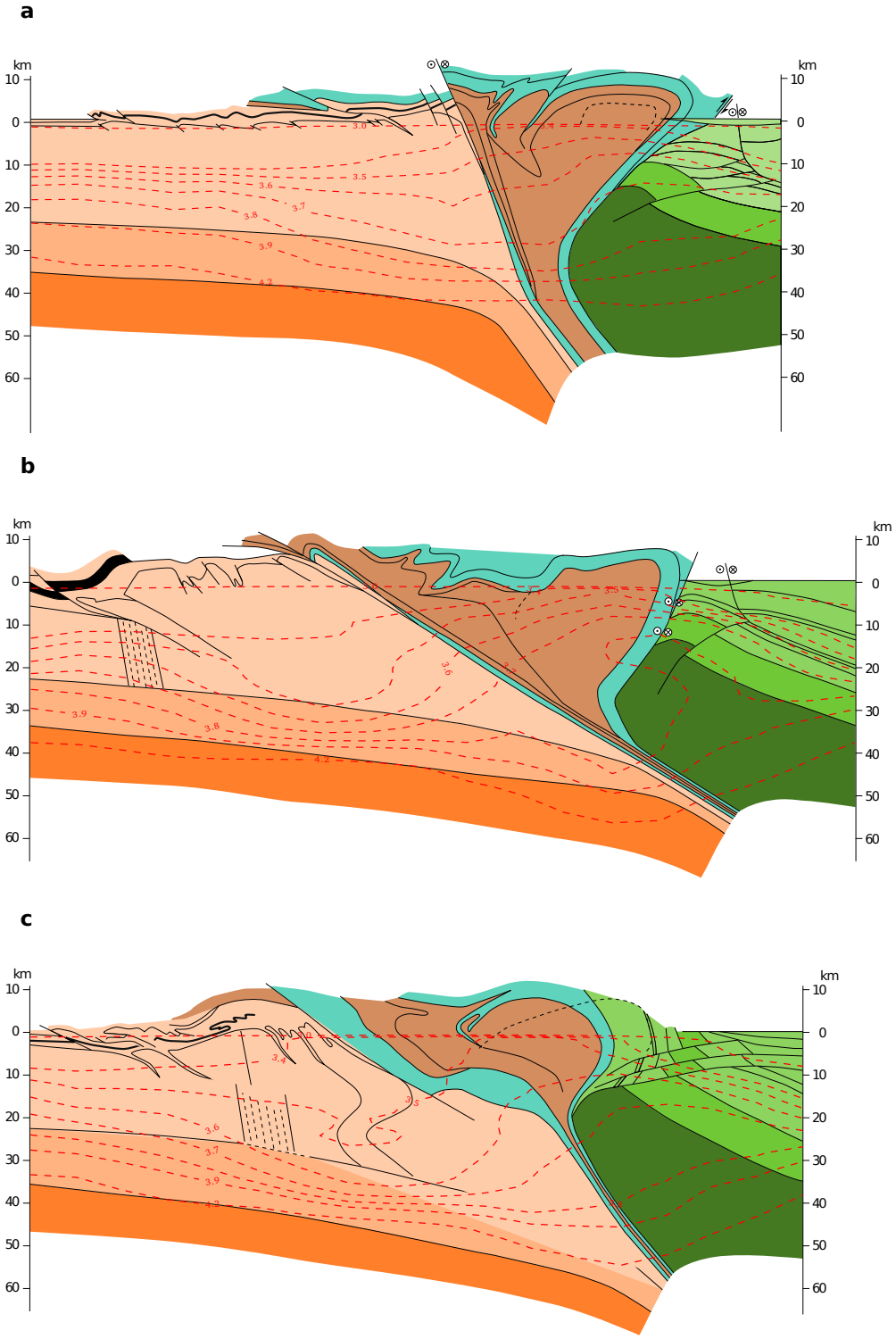
a
km
10
0
10
20
30
40
50
60
3.6
3.5
3.6
3.7
3.8
3.9
4.2
b
3.6
3.9
3.8
4.2
c
3.6
3.7
3.9
4.2

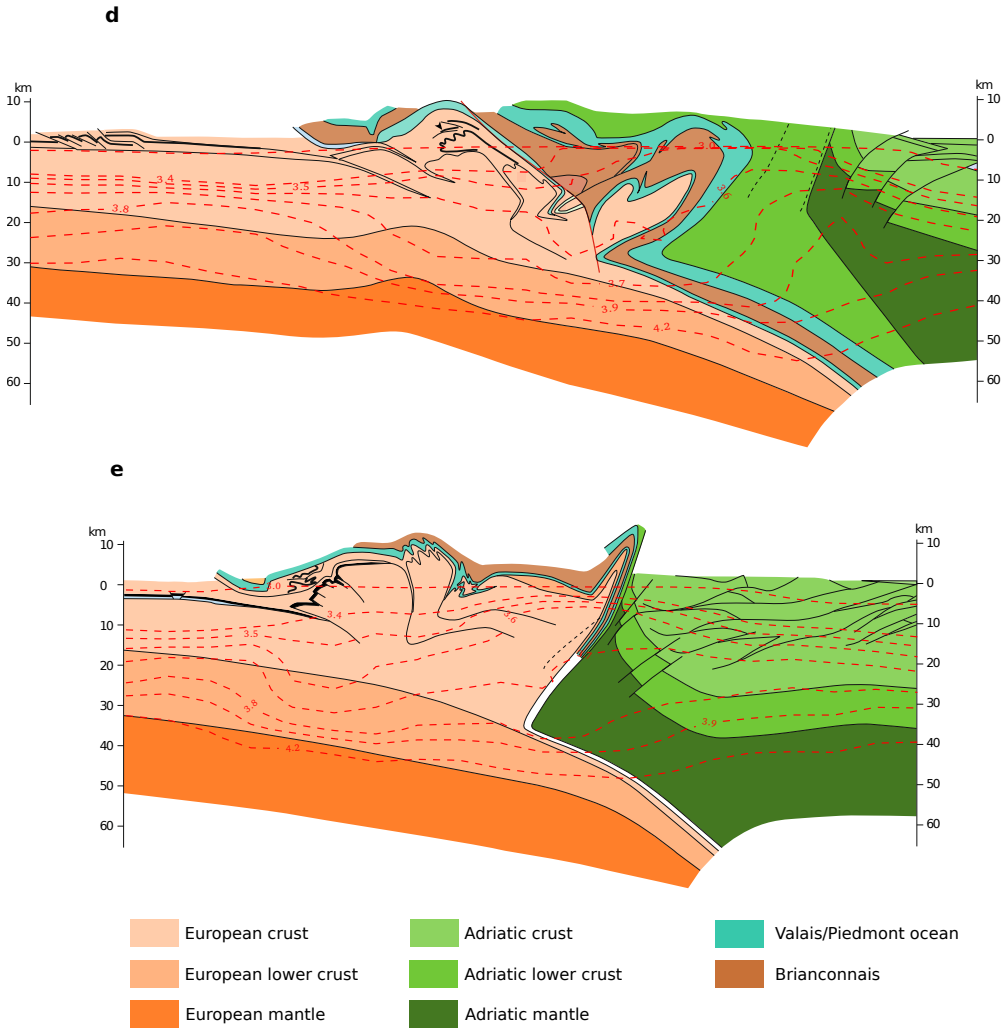

Figure 3.2: Five simplified geological-tectonic sections across the western and central Alps. Superimposed are v_S isolines from the herein presented model. **a** Argentera transect; **b** Pelvoux transect; **c** ECORS-CROP transect; **d** NFP 20 West transect; **e** Ticino transect. Figure modified after Schmid et al. (2017).

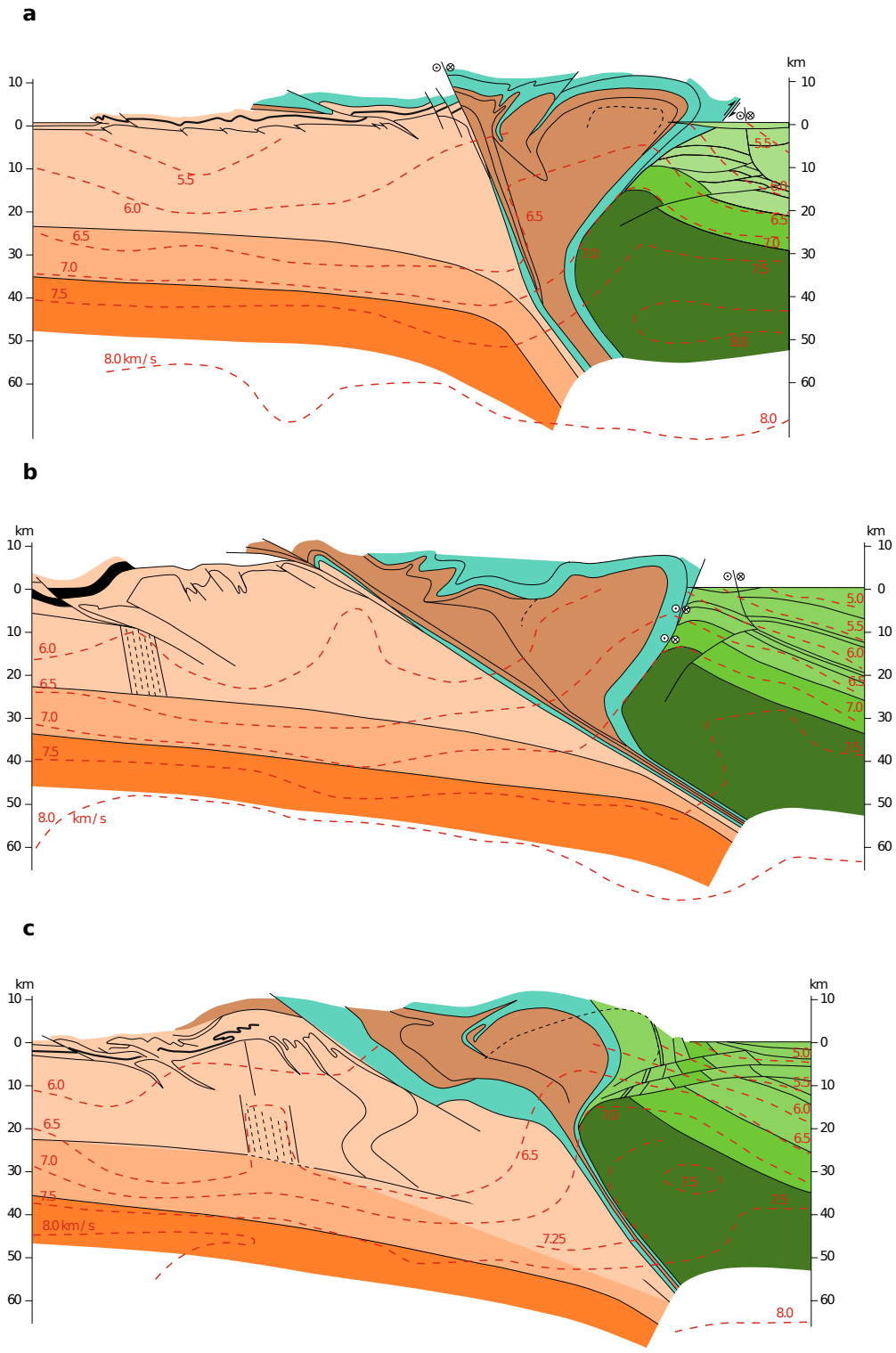
a
km
10
0
10
20
30
40
50
60
5.5
6.0
6.5
7.0
7.5
8.0 km/s
8.0
b
km
5.0
5.5
6.0
6.5
7.0
7.5
8.0 km/s
c
km
6.0
6.5
7.0
7.5
8.0 km/s
7.25
8.0

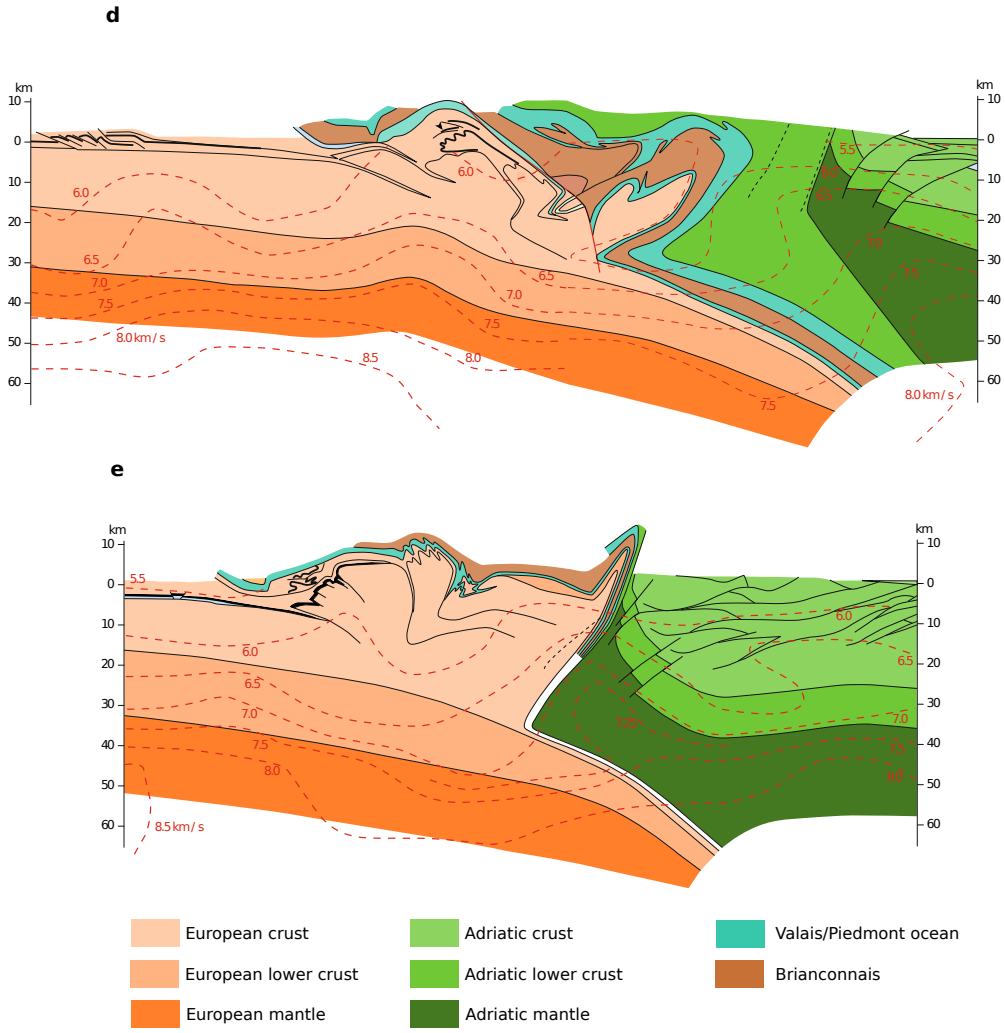

Figure 3.3: Five simplified geological-tectonic sections across the western and central Alps. Superimposed are v_P isolines from Diehl et al. (2009). The transects are partially based on the shown isolines. **a** Argentera transect; **b** Pelvoux transect; **c** ECORS-CROP transect; **d** NFP 20 West transect; **e** Ticino transect. Figure modified after Schmid et al. (2017).

3.1.2 Upper mantle v_{SV} and v_{SH}

The figures 3.4 and 3.5 show the mantle structure for Rayleigh-only and Love-only inversions. The primary structures such as slabs and low-velocity regions are imaged

with each separate dataset. Only the Apenninic slab is almost not present in the v_{SH} (Love-wave) model. The Love-wave model shows also less details which is probably due to the larger wavelength of Love waves. In the Rayleigh model the difference in anomaly strength between the different slabs vanishes. Interesting differences can also be seen in the western Alps and the northern Dinarides where Love- and Rayleigh-wave models show opposite anomalies.
Some of these differences may find an explanation in terms of radial anisotropy, which is determined here from the ratio of horizontally (v_{SH}) to vertically (v_{SV}) polarized shear velocity (Fig. 3.6),

$$\xi = \frac{v_{SH}^2}{v_{SV}^2}. \tag{3.1}$$

This implies vertical flow under the Apennines, Ligurian basin, but also at the transition between western and central Alps as well as between eastern Alps and Dinarides and rather horizontal flow elsewhere. At lithospheric depths it would show the frozen-in flow while in the asthenosphere it rather represents the current flow. The strong vertical flow under the Apennines and in the Ligurian basin can be reasonably related to subduction and asthenospheric upwelling, respectively. The absence of subduction-induced vertical flow in the Alps is, however, difficult to explain and may indicate that the applied method is not suited to determine the radially anisotropy structure. A comparison with the flow model of Schaefer et al. (2011) shows that the lowest values of ξ are expected in the Alps and no significant anisotropy in the Apennines. This is opposite to the structures shown in figure 3.6. Yet, the horizontal flow under the Alps can be explained with the model of Vignaroli et al. (2008), assuming that the Alpine subduction has largely stopped. Interpretations remain, however, very speculative.

3.2 Concluding remarks

This chapter presents the entire data set used in this study and gives an overview of how the data has been prepared and evaluated to obtain the phase-velocity measurements. The data are used in a linearized inversion to create a set of 2-D phase-velocity maps at different periods. These show already areas of fast and slow structures and give an impression of the anomalies in crust and mantle. By combination of the maps, a dispersion curve at each point of the model is obtained, which is used in a non-linear model search to find the shear-velocity profile between the surface and 200 km depth. Combining (and smoothing in the mantle) of all of these depth profiles results in the final 3-D model.
Crustal structures and mantle structures are discussed separately. The structure of

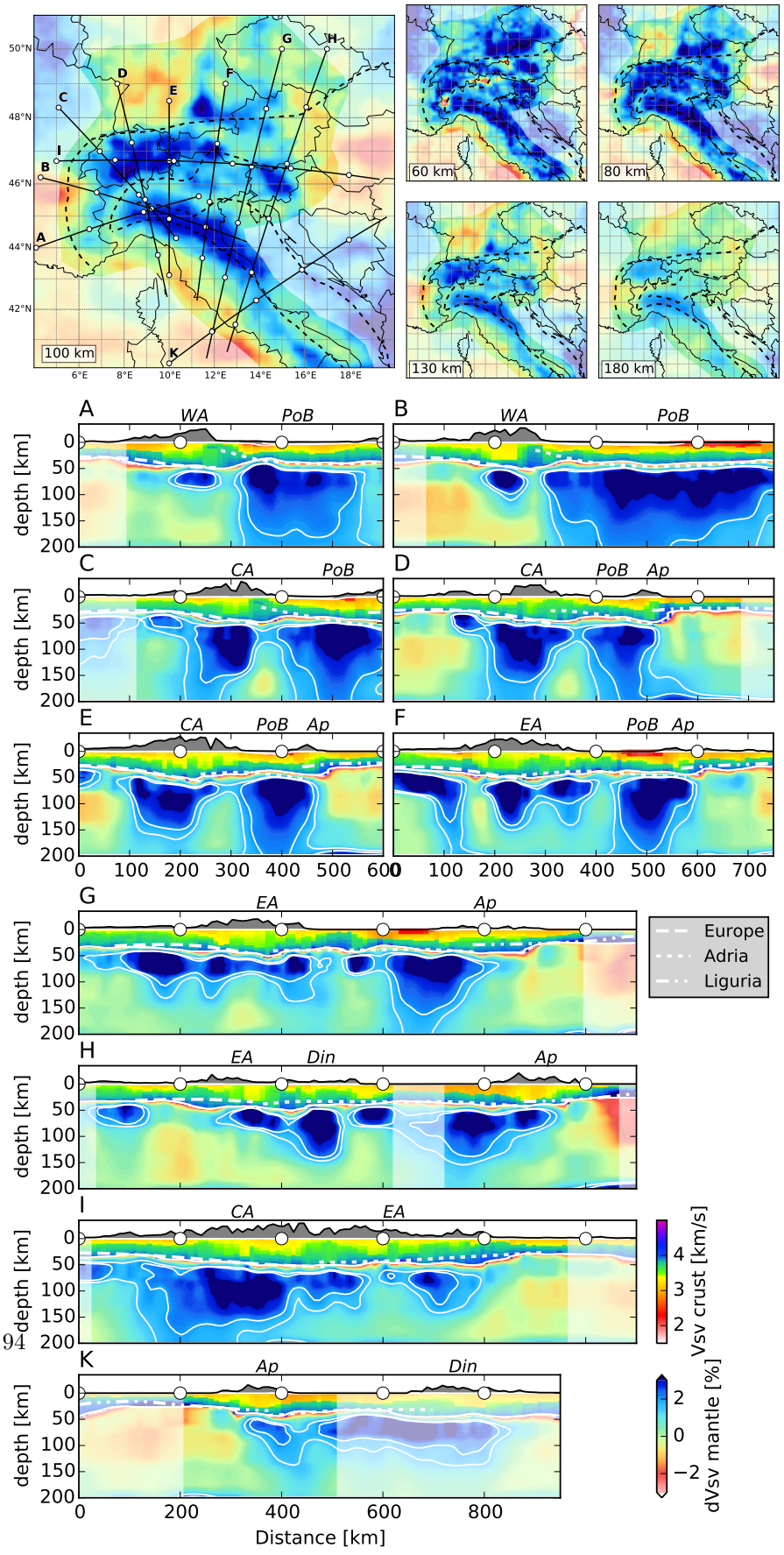
100 km
60 km
80 km
130 km
180 km
A
B
C
D
E
F
G
H
I
K
WA
PoB
CA
Ap
EA
Din
depth [km]
Distance [km]
Europe
Adria
Liguria
Vsv crust [km/s]
dVsv mantle [%]

Figure 3.4: Mantle structure in map view and along 10 different cross-sections based only on Rayleigh waves as approximation of deviations from PREM-v_{SV} (Dziewonski and Anderson, 1981). For an explanation of the dashed limits in the maps refer to Figure 1 in the above article. Moho boundary lines in the cross sections for European, Ligurian and Adriatic plate are taken from the receiver-function and CSS study of Spada et al. (2013). Regions of lower resolution are shown with reduced color intensities, according to the resolution tests in the above article. The +1.5% and +2.0% contour lines are shown to emphasize the slab anomalies. The abbreviations on top of each section refer to the topography: WA: Western Alps; CA: Central Alps; EA: Eastern Alps; Ap: Apennines; Din: Dinarides; PoB: Po sedimentary basin.

the upper mantle slabs in the Alps is briefly discussed in comparison to earlier studies and the tectonic history. However, a more thorough discussion including a complete overview of previous results from body-wave tomographic models is only given in the following chapter.

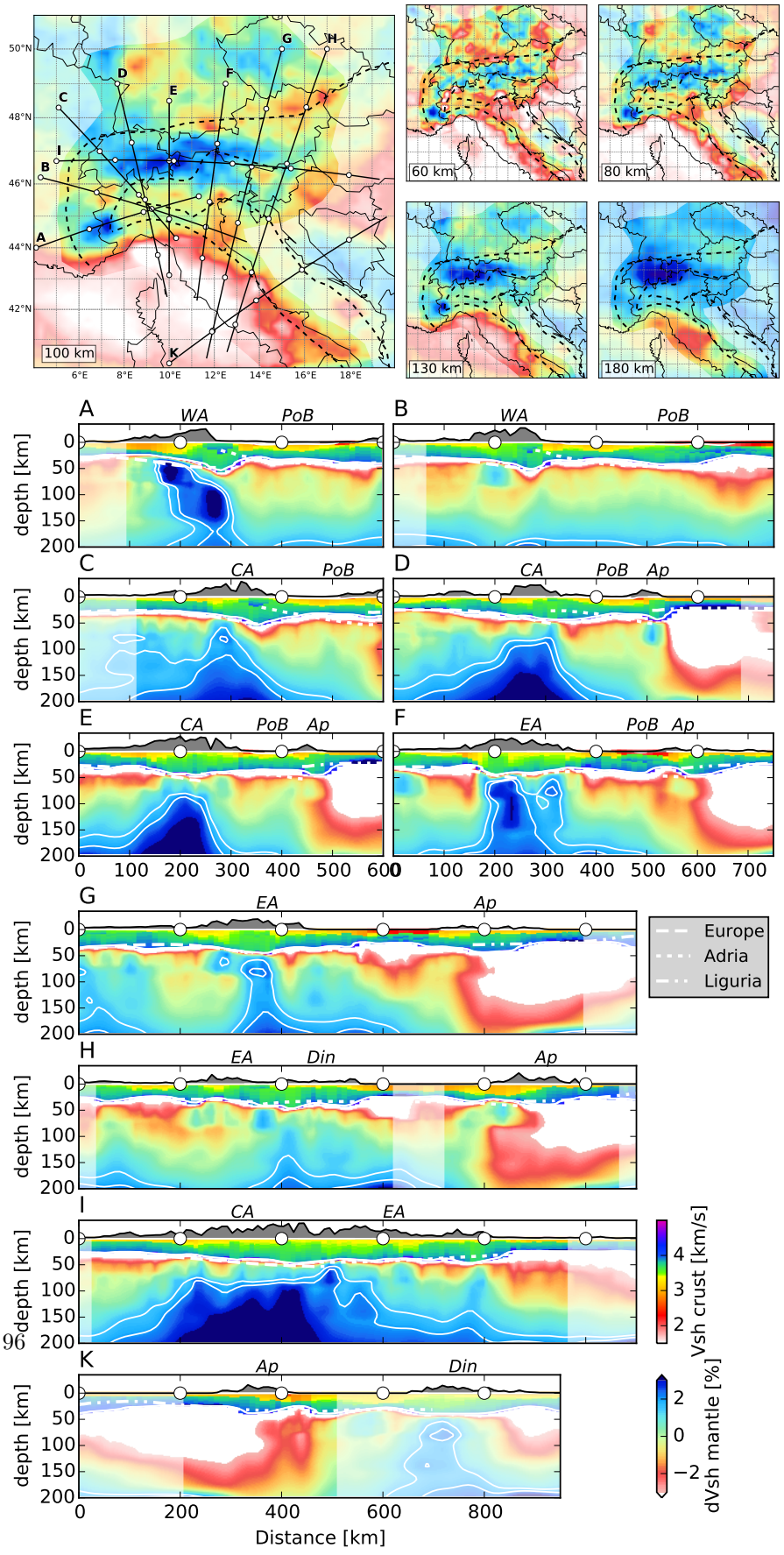
50°N
48°N
46°N
44°N
42°N
6°E
8°E
10°E
12°E
14°E
16°E
18°E
A
B
C
D
E
F
G
H
I
K
100 km
60 km
80 km
130 km
180 km
depth [km]
WA
PoB
CA
Ap
EA
Din
Europe
Adria
Liguria
Vsh crust [km/s]
dVsh mantle [%]
Distance [km]

Figure 3.5: Mantle structure in map view and along 10 different cross-sections based only on Love waves as approximation of deviations from PREM-v_{SH} (Dziewonski and Anderson, 1981). For an explanation of the dashed limits in the maps refer to Figure 1 in the above article. Moho boundary lines in the cross sections for European, Ligurian and Adriatic plate are taken from the receiver-function and CSS study of Spada et al. (2013). Regions of lower resolution are shown with reduced color intensities, according to the resolution tests in the above article. The +1.5% and +2.0% contour lines are shown to emphasize the slab anomalies. The abbreviations on top of each section refer to the topography: WA: Western Alps; CA: Central Alps; EA: Eastern Alps; Ap: Apennines; Din: Dinarides; PoB: Po sedimentary basin.

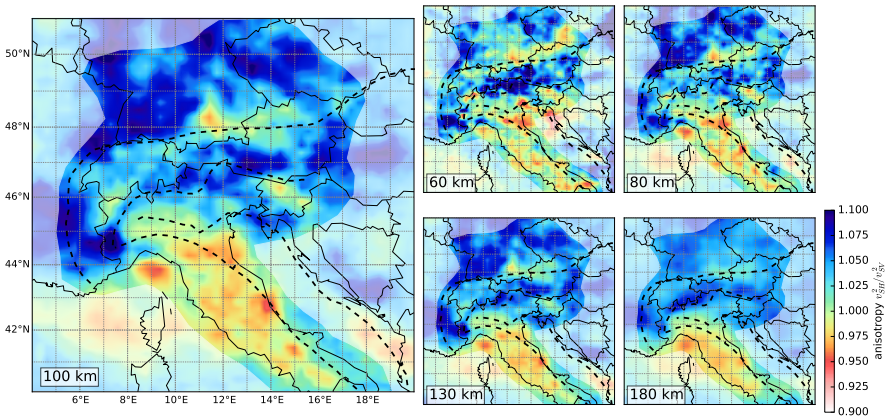

Figure 3.6: Radial anisotropy from separate inversions of Love- and Rayleigh-waves structure. For an explanation of the dashed limits in the maps refer to Figure 1 in the above article. Values of $\xi > 1$ can be interpreted as horizontal flow and values of $\xi < 1$ as vertical flow (e.g., Schaefer et al., 2011).

4 The Alpine slab detachments

unpublished

The third article within this thesis gives a more thorough comparison and interpretation of the mantle structures under the Alps from the herein presented surface-wave model. It is shown along different cross-sections through the Alps in direct comparison with body-wave tomographic models of Koulakov et al. (2009), Mitterbauer et al. (2011) and Zhao et al. (2016). Also a joint model is created by combination of the surface-wave model with the model of Zhao et al. (2016) where the two models are linked at the 140 km depth horizon. The discussion focuses especially on the western and eastern Alps, where a detachment of the European subduction slab is proposed.

The Alpine slab detachments

Emanuel D. Kästle[1], Lapo Boschi[1], Claudio Rosenberg[1], Nicolas Bellahsen[1], and Thomas Meier[2]

[1]Institut des Sciences de la Terre, Paris (iSTeP), Université Pierre et Marie Curie, Paris, France.
[2]Universität Kiel, Germany

September 5, 2017

After the Adriatic and European continental plate collided, the subduction processes changed dramatically in the Alps: European plate break-offs all around the Alpine arc in both early and late stages of the collision and subduction polarity reversal in the eastern Alps have been proposed. Evidence of this history should be found in the upper mantle, yet the slab geometries shown by tomographic imaging are ambiguous especially in the upper 150 km. We review earlier body-wave tomographic studies and compare them to a surface-wave derived model which is more reliable in the crucial mantle zone directly underneath the crust. Our model indicates that both in the western and the eastern Alps the European plate is detached. We argue that the deep slab under the eastern Alps represents the detached European slab which is sub-vertical to slightly overturned.

1 Introduction

The Alps and the adjacent Apenninic, Dinaric and Carpathian mountain chains were formed by a complex history of plate subduction and collision. The major driving force is the N-S convergence of Africa and Europe that has started approximately 200 Ma (Handy et al., 2010). Between 84 Ma and 35 Ma, Adria-Africa acted as upper plate along most of the subduction front and the Alpine Tethys was subducted towards the south. An opposite subduction direction can only be inferred along what would later become the Dinaric-Hellenic arc (Handy et al., 2015, Fig. 1). This changed with the continent-continent collision starting at 35 Ma. Slab break-offs are proposed along all

collision zones combined with volcanic activity (Blanckenburg and Davies, 1995). This also led to a reversal of subduction polarity in the Adria-Liguria collision (Vignaroli et al., 2008; Handy et al., 2010). Slab-retreat of the newly subducting Adriatic plate caused caused extension in the Ligurian sea and initiated the orogen curvature in the western Alps northern Apennines (Vignaroli et al., 2008; Schmid et al., 2017). A similar mechanism is proposed for the Dinaric subduction: while Adria was already the lower plate, after the continent collision and slab break-off, ongoing slab retreat gave the way for rising asthenospheric material and causing extension in the Pannonian basin (e.g., Faccenna et al., 2014).
In the Alps, it is generally accepted that Europe remained the lower plate after collision and potential slab break-off. Only in the eastern Alps the teleseismic tomographic results of Lippitsch et al. (2003) have started a discussion on the apparent northward dip of the slab between 50 and 250 km depth, suggesting that it may be due to subduction of Adria under Europe (Schmid et al., 2004; Ustaszewski et al., 2008; Handy et al., 2015). This would have been possible after the proposed slab break-off in the Alps, giving way for a northward indentation of the Adriatic plate (e.g., Ustaszewski et al., 2008). This corresponds to the main period of shortening in the southern Alps between 14–7 Ma, while the Adriatic plate was subject to a counter-clockwise rotation (Ustaszewski et al., 2008).

Up to date, the high-resolution regional tomographic models of the Alpine upper mantle disagree on important structures, such as the suggested detachment of the European slab under the western Alps and the subduction polarity under the eastern Alps (Adriatic vs. European subduction) (Lippitsch et al., 2003; Koulakov et al., 2009; Dando et al., 2011; Mitterbauer et al., 2011; Zhao et al., 2016; Hua et al., 2017). An important limiting factor is the lack of resolution in the upper ∼150 km of teleseismic body-wave models due to almost vertical ray paths. We recently presented a shear-velocity model of the crust and upper mantle, based on the inversion of surface-wave phase velocities from ambient-noise and earthquake measurements, which does not suffer from this limitation (Kästle et al., 2017). In the light of this new model, we want to re-discuss the issues of eastern and western Alpine slab geometries and the potential slab detachments of the European plate. By comparing the structures of the shallow upper mantle to the body-wave tomographic models we give an updated review of the tectonic processes as seen from tomographic imaging.

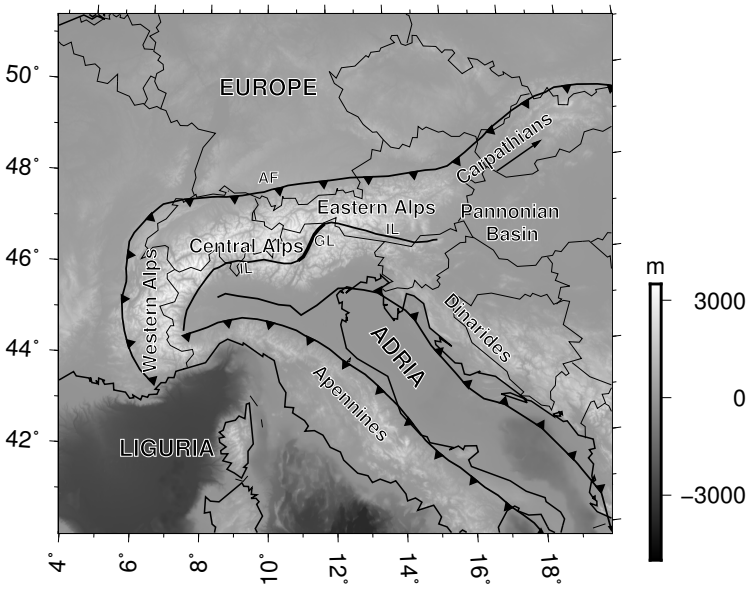

Figure 1: Map of the main tectonic units involved in the Alpine continental collision. AF: Alpine frontal thrust, IL: Insubric line, GL: Giudicarie line. Tectonic limits from Faccenna et al. (2014).

2 Eastern Alps

Studies using teleseismic body-waves have shown that the slab under the eastern Alps reaches at least to 250 km depth (Lippitsch et al., 2003), but probably even deeper to 350 km and more (Koulakov et al., 2009; Mitterbauer et al., 2011; Dando et al., 2011; Zhao et al., 2016; Hua et al., 2017, Tab. 1). It is assumed that a potential northward subduction of the Adriatic plate cannot explain a slab length of more than 190 km (Ustaszewski et al., 2008; Handy et al., 2015), which corresponds to the total N-S shortening in the eastern Alps (Ustaszewski et al., 2008). Ustaszewski et al. (2008) assume that a large portion of that shortening happened in the southern Alps, i.e. the Adriatic plate, however, field-related estimates suggest shortening values of only 50–75 km on the Adriatic side, although these are understood to be minimum estimates (Schönborn, 1999; Nussbaum, 2000; Brückl, 2011). The total slab length of an Adriatic subduction in the eastern Alps should therefore be between 50 and maximum 190 km. If the upper portion of the eastern Alpine slab is due to the northward subduction of Adria, how can the deeper slab be explained?

Table 1: Main observations concerning the subduction polarity in the eastern Alps from body-wave tomography.

Depth of slab tip (variable along latitude)	250 km (Lippitsch et al., 2003) > 410 km (Koulakov et al., 2009) > 300 km? (Dando et al., 2011) > 410 km (Mitterbauer et al., 2011) > 410 km (Zhao et al., 2016) > 410 km (Hua et al., 2017)
Slab dip	All body-wave tomographic models show a vertical to subvertical, slightly northward dipping slab between 12 and 14°E (Lippitsch et al., 2003; Koulakov et al., 2009; Dando et al., 2011; Mitterbauer et al., 2011; Zhao et al., 2016; Hua et al., 2017).
E-W slab continuity	All models show a gap or discontinuity (northward step) between central and eastern Alpine anomalies (Lippitsch et al., 2003; Koulakov et al., 2009; Mitterbauer et al., 2011; Zhao et al., 2016; Hua et al., 2017).
N-S shortening	Total of 190 km, mostly in the southern Alps (Ustaszewski et al., 2008) minimum 55 – 75 km in the southern Alps (Brückl, 2011) minimum 50 km in the southern Alps (Schönborn, 1999; Nussbaum, 2000)
Moho offset	An offset suggesting that Europe is the lower plate is only imaged along the TRANSALP cross-section (Kummerow et al., 2004). This may be due to indentation of Adria at mid-crustal levels. Otherwise the Moho structure is ambiguous (e.g., Spada et al., 2013).
Slab detachment	The continuity of the eastern Alpine slab in the upper 150 km is ambiguous. Between 12°E and 15°E, the tomographic models show a slab that reaches up to 150–50 km depth. Some models show a significantly weaker anomaly above 150 km compared to the central Alps or compared to the deeper eastern Alpine slab (Mitterbauer et al., 2011; Zhao et al., 2016; Hua et al., 2017, the latter two studies argue nevertheless in favor of an attaches slab). A rather attached slab can be inferred from the models of Lippitsch et al. (2003), Koulakov et al. (2009) and Dando et al. (2011). All models that cover areas east of 15°E show that the slab is detached there (Koulakov et al., 2009; Mitterbauer et al., 2011; Dando et al., 2011).

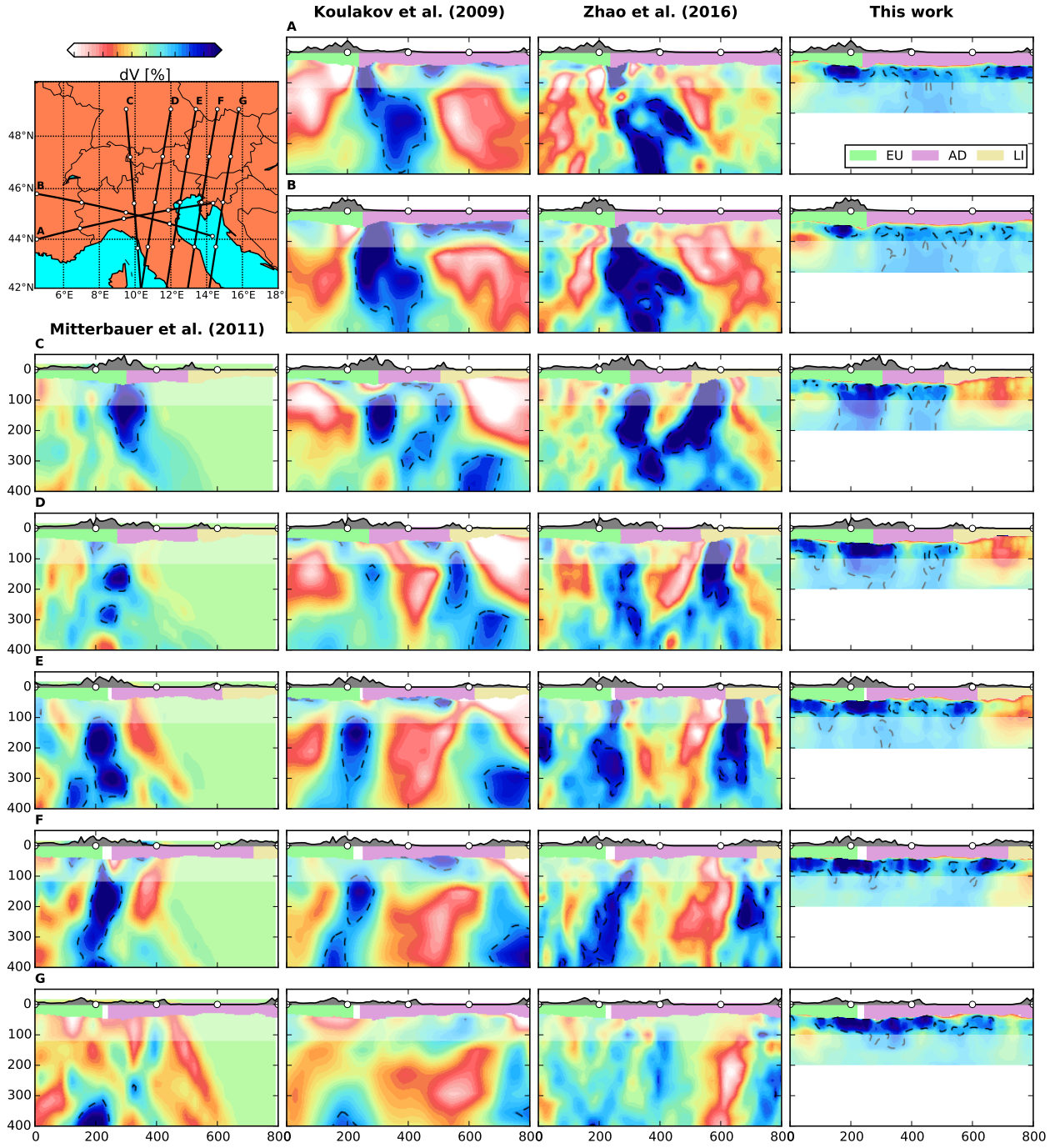

Figure 2: Comparison of teleseismic body-wave tomographic models with this work along seven cross-sections. The body-wave models show deviations of v_P ($\pm 2\%$ for the models of Mitterbauer et al. (2011) and Koulakov et al. (2009) and $\pm 3\%$ for one of Zhao et al. (2016)). The surface-wave model (this work) gives deviations of v_S to a Voigt-averaged (Babuska and Cara, 1991) PREM-model (Dziewonski and Anderson, 1981), with limits of $\pm 4\%$.

2.1 Origin of the deep slab

The possibility of slab stretching (Mitterbauer et al., 2011; Handy et al., 2015) seems unlikely, given a length greater than 350 km from most studies (Mitterbauer et al., 2011; Dando et al., 2011; Zhao et al., 2016; Hua et al., 2017). Another possibility is that subducted Adriatic lithosphere may have been introduced sideways from the NE-directed subduction under the Dinarides (Ustaszewski et al., 2008). It has been proposed that a considerable amount of shortening in the northern Dinarides took place during the Paleogene due to the NE-directed subduction of Adria (Schmid et al., 2008; Ustaszewski et al., 2008; Korbar, 2009; Handy et al., 2015). Quantitative estimates are, however, still a matter of debate (Korbar, 2009). After the proposed slab break-off around 35 Ma and onsetting opening of the Pannonian basin, dynamics in the northern Dinarides have been mostly dominated by roll-back subduction until 20 Ma and later by dextral transform faulting (Handy et al., 2015). Only in the southernmost part of the Dinarides there may have been ongoing NE-directed shortening after 20 Ma of about 235 km due to the rotational movement of Adria (Ustaszewski et al., 2008). Additionally, tomographic images show a slab gap below 150 km depth in the northern Dinarides (Wortel and Spakman, 2000; Piromallo and Morelli, 2003; Spakman and Wortel, 2004; Koulakov et al., 2009), which may be due to the asthenospheric upwelling in the Pannonian basin (e.g., Faccenna et al., 2014). It is therefore not possible to directly link the deep eastern Alpine slab to the Dinaric one. Given (1) the lack of a deep slab in the northern Dinarides, (2) the assumption of mostly strike-slip faulting and (3) the inferred SW-directed pull during slab rollback, we think that the idea of a sideways, northward introduction of a deep, Adriatic slab under the eastern Alps is rather speculative. This leaves a third possibility, which is a European slab at depth.
This is also supported by the anisotropy pattern observed from SKS-splitting, which shows two layers below the eastern Alps (Qorbani et al., 2015). The fast axis orientation in the deeper layer corresponds to the orientation in the central Alps and points therefore to a continuation of the European slab at depth.

2.2 Body-wave models

From tomographic imaging, the main arguments that are discussed in the context of Adriatic subduction under the eastern Alps are (1) the slab dip (2) a potential link with the Adriatic Moho and (3) the discontinuity of the slab from the central Alps.
Slab dip is often ambiguous in the Alps, where the slabs are mostly sub-vertical, with dipping angles between 70 and 90° (Lippitsch et al., 2003; Koulakov et al., 2009; Dando

et al., 2011; Mitterbauer et al., 2011; Zhao et al., 2016; Hua et al., 2017; Kästle et al., 2017). The resolution limit and the geometry of the ray paths may furthermore introduce artifacts that may bias the apparent dipping angle. If we follow the argument above, assuming that the length of the Adriatic slab should not be longer than 50 – 190 km, the slab dip below 250 km depth should not be considered. Northward dip of the slab under the easten Alps can, however, often only be unambiguously inferred when the entire slab in the upper mantle is taken into account (Mitterbauer et al., 2011; Zhao et al., 2016; Hua et al., 2017), thus increasing the uncertainty of dip angle interpretations.
Despite these uncertainties, the slightly northward dipping slab seems to be a robust feature that can be observed in all recent tomographic studies (Lippitsch et al., 2003; Koulakov et al., 2009; Dando et al., 2011; Mitterbauer et al., 2011; Zhao et al., 2016; Hua et al., 2017, Fig. 2). Given that this affects also the deeper part of the slab, possibly remnant of the subduction European plate, we think it is worth taking also other effects into account that may influence the dipping angle. Northward directed asthenospheric flow due to the rollback subduction of Adria (Vignaroli et al., 2008; Faccenna et al., 2014) may exert a push while simultaneous extrusion of the Carpathians towards the east could cause a suction force that overturned the slab.

A link of the fast slab anomaly to either the European or the Adriatic plate is difficult as teleseismic body-wave tomography tends to suffer from smearing along ray paths in the uppermost mantle and to be strongly dependent on crustal corrections. A link to either Moho is therefore only valid if there is a very clear attachment, which is not the case for any tomographic model in the eastern Alps. This ambiguity is also evident in the cross-sections in Figure 2, e.g. for the Adriatic slab under the Apennines (sections C,D,E) which indicate rather an attachment to the Ligurian plate in the models of Zhao et al. (2016). The shallow (50–100 km) slab positions are better resolved with the surface-wave model from this work. Additionally the Moho structure itself suffers from uncertainty in the eastern Alps and gives no clear hint on which plate is on top (e.g., Lüschen et al., 2004; Schmid et al., 2004; Spada et al., 2013).

A discontinuity between central and eastern Alpine slabs is indeed observed in most models (Lippitsch et al., 2003; Koulakov et al., 2009; Mitterbauer et al., 2011; Zhao et al., 2016; Kästle et al., 2017). It is expressed in the absence of a fast velocity anomaly between central and eastern Alps (Lippitsch et al., 2003) or a northward step of the anomaly (Zhao et al., 2016) and points therefore to a different evolution of the two domains. It has been proposed that the discontinuity is linked to the Giudicarie line, which

offsets the Periadriatic fault towards the north (e.g., Zhao et al., 2016). Handy et al. (2015) argue that the Giudicarie fault does not extend below Moho depths, as the Moho structure seems not to be disrupted along the fault. A small offset between central and eastern Alpine Moho is, however, visible in the Moho map of Kästle et al. (2017). The spatial correlation of the limit between central and eastern Alpine mantle anomalies and the Giudicarie fault is nevertheless an intriguing feature.

2.3 Surface-wave model

We contribute to the above discussion by the adding a surface-wave model of the Alpine region down to a depth of 150 km, considering that the latter technique is best suited for this depth range (Fig. 3). We show the model in combination with body-wave tomographic ones of Mitterbauer et al. (2011) and Zhao et al. (2016) to study the structures of the entire upper mantle. A zone between 100 and 140 km depth is defined where we think that the uncertainties of both surface- and teleseismic body-wave methods are high. Surface waves loose resolution at greater depths due to the long wavelengths in addition to the non-uniqueness of the inverse problem when determining the depth structure (e.g., Kästle et al., 2017). In teleseismic body-wave tomography, the number of crossing paths and the crustal corrections are the main limiting factors. The combined cross-sections are not directly comparable in anomaly strength, because of different sensitivities and different measured velocities (v_S and v_P). However, the geometry of the structure gives valuable additional information.

The surface-wave model shows a clear difference in strength and distribution of the fast anomaly between central and eastern Alps. The central Alpine anomaly shows higher shear-velocities compared to the eastern Alps extending eastward to 12–13°E, which coincides approximately with the Giudicarie fault. In the eastern Alps, the strong, fast anomaly disappears below about 80 km. We infer that that the European slab in the eastern Alps is detached. This agrees with body-wave tomographic studies which indicate that the deep slab is not linked to the lithosphere (Tab. 1). The remaining positive 1% anomaly at 100 km depth in the eastern Alps may be caused by smearing from the deep, detached slab. If the European slab did not detach smoothly along a horizontal depth level, but shows a rather rough, undulating detachment contour, this could give, on average, the 1% v_S increase. Also, subduction of the Adriatic plate in the top 150 km could explain the anomaly which is similar to the v_S anomaly of the Apenninic slab that shows an increase in shear velocity of about 1.5%. From the surface-wave model we are not able to uniquely distinguish between these possibilities.

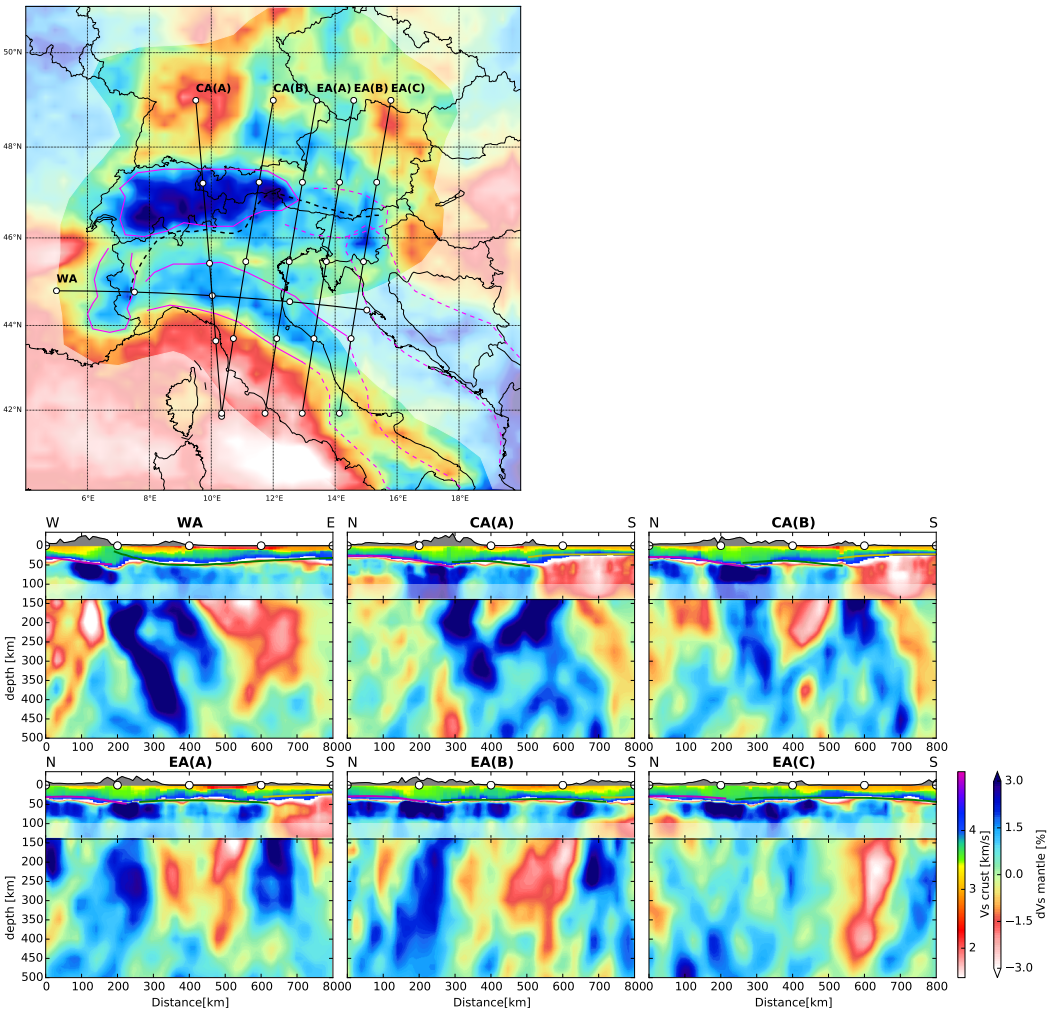

Figure 3: Combined cross-sections through the Alps using the presented surface-wave model (Kästle et al., 2017) between the surface and 140 km depth and the model of Zhao et al. (2016) below. The map view shows the anomalies at 100 km depth from the surface-wave model. Pink lines indicate the size of the different slabs (Apenninic, western Alpine (WA), central Alpine (CA), eastern Alpine (EA) and Dinaric); dashed lines indicate higher uncertainties. The zone between 100 and 140 km is subject to high uncertainties in both models. The lack of a pronounced fast anomaly in the surface-wave model in the western and eastern Alps is interpreted as sign of slab detachments.

We propose that the detached European slab under the eastern Alps lies below 150 km depth at 14°E and increases in depth towards the east (Fig. 3). A similar conclusion can be drawn from the body-wave model of Hua et al. (2017), which sets itself apart from the other mentioned tomographic studies as it uses both local and teleseismic earthquakes. It shows an attached slab in the central Alps and the top of the slab structure increases in depth under the eastern Alps from 150 to 300 km. Such a wedge-like detachment has also been inferred from SKS splitting by Qorbani et al. (2015). The eastern Alpine slab at greater depth seems continuous with a fast anomaly under the Pannonian basin, down to 660 km (Dando et al., 2011).

3 Western Alps

Similar to the eastern Alps, structures in the top 100 km of the mantle are different between tomographic models and therefore difficult to interpret. Lippitsch et al. (2003) propose a slab break-off at lithospheric depth. However, others find a link between the deeper anomaly and the lithosphere and infer that the slab is continuous (Zhao et al., 2016; Hua et al., 2017). At depth greater than 100 km, all models agree on a broad, fast anomaly, which may be an combination of European and Adriatic (from the Apenninic subduction) subduction slabs (Zhao et al., 2016).
Our model suggests a slab detachment in the western Alps below 100 km (Fig. 3). Other than in in the central Alps, there is no clear high-velocity anomaly below this depth (Fig. 2). Instead, a low-velocity anomaly separates the lithospheric anomaly at the junction of European and Adriatic plate from the deeper anomaly. This corresponds to section A for the model of Zhao et al. (2016) (Fig. 2), where shallow and deeper anomaly are separated by a low-velocity patch. Given that further to the north the two anomalies seem linked by a ∼50 km thick fast structure, Zhao et al. (2016) argue nevertheless in favor of a continuous slab. We, however, think that the resolution of teleseismic body-wave tomography is not sufficient to show such a thin link. Our models are limited by the large wavelength of surface waves, but the separation of shallow and deep anomaly, as well as the difference between western and central Alpine anomalies, are robust features that point to a detached European slab.

4 Conclusions

We review the discussion of the European slab detachments under eastern and western Alps by a comparison of regional high-resolution tomography models. The P-wave tomographic models show high agreement in the general slab structures, concerning slab dip and length. However, to understand potential slab detachments at lithospheric level, good resolution in the uppermost 150 km is required. Teleseismic body-wave models are limited in this region due to steep incident angles of teleseismic rays. This "resolution gap" is closed by presenting a shear-velocity model from surface-wave recordings. We are able to show that other than in the central Alps, in both western and eastern Alps the European slab seems detached.

We argue that the deep slab (below 150 km) under the eastern Alps is of European origin. We can, however, not exclude that the Adriatic plate has started subducting towards the north under the eastern Alps (Lippitsch et al., 2003; Ustaszewski et al., 2008; Handy et al., 2015), although our surface-wave model shows no clear slab signature.

To further investigate the question of subduction of the Adriatic plate in the eastern Alps and the geometry and position of the detached European slab in both eastern and western Alps it is necessary to image the entire upper mantle from the bottom of the crust to the mantle discontinuities. This could be done by combination of teleseismic body waves with surface waves or local earthquakes (e.g., Hua et al., 2017). These models can help to give better constraints on the crucial zone between 60 and 150 km depth. It would also be advantageous to have more continuous models between eastern Alps and Dinarides to understand the switch in subduction polarity underneath the two orogens. Up to date, the station distribution in the Dinarides is still a limiting factor.

5 Acknowledgements

We want to thank the different research groups for providing their models (Koulakov et al., 2009; Mitterbauer et al., 2011; Zhao et al., 2016). We are grateful to all the network operators providing data to the EIDA archive (http://www.orfeus-eu.org/eida). Graphics were created with Python Matplotlib and GMT (Wessel and Smith, 2001). This project has received funding from the European Unions Horizon 2020 research and innovation program under the Marie Sklodowska-Curie grant agreement No. 641943.

References

Babuska, V. and Cara, M. (1991). *Seismic anisotropy in the Earth*, volume 10. Springer Science & Business Media.

Blanckenburg, F. and Davies, J. H. (1995). Slab breakoff: a model for syncollisional magmatism and tectonics in the Alps. *Tectonics*, 14(1):120–131.

Brückl, E. (2011). *Lithospheric structure and tectonics of the eastern Alps-evidence from new seismic data*. INTECH Open Access Publisher.

Dando, B., Stuart, G., Houseman, G., Hegedüs, E., Brückl, E., and Radovanović, S. (2011). Teleseismic tomography of the mantle in the Carpathian-Pannonian region of central Europe. *Geophysical Journal International*, 186(1):11–31.

Dziewonski, A. M. and Anderson, D. L. (1981). Preliminary reference earth model. *Physics of the earth and planetary interiors*, 25(4):297–356.

Faccenna, C., Becker, T. W., Auer, L., Billi, A., Boschi, L., Brun, J. P., Capitanio, F. A., Funiciello, F., Horvàth, F., Jolivet, L., et al. (2014). Mantle dynamics in the Mediterranean. *Reviews of Geophysics*, 52(3):283–332.

Handy, M. R., Schmid, S. M., Bousquet, R., Kissling, E., and Bernoulli, D. (2010). Reconciling plate-tectonic reconstructions of Alpine Tethys with the geological–geophysical record of spreading and subduction in the Alps. *Earth-Science Reviews*, 102(3):121–158.

Handy, M. R., Ustaszewski, K., and Kissling, E. (2015). Reconstructing the Alps–Carpathians–Dinarides as a key to understanding switches in subduction polarity, slab gaps and surface motion. *International Journal of Earth Sciences*, 104(1):1–26.

Hua, Y., Zhao, D., and Xu, Y. (2017). P-wave anisotropic tomography of the Alps. *Journal of Geophysical Research: Solid Earth*.

Kästle, E. D., El-Sharkawy, A., Boschi, L., Meier, T., Rosenberg, C., Bellahsen, N., Cristiano, L., and Weidle, C. (2017). Surface-wave tomography of the alps using ambient-noise and earthquake phase-velocity measurements.

Korbar, T. (2009). Orogenic evolution of the External Dinarides in the NE Adriatic region: a model constrained by tectonostratigraphy of Upper Cretaceous to Paleogene carbonates. *Earth-Science Reviews*, 96(4):296–312.

Koulakov, I., Kaban, M., Tesauro, M., and Cloetingh, S. (2009). P-and s-velocity anomalies in the upper mantle beneath europe from tomographic inversion of isc data. *Geophysical Journal International*, 179(1):345–366.

Kummerow, J., Kind, R., Oncken, O., Giese, P., Ryberg, T., Wylegalla, K., Scherbaum, F., Group, T. W., et al. (2004). A natural and controlled source seismic profile through the Eastern Alps: TRANSALP. *Earth and Planetary Science Letters*, 225(1):115–129.

Lippitsch, R., Kissling, E., and Ansorge, J. (2003). Upper mantle structure beneath the alpine orogen from high-resolution teleseismic tomography. *Journal of Geophysical Research: Solid Earth*, 108(B8).

Lüschen, E., Lammerer, B., Gebrande, H., Millahn, K., Nicolich, R., Group, T. W., et al. (2004). Orogenic structure of the Eastern Alps, Europe, from TRANSALP deep seismic reflection profiling. *Tectonophysics*, 388(1):85–102.

Mitterbauer, U., Behm, M., Brückl, E., Lippitsch, R., Guterch, A., Keller, G. R., Koslovskaya, E., Rumpfhuber, E.-M., and Šumanovac, F. (2011). Shape and origin of the east-alpine slab constrained by the alpass teleseismic model. *Tectonophysics*, 510(1):195–206.

Nussbaum, C. (2000). *Neogene tectonics and thermal maturity of sediments of the easternmost southern Alps (Friuli area, Italy)*. PhD thesis.

Piromallo, C. and Morelli, A. (2003). P wave tomography of the mantle under the alpine-mediterranean area. *Journal of Geophysical Research: Solid Earth*, 108(B2).

Qorbani, E., Bianchi, I., and Bokelmann, G. (2015). Slab detachment under the Eastern Alps seen by seismic anisotropy. *Earth and planetary science letters*, 409:96–108.

Schmid, S. M., Bernoulli, D., Fügenschuh, B., Matenco, L., Schefer, S., Schuster, R., Tischler, M., and Ustaszewski, K. (2008). The alpine-carpathian-dinaridic orogenic system: correlation and evolution of tectonic units. *Swiss Journal of Geosciences*, 101(1):139–183.

Schmid, S. M., Fügenschuh, B., Kissling, E., and Schuster, R. (2004). Tectonic map and overall architecture of the Alpine orogen. *Eclogae Geologicae Helvetiae*, 97(1):93–117.

Schmid, S. M., Kissling, E., Diehl, T., van Hinsbergen, D. J., and Molli, G. (2017). Ivrea mantle wedge, arc of the western alps, and kinematic evolution of the alps–apennines orogenic system. *Swiss Journal of Geosciences*, pages 1–32.

Schönborn, G. (1999). Balancing cross sections with kinematic constraints: the Dolomites (northern Italy). *Tectonics*, 18(3):527–545.

Spada, M., Bianchi, I., Kissling, E., Agostinetti, N. P., and Wiemer, S. (2013). Combining controlled-source seismology and receiver function information to derive 3-D Moho topography for Italy. *Geophysical Journal International*, 194(2):1050–1068.

Spakman, W. and Wortel, R. (2004). A tomographic view on western Mediterranean geodynamics. In *The TRANSMED atlas. The Mediterranean region from crust to mantle*, pages 31–52. Springer.

Ustaszewski, K., Schmid, S. M., Fügenschuh, B., Tischler, M., Kissling, E., and Spakman, W. (2008). A map-view restoration of the Alpine-Carpathian-Dinaridic system for the Early Miocene. In *Orogenic Processes in the Alpine Collision Zone*, pages S273–S294. Springer.

Vignaroli, G., Faccenna, C., Jolivet, L., Piromallo, C., and Rossetti, F. (2008). Subduction polarity reversal at the junction between the Western Alps and the Northern Apennines, Italy. *Tectonophysics*, 450(1):34–50.

Wessel, P. and Smith, W. H. (2001). The Generic Mapping Tools.

Wortel, M. and Spakman, W. (2000). Subduction and slab detachment in the mediterranean-carpathian region. *Science*, 290(5498):1910–1917.

Zhao, L., Paul, A., Malusà, M. G., Xu, X., Zheng, T., Solarino, S., Guillot, S., Schwartz, S., Dumont, T., Salimbeni, S., et al. (2016). Continuity of the Alpine slab unraveled by high-resolution P wave tomography. *Journal of Geophysical Research: Solid Earth*.

4.1 Supplementary material

Additionally to Figure 2 in the presented article, another comparison is shown here, which includes the v_S model of Koulakov et al. (2009) (Fig. 4.1). To the knowledge of the author, this is the only published high-resolution body-wave shear-velocity model of the Alpine upper mantle apart from the herein presented surface-wave model. The resolution of the v_S model of Koulakov et al. (2009) is still rather low compared to the v_P model from the same authors. This may explain why individual slabs of Europe and Adria are difficult to distinguish, especially in profile C. It becomes evident that in the v_S model of Koulakov et al. (2009) in the eastern Alps the slab below 100 km is almost absent compared to their v_P model. This is similar to the surface-wave model and may be a feature of the shear-velocity structure of the eastern Alpine subduction zone.

4.2 Concluding remarks

The above discussion shows that there is need for better constraints of the upper mantle structure beneath the Alps between 50 and 150 km. The body-wave tomographic images show clear slabs, but in most areas it is not possible to link these structures to crustal models. Also the discrepancies between different tomographic models leave structural interpretations inconclusive. It is shown that surface waves can provide valuable additional information that illuminate the crust-mantle transition and the top part of the subduction slabs. This gives important hints on the detachment of the European slab in western and eastern Alps. However, some structures remain ambiguous, it is for example not possible to give a unique interpretation of the 1% v_S anomaly in the eastern Alps.

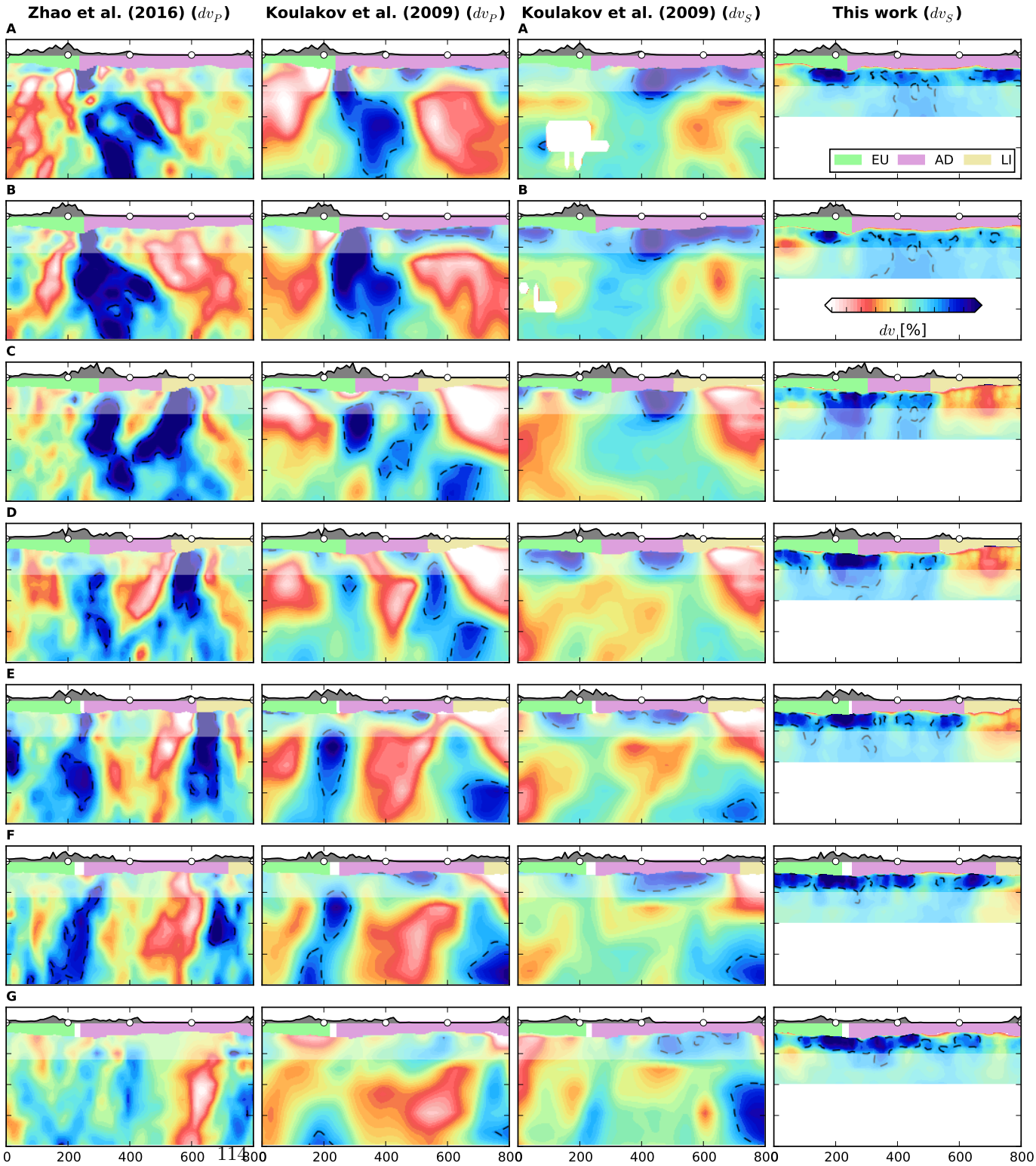
Zhao et al. (2016) (dv_P)
Koulakov et al. (2009) (dv_P)
Koulakov et al. (2009) (dv_S)
This work (dv_S)
A
B
C
D
E
F
G
EU
AD
LI
dv [%]
0
200
400
600
800

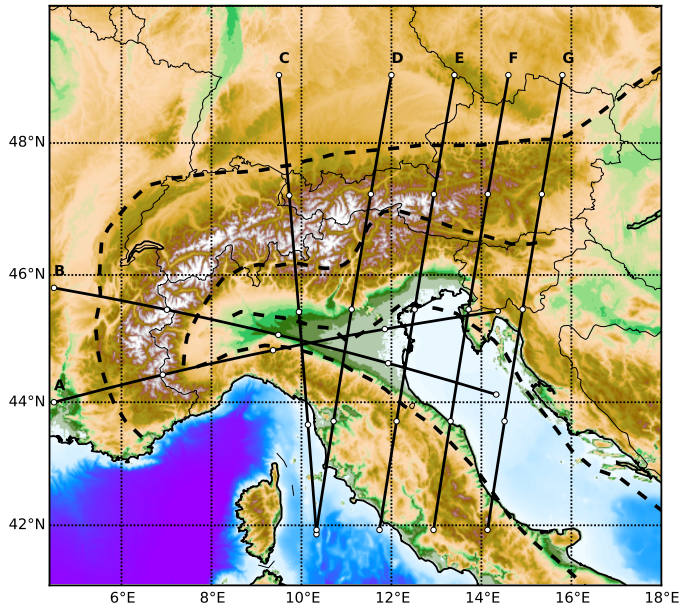

Figure 4.1: Comparison of tomographic models of Zhao et al. (2016), Koulakov et al. (2009) and the model presented in this work. The colorscale is given with respect to PREM (Dziewonski and Anderson, 1981), min/max values are ±3%, ±2% and ±4% for the respective models. White spots in the v_S model of Koulakov et al. (2009) are due to resolution gaps.

5 Conclusions

Central to this work is a new shear-velocity model of the wider Alpine area which images the structures of crust and mantle with higher detail and on a larger scale than previous v_S models. Another unique feature is the coverage of both crust and upper mantle structures for the region. This is achieved by a combination of ambient-noise and earthquake-based records.

The ambient-noise measurements have been obtained by an updated method, based on noise cross-correlations in the frequency domain. A detailed description of the method is given and an automated script to evaluate large data sets is provided online (`http://hestia.lgs.jussieu.fr/~boschil/downloads.html`). This includes also treatment of horizontal component correlations, for which the second order Bessel-function term (J_2) has to be taken into account order not to bias the measurements, as shown in the presented work. The earthquake data is provided through a cooperation with the University of Kiel by T. Meier, R. Soomro and A. El-Sharkawy.
A thorough comparison between two-station phase-velocity measurements is performed to validate this approach. Several thousand Rayleigh- and Love-wave dispersion curves are evaluated to test for differences in the common period range (8–60 s) of the two methods. A small bias with average discrepancy lower than 0.04 km/s for Rayleigh waves and 0.06 km/s for Love waves is observed in the data sets by which the ambient-noise based velocity estimates are lower than those obtained by the earthquake method. This is more than 10 times lower than the peak-to-peak variations in the phase-velocity maps. This bias is also present in earlier works, showing similar or less pronounced differences and is systematically described in this work for the first time.
A suite of synthetic tests is performed to investigate whether this discrepancy can be explained by approximations made in the derivation of the ambient-noise method. It is shown that an azimuthally non-uniform noise source distribution can influence the phase-velocity estimates, however, this effect vanishes when the measurements of station pairs of different azimuths are averaged. The bias in the data persists even after azimuthal averaging and is therefore unlikely to be caused by the noise source

distribution. Also, the effects of near-field sources and azimuthal velocity anisotropy are tested. None of these are found to offer and explanation for the shown bias. It is inferred that a combination of factors is most likely causing the small discrepancy, including laterals velocity variations and differences in the sensitivity of earthquake and ambient-noise based measurements. A small influence from higher modes can also not be excluded for the earthquake measurements.
For imaging purposes this discrepancy is negligible. Comparison of phase velocity maps show that there is good agreement between the structures imaged by both methods. The combination of both data sets can therefore be used to cover a larger period range and thus a broader depth range.

The procedure to obtain the complete 3-D v_S model is presented. This includes data preparation, a linearized inversion to create phase-velocity maps and a stochastic model search to find 1-D depth profiles at each cell of the model space. Checkerboard tests for the phase-velocity map inversion show that especially in the Alps and Apennines structures of 50 km block size can be resolved. By comparison with known geologic features such as sedimentary basins it is inferred that the resolution in the shallow crust reaches 25 km in the well resolved regions, including most parts of Switzerland, Italy, southern Germany and western Austria. An excellent depth resolution in the crust is evidenced from the 1-D resolution tests for the model search. The Moho depth estimation agrees well ($\pm 2 - -5\ km$) with the synthetic input model for simple crustal structures. At greater depth the tests indicate that anomalies are reproduced with lower amplitude and vertical smearing is especially observed for mantle anomalies below 100 km depth.

The crustal model shows known geologic structures such as the Ivrea body anomaly in the western Alps and the depth of sedimentary basins. The imaged Moho depths correspond to earlier results from receiver functions with deviations lower than 5 km in most areas. Given its high degree of detail and the large extend, the presented model has the potential to serve as reference for the v_S structure of the Alpine and Apenninic crust.

The upper mantle structure presented in this work shows fast anomalies under the orogens that are interpreted as subduction slabs. In the central Alps a broad, fast velocity anomaly extends vertically to the bottom of the model at 200 km depth. No slab detachment is visible in this depth range. This is clearly different from the western Alps, where the anomaly can not be traced below 100 km depth. A deeper

anomaly is separated from the western Alpine slab by a low-velocity zone. It is inferred that this is caused by a detachment of the European slab.
The difference in the anomaly strength between eastern and central Alps (1% vs 3%) and the absence of a clear slab structure in the eastern Alps indicates that the European slab is broken off east of 13°E. This coincides spatially approximately with the Giudicarie fault, which offsets the Periadriatic fault towards the north. The remaining 1% fast anomaly in the eastern Alps can be explained by (1) the presence of remnants of the detached European slab, (2) by vertical smearing between the fast lithosphere and the deeper European slab, (3) a subduction of Adria towards the north or (4) a combination of these effects. By comparison with body-wave tomographic models we infer that at depth greater 150–200 km a high-velocity anomaly is present which is most likely caused by the subducted European plate. An Adriatic slab reaching continuously from the lithosphere to 400 km depth as previously proposed is excluded in the presented interpretation.
The presence of a secondary anomaly north of the the eastern Alps in our models is denominated Eastern Alpine Northern Anomaly and is still enigmatic and could be the subject of further studies.
The eastern Alpine anomaly shows an almost continuous transition to the Dinaric subduction, south of the Periadriatic fault. The Dinaric slab is visible down to 150 km depth and the deeper zone is interpreted as slab gap.
The Apenninic slab is most pronounced in the northern Apennines. Its anomaly is weaker compared to the central Alps and the slab appears thinner in the presented model. Nevertheless, it can be followed from the bottom of the Moho to 200 km depth. In the southern Apennines the structures are more complicated. A shallow (50–150 km) slab gap causes the disappearance of the Apenninic anomaly in southern Italy.

A typical limitation of teleseismic body-wave tomographic models is the steep incidence angle of rays in the lithosphere and asthenosphere, limiting the resolution in the upper mantle. The zone between the bottom of the crust and 200 km is, however, crucial for our understanding of shallow slab detachments in the Alps and the potential subduction of Adria in the eastern Alps. This work shows that the combination of ambient-noise and earthquake derived surface-wave measurements is able to provide models that can help to constrain structures in the uppermost mantle.
Further work is required in the eastern Alps and along the transition to the Dinarides to improve our understanding of the present subduction mechanism. Joint inversions of surface and body waves could provide the needed resolution in the upper 200 km to potentially distinguish between detached European and Adriatic slab.

6 Outlook

This chapter points out ideas and challenges for future research work.

- **Extension of the ambient-noise data set.**
  The study has shown that ambient noise is a very valuable data source especially for the crustal structure. The presented data set contains cross correlations of 1 – 3 years and covers periods between 4–75 s. With careful processing and long recording times it would likely be possible to increase the number of measurements at long periods and even extend the period range of the phase-velocity curves. At the short-period end station-station distance can be a limiting factor to extract shorter period signals, but it may be equally be improved by increased recording times. However, higher modes are likely to be a bigger problem at periods below 4 s and will need more attention than in the presented work.
  Cross-correlations between Z and R components can be used to additionally constrain the Rayleigh-wave phase-velocity mesurements (Haney et al., 2012).
  Also it may be worth testing whether body waves can be extracted from ambient-noise data.

- **Correction for noise source distribution.**
  The approximate velocity bias is predictable if the noise source distribution is known as shown in the first article within this thesis (see also Weaver et al., 2009; Sadeghisorkhani et al., 2017). This may be used to improve the recordings and lowering the error of the measurements.

- **Reason for the bias between ambient-noise and earthquake-based measurements.**
  The hypothesis of different structural sensitivities of the two methods which is suggested to be responsible for the evidenced bias could be tested with full-waveform modeling techniques. These may also be used to test how structural heterogeneities influence ambient-noise measurements. Lateral inhomogeneous structures are assumed to have a similar influence on ambient-noise measurements to non-homogeneous source distributions, therefore it would also be possible to iteratively correct for this effect.

- **Uncertainty estimates.**
  With the presented method to obtain 3-D models it is not straightforward to give also 3-D resolution maps and meaningful uncertainty estimates. Measurement uncertainties are estimated by comparing the ambient-noise to the earthquake method (chapter 2) or by comparing station triplets (chapter 3). However, these estimates may be, as shown, due to methodological differences and therefore not representing the measurement error or not completely independent in case of the station triplet method. Tracking uncertainties throughout the model creation would be helpful for the interpretation of the final models.

- **Radial anisotropy.**
  The preliminary tests in the supplementary material section of chapter 3 show that both Love and Rayleigh-waves can constrain independently the general structures. Whether this can also be used to give the radially anisotropic structure needs more thorough testing. Some of the differences between Rayleigh- and Love-wave structures may rather be caused by different sensitivities than anisotropy. The radially anisotropic structure is of interest to study the mantle flow in the asthenosphere under the central Mediterranean area.

- **Eikonal tomography for the phase-velocity maps.**
  The linearized inversion which is used to obtain the 2-D phase-velocity map is based on straight rays, an assumption which is approximately correct and gives only minor structural differences compared to more sophisticated inversion approaches (Boschi and Dziewonski, 1999). However, given that the velocity contrasts in the crust can be quite large, it is worth testing whether approaches that take ray-bending into account, such as Eikonal tomography can improve the 2-D models.

- **Combination with body-wave data.**
  With the herein applied method it is difficult to constrain structures below 100–150 km depth due to the long wavelength of surface waves and the non-uniqueness of the inverse problem. The addition of body-wave data can help to better image deep structures and also extend the imaged area to greater depth, thus showing the continuation of the slabs into greater depths. The models may therefore profit considerably from a joint inversion of surface and S body waves (e.g., Auer et al., 2014).

- **Data coverage in the eastern Alps and Dinarides.**
  To answer the question of Adriatic subduction, the position of the shallow slabs

in the eastern Alps and the slab gap in the Dinarides it is probably necessary to improve the station coverage in these regions. This will partially be the case due to the AlpArray project (`http://www.alparray.ethz.ch`) although the coverage in the Dinarides south of Slovenia will remain sparse.

Bibliography

Aki, K. (1957). Space and time spectra of stationary stochastic waves, with special reference to microtremors. *Bull. Earthq. Res. Inst.*, 35:411–451.

Ardhuin, F., Gualtieri, L., and Stutzmann, E. (2015). How ocean waves rock the Earth: Two mechanisms explain microseisms with periods 3 to 300 s. *Geophysical Research Letters*, 42(3):765–772.

Ardhuin, F. and Herbers, T. H. (2013). Noise generation in the solid Earth, oceans and atmosphere, from nonlinear interacting surface gravity waves in finite depth. *Journal of Fluid Mechanics*, 716:316–348.

Auer, L., Boschi, L., Becker, T., Nissen-Meyer, T., and Giardini, D. (2014). Savani: A variable resolution whole-mantle model of anisotropic shear velocity variations based on multiple data sets. *Journal of Geophysical Research: Solid Earth*, 119(4):3006–3034.

Behm, M., Brückl, E., Chwatal, W., and Thybo, H. (2007). Application of stacking and inversion techniques to three-dimensional wide-angle reflection and refraction seismic data of the Eastern Alps. *Geophysical Journal International*, 170(1):275–298.

Bensen, G., Ritzwoller, M., and Shapiro, N. M. (2008). Broadband ambient noise surface wave tomography across the United States. *Journal of Geophysical Research: Solid Earth*, 113(B5).

Béthoux, N., Sue, C., Paul, A., Virieux, J., Fréchet, J., Thouvenot, F., and Cattaneo, M. (2007). Local tomography and focal mechanisms in the south-western alps: comparison of methods and tectonic implications. *Tectonophysics*, 432(1):1–19.

Beyreuther, M., Barsch, R., Krischer, L., Megies, T., Behr, Y., and Wassermann, J. (2010). ObsPy: A Python toolbox for seismology. *Seismological Research Letters*, 81(3):530–533.

Blanckenburg, F. and Davies, J. H. (1995). Slab breakoff: a model for syncollisional magmatism and tectonics in the Alps. *Tectonics*, 14(1):120–131.

Bleibinhaus, F. and Gebrande, H. (2006). Crustal structure of the Eastern Alps along the TRANSALP profile from wide-angle seismic tomography. *Tectonophysics*, 414(1):51–69.

Bois, C. and Party, E. S. (1990). Major geodynamic processes studied from the ECORS deep seismic profiles in France and adjacent areas. *Tectonophysics*, 173(1-4):397–410.

Boschi, L. and Dziewonski, A. M. (1999). High-and low-resolution images of the Earth's mantle: Implications of different approaches to tomographic modeling. *Journal of Geophysical Research: Solid Earth (1978–2012)*, 104(B11):25567–25594.

Boschi, L. and Weemstra, C. (2015). Stationary-phase integrals in the cross-correlation of ambient noise. *Reviews of Geophysics*, 53(2):411–451.

Brückl, E. (2011). *Lithospheric structure and tectonics of the eastern Alps-evidence from new seismic data*. INTECH Open Access Publisher.

Brückl, E., Bleibinhaus, F., Gosar, A., Grad, M., Guterch, A., Hrubcová, P., Keller, G. R., Majdański, M., Šumanovac, F., Tiira, T., et al. (2007). Crustal structure due to collisional and escape tectonics in the Eastern Alps region based on profiles Alp01 and Alp02 from the ALP 2002 seismic experiment. *J. Geophys. Res.: Solid Earth*, 112(B6).

BRÜCKL, E. and Hammerl, C. (2014). Eduard suess' conception of the Alpine orogeny related to geophysical data and models. *Austrian Journal of Earth Sciences*, 107(1).

Campillo, M. and Paul, A. (2003). Long-range correlations in the diffuse seismic coda. *Science*, 299(5606):547–549.

Campillo, M., Roux, P., Romanowicz, B., and Dziewonski, A. (2014). Seismic imaging and monitoring with ambient noise correlations. *Treatise on Geophysics*, pages 256–271.

Capitanio, F. and Goes, S. (2006). Mesozoic spreading kinematics: consequences for Cenozoic Central and Western Mediterranean subduction. *Geophysical Journal International*, 165(3):804–816.

Carminati, E. and Doglioni, C. (2012). Alps vs. Apennines: the paradigm of a tectonically asymmetric Earth. *Earth-Science Reviews*, 112(1):67–96.

Castellarin, A., Nicolich, R., Fantoni, R., Cantelli, L., Sella, M., and Selli, L. (2006). Structure of the lithosphere beneath the Eastern Alps (southern sector of the TRANSALP transect). *Tectonophysics*, 414(1):259–282.

Channell, J. and Horvath, F. (1976). The African/Adriatic promontory as a palaeogeographical premise for Alpine orogeny and plate movements in the Carpatho-Balkan region. *Tectonophysics*, 35(1-3):71–101.

Dando, B., Stuart, G., Houseman, G., Hegedüs, E., Brückl, E., and Radovanović, S. (2011). Teleseismic tomography of the mantle in the Carpathian-Pannonian region of central Europe. *Geophysical Journal International*, 186(1):11–31.

Diehl, T., Husen, S., Kissling, E., and Deichmann, N. (2009). High-resolution 3-D P-wave model of the Alpine crust. *Geophysical Journal International*, 179(2):1133–1147.

Dziewonski, A. M. and Anderson, D. L. (1981). Preliminary reference earth model. *Physics of the earth and planetary interiors*, 25(4):297–356.

ECORS, T. E.-C. D. S., Hirm, A., Nadir, S., Thouvenot, F., Nicolich, R., Pellis, G., Scarascia, S., Tabacco, I., Castellano, F., Merlanti, F., et al. (1989). Mapping the Moho of the Western Alps by wide-angle reflection seismics. *Tectonophysics*, 162(3-4):193–202.

Ekström, G. (2014). Love and Rayleigh phase-velocity maps, 5–40 s, of the western and central USA from USArray data. *Earth and Planetary Science Letters*, 402:42–49.

Ekström, G., Abers, G. A., and Webb, S. C. (2009). Determination of surface-wave phase velocities across USArray from noise and Aki's spectral formulation. *Geophysical Research Letters*, 36(18).

Faccenna, C., Becker, T. W., Auer, L., Billi, A., Boschi, L., Brun, J. P., Capitanio, F. A., Funiciello, F., Horvàth, F., Jolivet, L., et al. (2014). Mantle dynamics in the Mediterranean. *Reviews of Geophysics*, 52(3):283–332.

Friedrich, A., Krüger, F., and Klinge, K. (1998). Ocean-generated microseismic noise located with the Gräfenberg array. *Journal of Seismology*, 2(1):47–64.

Giacomuzzi, G., Civalleri, M., De Gori, P., and Chiarabba, C. (2012). A 3D Vs model of the upper mantle beneath Italy: Insight on the geodynamics of central Mediterranean. *Earth and Planetary Science Letters*, 335:105–120.

Goes, S., Govers, R., and Vacher, P. (2000). Shallow mantle temperatures under Europe from P and S wave tomography. *Journal of Geophysical Research: Solid Earth*, 105(B5):11153–11169.

Grad, M. and Tiira, T. (2009). The moho depth map of the European Plate. *Geophysical Journal International*, 176(1):279–292.

Handy, M. R., Schmid, S. M., Bousquet, R., Kissling, E., and Bernoulli, D. (2010). Reconciling plate-tectonic reconstructions of Alpine Tethys with the geological–geophysical record of spreading and subduction in the Alps. *Earth-Science Reviews*, 102(3):121–158.

Handy, M. R., Ustaszewski, K., and Kissling, E. (2015). Reconstructing the Alps–Carpathians–Dinarides as a key to understanding switches in subduction polarity, slab gaps and surface motion. *International Journal of Earth Sciences*, 104(1):1–26.

Haney, M. M., Mikesell, T. D., van Wijk, K., and Nakahara, H. (2012). Extension of the spatial autocorrelation (SPAC) method to mixed-component correlations of surface waves. *Geophysical Journal International*, 191(1):189–206.

Hasselmann, K. (1963). A statistical analysis of the generation of microseisms. *Reviews of Geophysics*, 1(2):177–210.

Haubrich, R., Munk, W., and Snodgrass, F. (1963). Comparative spectra of microseisms and swell. *Bulletin of the Seismological Society of America*, 53(1):27–37.

Hillers, G., Graham, N., Campillo, M., Kedar, S., Landès, M., and Shapiro, N. (2012). Global oceanic microseism sources as seen by seismic arrays and predicted by wave action models. *Geochemistry, Geophysics, Geosystems*, 13(1).

Hirn, A., Damotte, B., Torreilles, G., and Party, E. S. (1987). Crustal reflection seismics: the contributions of oblique, low frequency and shear wave illuminations. *Geophysical Journal International*, 89(1):287–296.

Hua, Y., Zhao, D., and Xu, Y. (2017). P-wave anisotropic tomography of the Alps. *Journal of Geophysical Research: Solid Earth*.

Koulakov, I., Kaban, M., Tesauro, M., and Cloetingh, S. (2009). P-and s-velocity anomalies in the upper mantle beneath europe from tomographic inversion of isc data. *Geophysical Journal International*, 179(1):345–366.

Kufner, S.-K., Schurr, B., Sippl, C., Yuan, X., Ratschbacher, L., Ischuk, A., Murodkulov, S., Schneider, F., Mechie, J., Tilmann, F., et al. (2016). Deep India meets deep Asia: Lithospheric indentation, delamination and break-off under Pamir and Hindu Kush (Central Asia). *Earth and Planetary Science Letters*, 435:171–184.

Kummerow, J., Kind, R., Oncken, O., Giese, P., Ryberg, T., Wylegalla, K., Scherbaum, F., Group, T. W., et al. (2004). A natural and controlled source seismic profile through the Eastern Alps: TRANSALP. *Earth and Planetary Science Letters*, 225(1):115–129.

Legendre, C., Meier, T., Lebedev, S., Friederich, W., and Viereck-Götte, L. (2012). A shear wave velocity model of the European upper mantle from automated inversion of seismic shear and surface waveforms. *Geophysical Journal International*, 191(1):282–304.

Li, H., Bernardi, F., and Michelini, A. (2010). Surface wave dispersion measurements from ambient seismic noise analysis in Italy. *Geophysical Journal International*, 180(3):1242–1252.

Lin, F.-C., Moschetti, M. P., and Ritzwoller, M. H. (2008). Surface wave tomography of the western United States from ambient seismic noise: Rayleigh and Love wave phase velocity maps. *Geophysical Journal International*, 173(1):281–298.

Lippitsch, R., Kissling, E., and Ansorge, J. (2003). Upper mantle structure beneath the alpine orogen from high-resolution teleseismic tomography. *Journal of Geophysical Research: Solid Earth*, 108(B8).

Lombardi, D., Braunmiller, J., Kissling, E., and Giardini, D. (2008). Moho depth and Poisson's ratio in the Western-Central Alps from receiver functions. *Geophysical Journal International*, 173(1):249–264.

Longuet-Higgins, M. S. (1950). A theory of the origin of microseisms. *Philosophical Transactions of the Royal Society of London A: Mathematical, Physical and Engineering Sciences*, 243(857):1–35.

Lüschen, E., Lammerer, B., Gebrande, H., Millahn, K., Nicolich, R., Group, T. W., et al. (2004). Orogenic structure of the Eastern Alps, Europe, from TRANSALP deep seismic reflection profiling. *Tectonophysics*, 388(1):85–102.

Mandl, G. and Ondrejicková, A. (1991). Über eine triadische Tiefwasserfazies (Radiolarite, Tonschiefer) in den Nördlichen Kalkalpen – ein Vorbericht. *Jahrbuch der Geologischen Bundesanstalt*, 134(2):309–318.

Meier, T., Soomro, R., Viereck, L., Lebedev, S., Behrmann, J. H., Weidle, C., Cristiano, L., and Hanemann, R. (2016). Mesozoic and Cenozoic evolution of the Central European lithosphere. *Tectonophysics*, 692:58–73.

Miche, A. (1944). Mouvements ondulatoires de la mer en profondeur croissante ou décroissante. forme limite de la houle lors de son déferlement. application aux digues maritimes. deuxième partie. mouvements ondulatoires périodiques en profondeur régulièrement décroissante. *Annales des Ponts et Chaussées*, 114.

Mitterbauer, U., Behm, M., Brückl, E., Lippitsch, R., Guterch, A., Keller, G. R., Koslovskaya, E., Rumpfhuber, E.-M., and Šumanovac, F. (2011). Shape and origin of the east-alpine slab constrained by the alpass teleseismic model. *Tectonophysics*, 510(1):195–206.

Molinari, I., Argnani, A., Morelli, A., and Basini, P. (2015). Development and testing of a 3D seismic velocity model of the Po Plain sedimentary basin, Italy. *Bulletin of the Seismological Society of America*, 105(2A):753–764.

Molinari, I. and Morelli, A. (2011). EPcrust: a reference crustal model for the European Plate. *Geophysical Journal International*, 185(1):352–364.

Muyzert, E. and Snieder, R. (2000). An alternative parameterisation for surface waves in a transverse isotropic medium. *Physics of the Earth and Planetary Interiors*, 118(1):125–133.

Nocquet, J.-M. and Calais, E. (2004). Geodetic measurements of crustal deformation in the Western Mediterranean and Europe. In *Geodynamics of Azores-Tunisia*, pages 661–681. Springer.

Nussbaum, C. (2000). *Neogene tectonics and thermal maturity of sediments of the easternmost southern Alps (Friuli area, Italy)*. PhD thesis.

Pfiffner, O.-A., Lehner, P., Heitzmann, P., Mueller, S., and Steck, A. (1997). *Deep structure of the Swiss Alps*. Springer.

Piromallo, C. and Morelli, A. (2003). P wave tomography of the mantle under the alpine-mediterranean area. *Journal of Geophysical Research: Solid Earth*, 108(B2).

Poli, P., Campillo, M., Pedersen, H., Group, L. W., et al. (2012). Body-wave imaging of Earth's mantle discontinuities from ambient seismic noise. *Science*, 338(6110):1063–1065.

Qorbani, E., Bianchi, I., and Bokelmann, G. (2015). Slab detachment under the Eastern Alps seen by seismic anisotropy. *Earth and planetary science letters*, 409:96–108.

Ren, Y., Stuart, G., Houseman, G., Dando, B., Ionescu, C., Hegedüs, E., Radovanović, S., Shen, Y., Group, S. C. P. W., et al. (2012). Upper mantle structures beneath the Carpathian–Pannonian region: implications for the geodynamics of continental collision. *Earth and Planetary Science Letters*, 349:139–152.

Roure, F., Choukroune, P., and Polino, R. (1996). Deep seismic reflection data and new insights on the bulk geometry of mountain ranges. *Comptes rendus de l'Académie des sciences. Série 2. Sciences de la terre et des planètes*, 322(5):345–359.

Sadeghisorkhani, H., Gudmundsson, Ó., Roberts, R., and Tryggvason, A. (2017). Velocity-measurement bias of the ambient noise method due to source directivity: a case study for the Swedish National Seismic Network. *Geophysical Journal International*, 209(3):1648–1659.

Savostin, L. A., Sibuet, J.-C., Zonenshain, L. P., Le Pichon, X., and Roulet, M.-J. (1986). Kinematic evolution of the Tethys belt from the Atlantic Ocean to the Pamirs since the Triassic. *Tectonophysics*, 123(1-4):1–35.

Schaefer, J., Boschi, L., Becker, T., and Kissling, E. (2011). Radial anisotropy in the European mantle: Tomographic studies explored in terms of mantle flow. *Geophysical Research Letters*, 38(23).

Schmid, S. M., Bernoulli, D., Fügenschuh, B., Matenco, L., Schefer, S., Schuster, R., Tischler, M., and Ustaszewski, K. (2008). The alpine-carpathian-dinaridic orogenic system: correlation and evolution of tectonic units. *Swiss Journal of Geosciences*, 101(1):139–183.

Schmid, S. M., Fügenschuh, B., Kissling, E., and Schuster, R. (2004). Tectonic map and overall architecture of the Alpine orogen. *Eclogae Geologicae Helvetiae*, 97(1):93–117.

Schmid, S. M., Kissling, E., Diehl, T., van Hinsbergen, D. J., and Molli, G. (2017). Ivrea mantle wedge, arc of the western alps, and kinematic evolution of the alps–apennines orogenic system. *Swiss Journal of Geosciences*, pages 1–32.

Schönborn, G. (1999). Balancing cross sections with kinematic constraints: the Dolomites (northern Italy). *Tectonics*, 18(3):527–545.

Shen, W., Ritzwoller, M. H., and Schulte-Pelkum, V. (2013). A 3-D model of the crust and uppermost mantle beneath the Central and Western US by joint inversion of receiver functions and surface wave dispersion. *Journal of Geophysical Research: Solid Earth*, 118(1):262–276.

Singer, J., Diehl, T., Husen, S., Kissling, E., and Duretz, T. (2014). Alpine lithosphere slab rollback causing lower crustal seismicity in northern foreland. *Earth and Planetary Science Letters*, 397:42–56.

Spada, M., Bianchi, I., Kissling, E., Agostinetti, N. P., and Wiemer, S. (2013). Combining controlled-source seismology and receiver function information to derive 3-D Moho topography for Italy. *Geophysical Journal International*, 194(2):1050–1068.

Spakman, W. and Wortel, R. (2004). A tomographic view on western Mediterranean geodynamics. In *The TRANSMED atlas. The Mediterranean region from crust to mantle*, pages 31–52. Springer.

Stampfli, G. M. and Borel, G. (2002). A plate tectonic model for the Paleozoic and Mesozoic constrained by dynamic plate boundaries and restored synthetic oceanic isochrons. *Earth and Planetary Science Letters*, 196(1):17–33.

Thöni, M., Miller, C., BLICHERT-TOFT, J., Whitehouse, M., Konzett, J., and Zanetti, A. (2008). Timing of high-pressure metamorphism and exhumation of the eclogite type-locality (Kupplerbrunn–Prickler Halt, Saualpe, south-eastern Austria): constraints from correlations of the Sm–Nd, Lu–Hf, U–Pb and Rb–Sr isotopic systems. *Journal of Metamorphic Geology*, 26(5):561–581.

Traer, J. and Gerstoft, P. (2014). A unified theory of microseisms and hum. *Journal of Geophysical Research: Solid Earth*, 119(4):3317–3339.

TRANSALP Working Group, Gebrande, H., Lüschen, E., Bopp, M., Bleibinhaus, F., Lammerer, B., Oncken, O., Stiller, M., Kummerow, J., Kind, R., Millahn, K., et al. (2002). First deep seismic reflection images of the Eastern Alps reveal giant crustal wedges and transcrustal ramps. *Geophysical Research Letters*, 29(10).

Tsai, V. C. (2009). On establishing the accuracy of noise tomography travel-time measurements in a realistic medium. *Geophysical Journal International*, 178(3):1555–1564.

Ustaszewski, K., Schmid, S. M., Fügenschuh, B., Tischler, M., Kissling, E., and Spakman, W. (2008). A map-view restoration of the Alpine-Carpathian-Dinaridic system

for the Early Miocene. In *Orogenic Processes in the Alpine Collision Zone*, pages S273–S294. Springer.

Ustaszewski, K., Wu, Y.-M., Suppe, J., Huang, H.-H., Chang, C.-H., and Carena, S. (2012). Crust–mantle boundaries in the Taiwan–Luzon arc-continent collision system determined from local earthquake tomography and 1D models: Implications for the mode of subduction polarity reversal. *Tectonophysics*, 578:31–49.

Verbeke, J., Boschi, L., Stehly, L., Kissling, E., and Michelini, A. (2012). High-resolution Rayleigh-wave velocity maps of central Europe from a dense ambient-noise data set. *Geophysical Journal International*, 188(3):1173–1187.

Vignaroli, G., Faccenna, C., Jolivet, L., Piromallo, C., and Rossetti, F. (2008). Subduction polarity reversal at the junction between the Western Alps and the Northern Apennines, Italy. *Tectonophysics*, 450(1):34–50.

Waldhauser, F., Kissling, E., Ansorge, J., and Mueller, S. (1998). Three dimensional interface modelling with two-dimensional seismic data: the Alpine crust-mantle boundary. *Geophysical Journal International*, 135(1):264–278.

Wapenaar, K., Draganov, D., Snieder, R., Campman, X., and Verdel, A. (2010a). Tutorial on seismic interferometry: Part 1—Basic principles and applications. *Geophysics*, 75(5):75A195–75A209.

Wapenaar, K., Slob, E., Snieder, R., and Curtis, A. (2010b). Tutorial on seismic interferometry: Part 2—Underlying theory and new advances. *Geophysics*, 75(5):75A211–75A227.

Weaver, R., Froment, B., and Campillo, M. (2009). On the correlation of non-isotropically distributed ballistic scalar diffuse waves. *The Journal of the Acoustical Society of America*, 126(4):1817–1826.

Wortel, M. and Spakman, W. (2000). Subduction and slab detachment in the mediterranean-carpathian region. *Science*, 290(5498):1910–1917.

Xie, J., Yang, Y., and Ni, S. (2016). On the accuracy of long-period Rayleigh waves extracted from ambient noise. *Geophysical Journal International*, 206(1):48–55.

Yang, Y. and Ritzwoller, M. H. (2008). Characteristics of ambient seismic noise as a source for surface wave tomography. *Geochemistry, Geophysics, Geosystems*, 9(2).

Yao, H. and Van Der Hilst, R. D. (2009). Analysis of ambient noise energy distribution and phase velocity bias in ambient noise tomography, with application to SE Tibet. *Geophysical Journal International*, 179(2):1113–1132.

Yao, H., van Der Hilst, R. D., and Maarten, V. (2006). Surface-wave array tomography in SE Tibet from ambient seismic noise and two-station analysis—I. Phase velocity maps. *Geophysical Journal International*, 166(2):732–744.

Zhao, L., Paul, A., Guillot, S., Solarino, S., Malusà, M. G., Zheng, T., Aubert, C., Salimbeni, S., Dumont, T., Schwartz, S., et al. (2015). First seismic evidence for continental subduction beneath the Western Alps. *Geology*, 43(9):815–818.

Zhao, L., Paul, A., Malusà, M. G., Xu, X., Zheng, T., Solarino, S., Guillot, S., Schwartz, S., Dumont, T., Salimbeni, S., et al. (2016). Continuity of the Alpine slab unraveled by high-resolution P wave tomography. *Journal of Geophysical Research: Solid Earth*.

Zhou, L., Xie, J., Shen, W., Zheng, Y., Yang, Y., Shi, H., and Ritzwoller, M. H. (2012). The structure of the crust and uppermost mantle beneath South China from ambient noise and earthquake tomography. *Geophysical Journal International*, 189(3):1565–1583.

Zhu, H., Bozdağ, E., Peter, D., and Tromp, J. (2012). Structure of the European upper mantle revealed by adjoint tomography. *Nature Geoscience*, 5(7):493–498.